A biodegradable optical filter and photodetector for monitoring oxygen in living tissues

Ceren Kutucu

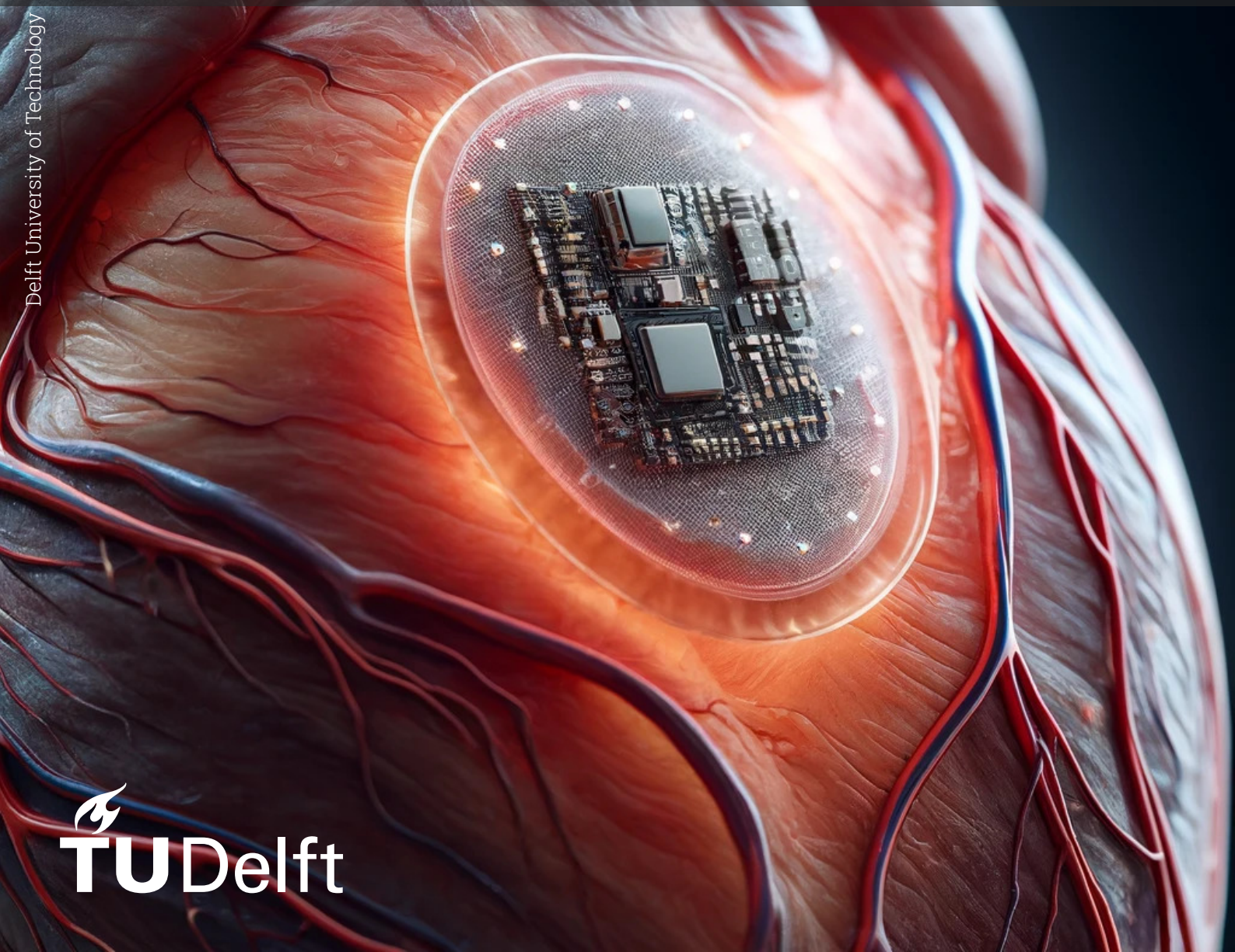

Delft University of Technology

TU Delft

A biodegradable optical filter and photodetector for monitoring oxygen in living tissues

by

Ceren Kutucu

to obtain the degree of Master of Engineering

at the Delft University of Technology,

to be defended publicly on Wednesday July, 3 at 13:00.

Student number:	5777674	
Project duration:	December 4, 2023 – July 3, 2024	
Thesis committee:	Prof. Dr. P. J. French,	TU Delft, Thesis advisor
	Dr. F. Arroyo Cardoso,	TU Delft, Daily supervisor
	Dr. C. Boutry,	TU Delft, Daily supervisor
	Dr. P. R. Rao,	TU Delft, External member
	Msc. Z. Liao	TU Delft, External member

Cover:	Generated by DALL·E using ChatGPT 4.0
Style:	TU Delft Report Style, with modifications by Daan Zwaneveld

An electronic version of this thesis is available at `http://repository.tudelft.nl/`.

TU Delft

Preface

Dear reader,

Here, I present you my master's thesis on the design of a biodegradable optical filter and photodetector for monitoring oxygen in living tissues. I started this project at the beginning of December 2023; where I had almost zero clue on how this project would proceed. It began with an extensive literature review that was interesting and fun to work on, but sometimes a bit tiring. Once I was able to know which way to proceed with design (thankfully!), things started to become clearer, and I am now able to share my research and results with you. My research journey consisted of many ups and downs where some days I was excited about an improvement or a result, whereas some days were not as good as others. At the end of the project, I can say that I learned a lot about the design of an optical filter and optical characterization, which I was able to combine with my knowledge of electrical engineering and biology. Overall, this project helped me learn a lot about research and I had a lot of fun.

There are many people I would like to thank for their help and guidance throughout this project.

First, I would like to thank my thesis advisor, Prof. Paddy J. French, for introducing me to this project and for his guidance, help, and support. Then, I am extremely grateful to my thesis supervisors Dr. Filipe Arroyo Cardoso and Dr. Clementine Boutry for their guidance, help, and support throughout the project. Additionally, many thanks to Dr. Padmakumar R. Rao for his guidance on the Spectra and for being a part of my thesis committee. I would also like to thank Msc. Zhengwei Liao for the many discussions about the project and his help and support. I am also grateful for the support of my colleagues in Bioelectronics, Electronic Instrumentation, and Electronic Components, Technology and Materials research groups, for the discussions in the group meetings and their valuable feedback.

Last but not least, I would like to thank my family and friends for their continuous support. They were always by my side throughout many ups and downs and I would not be able to finish this thesis without their presence and never-ending encouragement.

Ceren Kutucu
Delft, July 2024

Abstract

Tissue vitality monitoring is a crucial process to preserve patients' health during post-surgical recovery or to ensure full adaptation and healing of transplanted organs. Among the many local factors for vitality assessment, tissue oxygenation gives an insight into entire tissue recovery and is directly linked to cell metabolism. To be able to assess oxygenation at the cellular level, NADH fluorescence sensing is used due to its contribution to the cellular respiratory cycle and high sensitivity to oxygen concentration. The current devices for NADH fluorescence sensing are limited to external measurements, where they are suitable for hospital use. This raises the need for a device that is implantable and bioresorbable so that it can stay in the body after the surgery and does not require secondary surgery for removal that puts the patient at risk. The goal of this master's thesis is to introduce the design of a bioresorbable optical filter and photodetector for the measurements of oxygen through the detection of NADH fluorescence. The design consists of an absorption layer, a Fabry-Perot filter, and a wavelength-specific photodetector; where the overall response is designed to have high sensitivity to the emission wavelength of NADH (470nm) and low sensitivity to the excitation of NADH (350nm). ZnO nanoparticles are chosen to be the absorption layer due to their high absorption properties to 350nm and biodegradability, where the optical response is then tested through spectroscopy measurements. For the Fabry-Perot filter, a design with SiO_2 and SiN_x layers has been created with simulation and tested with optical measurements. The complete design consists of 15 layers and has a total thickness of approximately $1\mu m$. Lastly; for the photodetector, Spectra simulations have been conducted for the determination of the optimal design properties. The choices are then adapted to a mask design for the fabrication, in which the back side etching of the silicon wafer is required for biodegradability and optical performance. The fabrication of the photodetector has not been completed due to the time frame of the project. The measurements on the combination of ZnO and Fabry-Perot filter show that the transmission of 470nm is 2.5-4 times larger than the transmission of 350nm, which is expected to increase to at least an order of magnitude when combined with the photodetector. For future experiments, it is recommended to conduct more tests on the filters and ZnO to ensure repeatability and consistency.

Contents

Preface i

Abstract ii

Nomenclature viii

1 Introduction 1

2 State of the art 3
2.1 Oxygen sensing methods . . . 3
2.1.1 Photoplethysmography (PPG) . . . 3
2.1.2 Electrochemical Sensing . . . 5
2.1.3 Photoluminescence . . . 6
2.1.4 NADH . . . 7
2.1.5 Selected oxygen sensing method in this project . . . 7
2.2 NADH Fluorescence Sensing . . . 7
2.2.1 Filter design . . . 8
2.2.2 Detection principle . . . 10
2.3 Material selection . . . 11
2.4 Objective of the research . . . 11

3 Methods 13
3.1 Absorption Layer . . . 13
3.1.1 Choice of Material . . . 13
3.1.2 Process steps . . . 13
3.2 Fabry-Perot Filter . . . 14
3.2.1 Choice of Material . . . 14
3.2.2 Modelling . . . 14
3.2.3 Simulations . . . 15
3.2.4 Process steps . . . 16
3.3 Photodetector . . . 16
3.3.1 Modelling . . . 17
3.3.2 Simulation . . . 19
3.3.3 Choice of material . . . 22
3.3.4 Mask Design . . . 22
3.3.5 Process steps . . . 26
3.4 Test setup . . . 29
3.4.1 Optical Test Setup . . . 29
3.4.2 Photodetector Current Measurement Setup Concept . . . 29

4 Experiments and results 31
4.1 Absorption Layer . . . 31
4.2 Fabry-Perot Filter . . . 33
4.3 Photodetector . . . 35
4.4 Combination of the different parts of the system . . . 37
4.5 Biodegradation time . . . 38

5 Discussion 40
5.1 Test setup . . . 40
5.1.1 Future Outlook . . . 40
5.2 Absorption Layer . . . 41
5.2.1 Future Outlook . . . 41

5.3 Fabry-Perot Filter . . . 41
5.3.1 Design considerations . . . 42
5.3.2 Future Outlook . . . 42
5.4 Photodetector . . . 42
5.4.1 Future Outlook . . . 43
5.5 Combination of the different parts of the system . . . 43
5.5.1 Fabry Perot filter and ZnO absorption layer . . . 43
5.5.2 All . . . 44
5.5.3 Future Outlook . . . 44
5.6 Biodegradation time . . . 44
5.6.1 Future Outlook . . . 44

6 Conclusions **46**

References **47**

A Matlab Code for Detector Characterization **51**

B Minimum light intensity determination **53**

C Mask Design **55**

D Transmission spectrum of filters at different angles of incidence **61**

E Transmission spectrum of ZnO absorption layers at different angles of incidence **62**

F Transmission spectrum of filters with ZnO absorption layers at different angles of incidence **64**

List of Figures

2.1 Examples of the four main oxygen sensing methods . . . 3
2.2 Cellular autofluorescence spectra [25] . . . 8
2.3 Example for transmission spectrum of filters [27] . . . 9
2.4 Fabry-Perot interference filter example from Pimenta et. al. [28] . . . 10
2.5 Gated photodiode structure by Choi et.al. [31] . . . 11

3.1 ZnO spectral response . . . 14
3.2 Transmittance of the simulated filters . . . 16
3.3 Adapted design of the photodetector . . . 17
3.4 One-well models with arrows indicating the incoming light . . . 18
3.5 Current response at different depths within the substrate over the spectrum . . . 19
3.6 Structures in the mask design . . . 23
3.7 Images of the mask . . . 24
3.8 Vernier scales . . . 24
3.9 Test structure . . . 25
3.10 STI etching and thermal oxidation . . . 26
3.11 P-type doping . . . 26
3.12 N-type doping . . . 27
3.13 Gate opening and oxidation . . . 27
3.14 Contact opening . . . 27
3.15 Metal deposition and interconnect . . . 28
3.16 TMAH etching profile . . . 28
3.17 Back side etching . . . 29
3.18 Optical test setup . . . 30

4.1 Transmission of 470nm over 350nm at different angles of incidence for samples with 10-minute anneal . . . 32
4.2 Transmission of 470nm over 350nm at different angles of incidence for samples spun at 1500rpm with different annealing times . . . 32
4.3 Transmission of 470nm over 350nm at different angles of incidence for samples spun at 2000rpm with different annealing times . . . 33
4.4 Transmission spectra of the Fabry-Perot filters . . . 34
4.5 Transmission ratio of 350nm and 470nm at different angles of incidence . . . 34
4.6 Factor of 470nm with respect to 350nm at different angles of incidence . . . 35
4.7 Pre-fabrication tests for photodetector . . . 36
4.8 Delamination of filter 1 after annealing . . . 37
4.9 Transmission of 470nm over 350nm at different angles of incidence for the combination of the filters with the ZnO absorption layer . . . 37
4.10 Transmission of 470nm over 350nm at different angles of incidence for the Fabry-Perot filters and the combination of the filters with the ZnO absorption layer . . . 38

5.1 Spectrum of DH2000 Deuterium Tungsten Halogen Lamp . . . 40

B.1 Current response of the device configurations at different light intensities . . . 53

C.1 Image 1: P-type doping . . . 55
C.2 Image 2: N-type doping . . . 56
C.3 Image 3: Gate opening . . . 56
C.4 Image 4: Contact opening . . . 57
C.5 Image 5: Metal interconnect . . . 57

C.6 Image 6: Back-side opening 58
C.7 Image 7: Pad opening (Positive photoresist) 58
C.8 Image 8: Pad opening (Negative photoresist) 59
C.9 Image 9: Shallow Trench Isolation 59
C.10 Complete mask design with labeling of the specific regions of the mask 60

D.1 Transmission spectra of the Fabry-Perot filters at different angles of incidence 61

E.1 Transmission spectrum of ZnO sample with 1000rpm/80s spin coating and 10-minute annealing 62
E.2 Transmission spectrum of ZnO samples with 1500rpm/65s spin coating 63
E.3 Transmission spectrum of ZnO samples with 2000rpm/40s spin coating 63

F.1 Transmission spectra of the Fabry-Perot filters with ZnO absorption layers at different angles of incidence 64

List of Tables

3.1 Filter configurations from simulations 15
3.2 Transmission of filters at 350nm and 470nm 16
3.3 Percentage of currents of test wavelengths w.r.t 470nm at different gate voltages 20
3.4 Percentage of currents of test wavelengths w.r.t total current at different gate voltages . 20
3.5 Percentage of currents of test wavelengths with different channel widths for $5\mu m$ 21
3.6 Percentage of currents of test wavelengths with different channel widths for $15\mu m$ . . . 21
3.7 Percentage of currents of test wavelengths with different channel widths for $25\mu m$ . . . 21
3.8 Ratio of 400nm and 470nm with different substrate thicknesses 22
3.9 Devices in the mask 23

4.1 Thicknesses of ZnO absorption layers 33
4.2 STI etching results 36
4.3 Percent change of the combination of ZnO absorption layer and Fabry-Perot filter compared to Fabry-Perot filters 38
4.4 Total expected biodegradation times of each component 39

Nomenclature

Abbreviations

Abbreviation	Definition
Ag/AgCl	Sodium/Sodium chloride
AFM	Atomic force microscope
ATP	Adenosine triphosphate
B	Boron element
BHF	Buffered hydrofluoric acid
CE	Counter electrode
Cl^-	Chlorine ion
CO_2	Carbon dioxide
DSP	Double side polished
e^-	Electron
H	High refractive index material in Fabry-Perot filter
H^+	Hydrogen ion
H_2O	Water
H_2O_2	Hydrogen peroxide
Hb	Deoxyhemoglobin
HbO_2	Oxyhemoglobin
HF	Hydrofluoric acid
ICPECVD	Inductively coupled plasma enhanced chemical vapor deposition
ICU	Intensive care unit
IPA	Isopropyl alcohol
ISO	International Organization for Standardization
KOH	Potassium hydroxide
L	Low refractive index material in Fabry-Perot filter
LED	Light emitting diode
Mg	Magnesium element
Mo	Molybdenum element
Mo-W	Molybdenum - Tungsten
NAD^+	Nicotinamide adenine dinucleotide (oxidized form)
$NADH$	Nicotinamide adenine dinucleotide (reduced form)
NIR	Near-infrared
NIRS	Near-infrared spectroscopy
O_2	Oxygen gas
OH^-	Hydroxyl ion
P	Phosphorus element
PBS	Phosphate-buffered saline
PCB	Printed circuit board
Pd-MABP	Palladium-benzoporphyrin
PECVD	Plasma enhanced chemical vapor deposition
PLA	Polylactic acid
PLGA	Poly(lactic-co-glycolic acid)
PPG	Photoplethysmography
Pt	Platinum element
PtOEP	Platinum octaethylporphyrin
RE	Reference electrode

Abbreviation	Definition
SEM	Scanning electron microscope
SiN_x	Silicon nitride
SiO_2	Silicon oxide
SNR	Signal-to-noise ratio
STI	Shallow trench isolation
TLM	Transfer length method
TMAH	Tetramethylammonium hydroxide
UV	Ultraviolet light
WE	Working electrode
Zn	Zinc element
ZnO	Zinc oxide

Symbols

Symbol	Definition	Unit
c	Speed of light in free space	[m/s]
C_{Hb}	Concentration of deoxyhemoglobin	[mol/L]
C_{HbO_2}	Concentration of oxyhemoglobin	[mol/L]
E°	Chemical potential	[V]
f_{op}	Operation frequency of the light source	Hz
G	Carrier generation rate	[$carrier/cm^3s$]
h	Planck's constant	
I	Intensity of light	[W/m^2]
I_0, i_{v0}	Initial intensity of light	[W/m^2]
I_{PC}, I_{lum}	Photocurrent	A
$i_v(x)$	Intensity of light with respect to distance	[W/m^2]
k	Boltzmann constant	
L, x	Distance	[m]
L_T	Transfer length	[m]
n	Refractive index	
N_A	Acceptor concentration	[$atoms/cm^3$]
N_D	Donor concentration	[$atoms/cm^3$]
n_i	intrinsic carrier concentration	[$atoms/cm^3$]
$P_{T_{O_2}}$	Oxygen tension of the visceral surface tissue	[%atm]
q	Elementary charge	[C]
R_c	Contact resistance	[Ω]
R_s	Sheet resistance	[Ω]
S	Surface area	[m^2]
SO_2	Oxygen saturation	[%]
t	Thickness	[m]
T	Temperature	[K]
T_{350nm}	Transmission of 350nm	[%]
T_{470nm}	Transmission of 470nm	[%]
V_{bi}	Intrinsic bias voltage	[V]
V_G, V_{PG}	Gate voltage	[V]
V_{GS}	Gate-source voltage	[V]
V_r	Reverse bias voltage	[V]
w	Width	[m]
W	Depletion depth	[m]
W_{pn}	Intrinsic depletion width	[m]
$W_{pn,new}$	Biased depletion width	[m]
α	Absorption coefficient	[m^{-1}]

Symbol	Definition	Unit
$\Delta\Phi$	Phase difference	
ϵ_r	Relative permittivity	
ϵ_0	Vacuum permittivity	[F/m]
θ	Angle of incidence	Degrees
κ_{SV}	Stern-Volmer constant	
λ	Wavelength	[m]
ρ	Resistivity	[$\Omega \cdot m$]
τ	Fluorescence lifetime in the presence of oxygen	[s]
τ_0	Fluorescence lifetime without oxygen	[s]
ϕ_0	Incoming light intensity	[W/m^2]

1 Introduction

Tissue vitality monitoring is an important process to be monitored with careful attention to preserve patients' health and ensure complete recovery. The essential application areas for monitoring include post-surgical monitoring of the operation area and the monitoring of transplanted organs. During these processes, many factors can influence or interrupt the healing. One of the examples is the leakage of anastomoses [1]. An anastomosis is defined as a surgical joint between organs or a joint within an organ [1]. After gastrointestinal surgeries, there is a 3-12% chance of leakage in anastomoses, which results in high mortality (10-20%) and morbidity (30-50%) rates [1]. The detection of the leakage is done based on the state of the patient and it can take up to four or more days. Therefore; the state of the leakage improves and results in a detrimental abdominal infection, which has to be treated with a second surgery [1]. However, this surgery is hazardous as the patient is already fatigued due to the previous surgery and the further improvement of the anastomosis. These complications raise a need for a method for early detection and treatment of the leakage, where the tissue conditions can be monitored after the surgery [1].

Local factors around the region of interest are the most fundamental to consider for monitoring the tissue condition. These factors are the oxygenation (O_2 and CO_2 levels), temperature, and pH [1].

Oxygenation

Oxygen concentration surrounding the tissue is crucial for energy production, which is an important indication of cell metabolism and healing [2]. It protects the region from infections due to bacteria and promotes recovery. At the beginning of healing, due to vascular damage and the oxygen consumption by the non-damaged active cells, the oxygen level surrounding the tissue is considerably low [2]. This puts the tissue in a hypoxic state, which is defined as the state of having significantly low levels of oxygen [3].

Hypoxia is essential for initial healing as it promotes inflammation, but prolonged hypoxia delays tissue healing and endangers the patient [2]. This means even though the oxygen level has to be low initially for inflammation, it has to increase to carry on with healing [2]. Therefore, monitoring oxygen concentration throughout this healing process is crucial to assess recovery.

The transportation of oxygen is done through blood, where it is carried in two forms: Dissolved oxygen in the plasma, which is about 2% of the total oxygen in the blood, and oxygen that is bound to the hemoglobin protein (98%), which functions as the oxygen carrier in the blood [4]. The oxygen-bounded hemoglobin proteins are defined as saturated, which are used to determine the oxygen saturation as a ratio of the saturated hemoglobin proteins over the total hemoglobin concentration. Dissolved oxygen on the other hand exists in the gaseous form, where its presence can be determined through partial pressures (oxygen tension) [4].

In addition to oxygen level measurements, the carbon dioxide levels can also be measured [1]. This is because; while oxygen is an indication of healthy blood circulation, an increase in carbon dioxide

indicates unhealthy blood circulation [1]. Together, they can give an outline of the condition of the tissue.

Temperature

Temperature changes indicate the body's response to the surgical wound at the beginning of healing. An increase in temperature means an inflammatory response, which is the body's initial response to the surgical wound [5]. As a result of this, local infections and complications can also be detected by measuring temperature changes [1].

pH

pH indicates a local infection or changes in the tissue structure, as it is influenced by the carbon dioxide concentration within the tissue [1].

All in all, these factors or their combinations could be used to determine the condition of the tissue and the progress of healing. For the current application of tissue monitoring, the oxygen concentration is chosen to be the detection agent as it is a factor to be considered throughout the entire tissue healing process and is directly linked to the condition of cell metabolism. In chapter 2, the existing oxygen detection methods, the selected oxygen sensing method for this project, and the research goal will be explained in detail.

2

State of the art

2.1. Oxygen sensing methods

There are four main methods to detect oxygen concentration in the body: Photoplethysmography (PPG), electrochemical measurements, photoluminescence, and NADH, which are presented in figure 2.1. Using these methods, the oxygen concentration in different regions of the body, such as the oxygen concentration in blood, at the surface of the skin, or deeper in the tissue can be measured [6]. This section will describe each method in more detail and its applicability for tissue vitality monitoring.

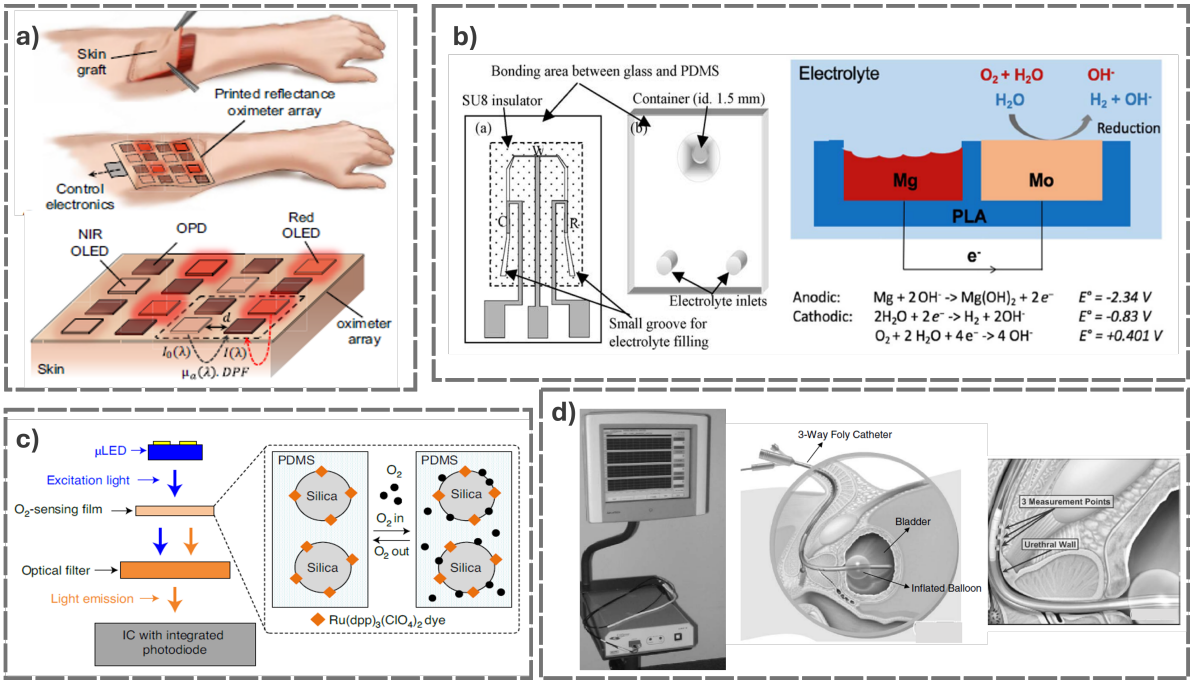

Figure 2.1: Examples of the four main oxygen sensing methods. a) Photoplethysmography (PPG) [7]. b) Electrochemical sensing: (Left) Clark cell [8] and (Right) a biodegradable galvanic pair [9]. c) Photoluminescence using ruthenium [10]. d) NADH measurement setup: (Left) Hospital measurement equipment, (Middle) Insertion of the 3-way catheter, and (Right) Three measurement points on the catheter [11].

2.1.1. Photoplethysmography (PPG)

Photoplethysmography (PPG) is an optical method that uses wavelength ranges at red and near-infrared (NIR) spectrum to assess volumetric changes in arterial blood circulation [12]. One of the application areas of PPG is oximetry where oxygen saturation is optically quantified through the con-

centrations of hemoglobin [7].

Hemoglobin is a crucial protein in the body for the transportation of oxygen in blood which exists in two forms: Oxyghemoglobin (HbO_2) and deoxyhemoglobin (Hb). At the NIR spectrum, these two forms have different molar absorptivities; which allows for the determination of their concentration through ratiometric measurement. Using the concentrations of Hb and HbO_2 (C_{HbO_2} and C_{Hb}), oxygen saturation can be calculated as[7];

$$SO_2 = \frac{C_{HbO_2}}{C_{HbO_2} + C_{Hb}} \tag{2.1}$$

The design of an oximeter consists of three main components: Photodiodes, red, and NIR light-emitting diodes (LED) [7] [13] [14]. The operation wavelengths of the LEDs have to be chosen so that Hb has a lower absorptivity than HbO_2 at one wavelength and has a higher absorptivity at the other, to be able to distinguish the concentrations of the two forms.

Additionally, there are two modes of the oximeter: Transmission and reflection mode [7]. In the transmission mode, the light from the LEDs passes through the tissue and is collected by the photodiode at the opposite side; whereas in the reflection mode, the LEDs and the photodiode are located at the same side of the tissue. One of the main disadvantages of the transmission mode oximeter is that the measurement is restricted to the area that can be transilluminated in which the light can penetrate through the whole tissue (earlobes or fingers) [7]. On the other hand, reflection mode allows for any type of area to be measured (legs or forehead) as it does not have this restriction. Therefore, using reflection mode allows for a wider range of tissue applications.

Using the principle of PPG, several devices for oximetry have been designed where three of the applications will be investigated in more detail in this paper: Reflectance oximeter array by Khan et. al. [7], deep-tissue sensing patch by Liu et. al. [13] and implantable optical probe by Guo et.al. [14]. For all of these methods, reflection mode has been used with the main components of the oximeter. Even though the operation wavelengths are different from each other, the LEDs work in red and NIR range for all the applications.

Among these three papers, Khan et.al. report a non-invasive method to determine the oxygen saturation of the pulsatile arterial blood when there is blood flow (pulse oximetry) and the relative change of SO_2 when the blood flow is restricted (reflectance oximetry). This allows for the transition from high to low oxygen concentration to be monitored even in the absence of a blood signal. It has been reported that the system is able to measure oxygen saturation with a 1.1% mean error compared to a commercial device when it is placed on the forehead [7].

Liu et.al. report a sensing patch with microneedle waveguides that pierces through the skin. This partially invasive technique allows the light from the LEDs to penetrate through the tissue more easily and makes the system more stable. The system is able to monitor oxygen saturation at the tissue (tissue oximetry), heart pulsation, and respiratory activities in addition to pulse oximetry. Experiments show that the microneedle waveguides have the potential to be used for deep-tissue sensing [13].

Lastly, Guo et.al. report an invasive optical probe which uses near-infrared spectroscopy (NIRS) for oxygenation measurements. Even though the principle of NIRS is the same as PPG; it is a more advanced version of PPG, as it provides a mixed saturation value based on arterial, capillary, and venous flow [12]. The implant consists of bioresorbable barbed structures which are designed for easier penetration and attachment; and are miniaturized for minimal invasion by using micro-scale LEDs and photodiodes. With this, it is possible to do tissue oximetry, pulse oximetry, and heart rate measurements. Experiments have shown that the implant applies to various porcine organs, but its signal-to-noise ratio (SNR) increases significantly over 8mm penetration depth [14].

Overall, all these three devices use the main principles of PPG to assess blood and tissue oxygenation. Based on these devices and the principles of PPG, it has been observed that PPG is mainly restricted to the measurements relative to blood (hemoglobin) even though there are invasive devices that can reach deeper into the tissues. As a result of this, it is only possible to know tissue oxygenation based on the assumption that hemoglobin is able to deliver oxygen to the cells; which does not give a complete insight on the changes in cellular level.

2.1.2. Electrochemical Sensing

Electrochemical measurement of oxygen relies on the principle of the chemical reactions involving the reduction of oxygen which results in the generation of current based on the amount of reduction [9].

$$O_2 + 2H_2O + 4e^- \rightarrow 4OH^- \tag{2.2}$$

The measurement setup involves galvanic metal pairs, where corrosion reactions take place at the anode of the electrochemical cell, and reduction of oxygen or evolution of hydrogen takes place at the cathodic side [9]. As a result, the lifetime of the electrochemical cell and the measurement time of the oxygen depends on the total corrosion time of the metal on the anodic side.

The most common type of electrochemical oxygen sensor is the Clark cell that is also developed by Gray et.al.[15]. It consists of platinum (Pt) as the working (WE) and the counter (CE) electrode, and silver/silver chloride (Ag/AgCl) as the reference (RE) electrode. For this application, the cell is supplied with $-0.5V$ using a potentiostat, and the negative currents are measured to quantify the oxygen tension of the visceral surface tissue ($P_{T_{O_2}}$) [15]. The results of stable measurements over 165 minutes have shown that negative currents are proportional to $P_{T_{O_2}}$, where more negative currents indicate higher partial pressures and consequently, higher oxygen concentrations [15].

In addition to Clark cells, there are different electrochemical oxygen sensor configurations in terms of biodegradability, shape, and additional measurement parameters [9] [16] [17]. She et.al. report a biodegradable, self-powered galvanic pair. Molybdenum (Mo) and magnesium (Mg) are used for the galvanic pair, where Mg is the anode and Mo is the cathode. The pair is embedded in poly-lactic acid (PLA) and immersed in saline electrolyte.

In this setup, the oxygen concentration is determined based on the spontaneous galvanic protection of Mo due to oxidation of Mg at the anode ($E^\circ = -2.34V$). This means that; Mo at the cathode does not undergo corrosion and either hydrogen evolution or oxygen reduction takes place, which is dependent on oxygen concentration. In the absence of oxygen, reduction cannot occur and hydrogen evolution reaction determines the anode-cathode reaction($E^\circ = -0.83V$); whereas in the presence of oxygen, the reduction reaction determines the voltage ($E^\circ = +0.401V$) [9]. This results in a variation of voltage which can be approximated as a linear dependence of the anode-cathode potential to the oxygen concentration until the point of saturation, where oxygen reduction dominates hydrogen evolution. Based on this, the range of the sensor is determined to be $0 - 60\% atm$ with a sensitivity of $6mV/\% atm$ oxygen during a maximum ex-vivo operation time of 66 minutes[9].

Xia et.al. report a flexible thread-based oxygen sensor that can measure oxygen concentrations at larger surfaces or local spots with high accuracy and sensitivity. The structure is based on silver threads coated with dielectric ink that are located both at the cathode and anode sides and controlled with a potentiostat at 0.55V. At the anode, chlorination of the silver thread takes place and at the cathode, water formation occurs.

$$Anode: \quad 4Ag + 4Cl^- \rightarrow 4AgCl + 4e^- \tag{2.3}$$

$$Cathode: \quad 4H^+ + 4e^- + O_2 \rightarrow 2H_2O \tag{2.4}$$

Here, the formation of water and the resulting current flowing through the cathode depends linearly on dissolved oxygen concentration.

There are two configurations of the silver threads to be used for measurement: Wire sensor and tip sensor. The wire sensor has a larger sensing area that applies to bigger regions and the tip sensor is for smaller local points on the tissue. The results show good repeatability, reversibility, and stability for these sensors for over a week. The sensitivity of the sensors reduced during this period, where more reduction has been reported for the wire-type sensor. They are calculated to be $867.8 \pm 87 \frac{nA}{mg/L}$ for the wire sensor and $1.94 \pm 0.35 \frac{nA}{mg/L}$ for the tip sensor with a limit of detection of 0.95 and 1.68ppm respectively [16].

Lastly, Li et.al. introduce a bioresorbable electrochemical sensor based on galvanic coupling for glucose, oxygen, and temperature measurement in subcutaneous tissue. The device consists of a polylactic-co-glycolic acid (PLGA) substrate, zinc (Zn) (WE), molybdenum (Mo) (CE), and molybdenum-tungsten (Mo-W) (RE) based electrodes and a sensor for current measurements to determine the change in

concentrations. For temperature measurements, an additional Mo electrode is added where voltage change is monitored. For powering, the system is connected to an external reusable control unit with a lithium battery. The results show a stable operation for 7 days in vitro and 5 days in vivo. During this period, the sensitivity remains constant at $0.08\frac{\mu A}{mM}$ for oxygen over the first 5 days; and then increases gradually to 1.92 times its initial value by the end of day 7. Besides, the sensor degrades 2 weeks after its placement inside the body and detaches from the external unit in 4 weeks. The complete degradation is then completed within 2 months [17].

In general, the electrochemical sensors allow for the determination of oxygen concentrations through the change of electrical properties in the sensor. It is possible to design sensors with different configurations depending on the target measurement area or the duration of stay in the body. One of the main limitations of these types of systems is the lifetime, as the degradation rate and the material of the electrodes are proportional to the total operation time of these devices. Additionally, based on the papers described above, the measurement area consists of the surrounding subcutaneous tissue and the surface tissue which are not based on the cellular level changes.

2.1.3. Photoluminescence

Photoluminescence is defined as the excitation of material with light energy or photons to stimulate the emission of photons [18]. To determine the oxygen concentration based on luminescence, photo-sensitive dyes are introduced to the sensor design. Some examples for these dyes include ruthenium [10] [19], platinum octaethylporphyrin (PtOEP) [20] and palladium-benzoporphyrin (Pd-MABP) [21] [22].

In the presence of oxygen; the luminescence intensity and lifetime of the photo-sensitive dye decreases, which is defined as quenching [10]. By measuring this change, the concentration of oxygen can be determined using the Stern-Volmer equation [10]:

$$\frac{I_0}{I} = \frac{\tau_0}{\tau} = 1 + \kappa_{SV}[O_2] \tag{2.5}$$

where I_0 and τ_0 are the emission intensity and the lifetime of the dye when there is no oxygen, and κ_{SV} is the Stern-Volmer constant. Based on this equation, both intensity and lifetime give an insight to oxygen concentration. In contrast to emission light intensity, the lifetime is independent of the excitation light intensity, dye concentration, filtering effects, and photobleaching [10].

The configurations for photoluminescence based sensors include hydrogel-based nanofibers [22], nanoparticles [19], wearables [20] and implants [10].

Among these configurations, Chien et.al. report hydrogel-based nanofibers, that are injectable into the interstitial tissue, where the oxygen concentration can be monitored. The fibers are excited with an external optical device, where the quenching is also monitored with a response time of up to 2.5 years [22]. Biodegradable versions of these hydrogels have also been investigated by Cybyk et. al., where different material compositions were tested. The results showed accurate oxygen measurements with linear Stern-Volmer plots for up to 35 days in vitro [23].

Zhou et.al. introduce mitochondria-specific oxygen nanosensors based on ruthenium. The nanosensors are chemically functionalized so that they target mitochondria to check intracellular oxygen activity. In vitro tests show that nanosensors can operate with constant illumination of 450nm for 40 minutes. They have high sensitivity in which their quenching response to oxygen (75%) is approximately the same as the free nanosensors in the solution (74.1%) [19].

Lim et. al. has designed a wearable sensor patch for transcutaneous oxygen monitoring ($tcpO_2$). $tcpO_2$ is used to measure the concentration of oxygen just below the skin, where a heater is used to allow more oxygen diffusion towards the skin. The intensity based photocurrent measurements at $45°C$ showed a intensity sensitivity ($\frac{I_0}{I_{30}}$) of 1.61 at 30% oxygen and a measurement range of 0-30% oxygen [20].

Lastly, Sonmezoglu et.al. report an ultrasonically powered implant with a ruthenium-based sensitive area. The oxygen concentration is characterized through phase luminometry, where the phase shift between excitation and emission is determined to calculate the lifetime:

$$\Delta\Phi = tan^{-1}(2\pi f_{op}\tau) \tag{2.6}$$

Here; $\Delta\Phi$ is the phase change, f_{op} is the operation frequency of the light source (20kHz) and τ is the lifetime. The change in the lifetime can then be related to oxygen concentration through the Stern-Volmer equation. The results show that it is possible to wirelessly monitor deep-tissue oxygenation up to 10cm with an oxygen sensitivity of $\sim 0.066°(mmHg)^{-1}$ and a phase resolution less than $0.38° Hz^{-1/2}$ [10].

In summary, the photoluminescence measurements allow oxygen to be monitored based on quenching. For some of the applications, chemical functionalization of the substances is needed to achieve cellular-level analysis. For the others, the measurement areas involve interstitial tissue and transcutaneous measurements. Most of the methods are not investigated for biodegradability whereas the investigated ones show an operation time of 35 days.

2.1.4. NADH

One of the main organelles involved in cell metabolism is the mitochondrion, which is important for energy supply to the cell. A properly functioning mitochondrion is an indication of vitality, which can be detected through the oxygen supply to the cell and oxygen demand of the cell to produce energy (ATP) [3]. The supply can already be determined from the oxygen concentration of the blood and the flow; but to determine the oxygen demand, the energy (ATP) production mechanisms and the respiratory chain components have to be considered [3].

Nicotinamide adenine dinucleotide (NADH) has the most significant oxygen sensitivity in the cellular respiratory cycle, which can be used for intracellular oxygen concentration determination [3]. Its presence indicates cellular activity and therefore a functioning energy metabolism [3]. There is inverse proportionality between NADH and O_2 in the cell as the reduction of NAD^+ to form NADH requires the absence of oxygen. In addition to this, NADH is inversely proportional to the tissue blood flow; as with more flow, more O_2 is present, which results in the oxidation of NADH that eventually decreases NADH concentration [3].

Measurement of NADH fluorescence to assess its presence is an old technique that has been established starting from the early 1950s [11]. Mayevsky et.al. use this technique to monitor mitochondrial NADH together with microcirculatory blood flow, tissue reflectance, and oxygenation with a commercially developed device (CritiView). The device consists of a catheter with 3 measurement points and is placed in the brain of small animals (gerbil and rat), the urethral wall of patients who are in the intensive care unit (ICU), and patients who undergo vascular and open heart surgeries. The use of the device allows for multiparametric monitoring where the results from the device are claimed to serve as an early warning as the measurements show the expected relationships between the measured parameters for tissue condition monitoring [11].

To summarize, NADH is an important indicator to be investigated for cellular activity which is inversely related to blood flow and oxygen. The quantification of the NADH concentration can be done through fluorescence and can then be linked to determine the oxygen concentration through ratiometric relations.

2.1.5. Selected oxygen sensing method in this project

After careful consideration of each method of oxygen monitoring for tissue vitality analysis, NADH monitoring is chosen as the most optimal method. This is because NADH gives the most insight into the oxygen concentration in the cell; in contrast to the other methods which are mostly limited to the surroundings of the tissue and the blood. Furthermore, as the detection mechanism and time are not dependent on the measurement agent, unlike the photo-sensitive dye or the metal of the electrochemical cell, there is a freedom of design in terms of the operation time and material choice. Lastly, fluorescent characteristics of NADH allow for an optical measurement where a sensor system can be designed solely based on NADH optical properties that will be directly linked to oxygen.

2.2. NADH Fluorescence Sensing

NADH exhibits fluorescent characteristics that are excitable at approximately 350nm, in contrast to its oxidized form (NAD^+) [24]. The emission spectrum of the molecule is observed at 420-550nm with an emission peak of 470nm for unbounded NADH (free) and of 440nm for protein-bounded NADH.

These two states also have different fluorescence lifetimes of 400ps for free NADH and 2500ps for protein-bounded NADH [25].

The protein-bounded form of NADH is more stable compared to the free form and stays constant throughout the respiratory cycle. In contrast, free NADH fluorescence intensity changes throughout the cycle, where it is more when the oxygen is low and less with higher amounts of oxygen. This also means that the measurement of fluorescence intensity and lifetime is mostly dependent on the free NADH. For the overall NADH measurements, the results then show higher fluorescence intensities and shorter average fluorescence lifetimes at lower oxygen concentrations [25].

In addition to NADH, there are also other molecules with fluorescence characteristics that can influence the measurements. The fluorescence responses of other molecules together with NADH are presented in figure 2.2 [25]. One of the examples would be flavins which are involved in hydroxylation and (de)hydrogenation reactions [26]. They have the same excitation wavelength as NADH with an emission peak at approximately 550nm [25]. This causes interference in the optical measurement of NADH fluorescence intensity and lifetime as a result.

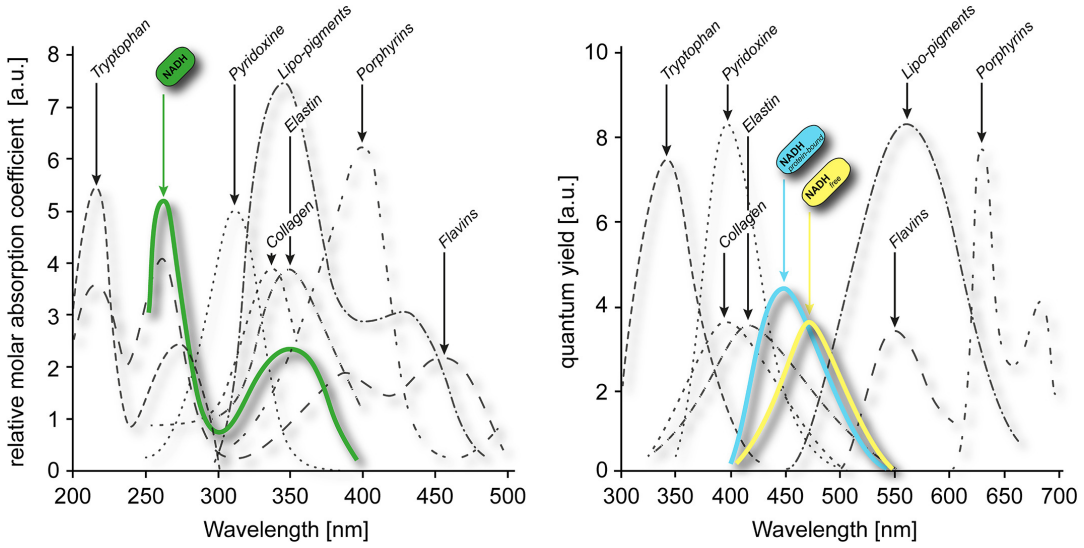

Figure 2.2: Cellular autofluorescence spectra [25]. (Left) The absorption spectrum of fluorescent molecules in the body with the NADH absorption curve shown in green. (Right) The emission spectrum of the fluorescent molecules with NADH-free emission shown in yellow and protein-bounded NADH shown in blue. The heights show the relative molar absorptivity and the quantum yield respectively which might vary between samples.

The optical measurement of fluorescence requires an excitation source (350nm) and a detector for the quantification of the fluorescence. As the emission of other fluorescent molecules in the body might interfere with this detection, together with the excitation source, an optical filter setup is required to be able to distinguish between the emission of NADH and other molecules and to remove the influence of the excitation source. The section 2.2.1 will introduce the filtering methods for the isolation of NADH emission and the principle of detection to be able to quantify oxygen concentration.

2.2.1. Filter design

Filtering of the excitation wavelength and emissions from other molecules allows for a more specific and accurate detection. The filtering methods for the determination of NADH molecules are chosen to be the interference filter and absorption layer.

Interference filters

An interference filter consists of stacks of two different materials with different refractive indexes. The working mechanism of interference filters relies on the phase shift of the light, due to the thicknesses of these layers [27]. When the incoming light hits the filter, two reflections occur: Reflection from the top of the filter (reflection 1) and at the interface of layers after light passes through one of the filter layers (reflection 2).

The thickness of an interference filter layer can be calculated based on the refractive index of the material (n) and the wavelength of interest (λ) [27]. When the thickness is $\frac{\lambda}{4n}$, destructive interference occurs, in which the incoming light is canceled due to a phase shift of $90°$ between the reflections; and constructive interference occurs when the thickness is $\frac{\lambda}{2n}$ due to $0°$ phase shift [27]. A $\frac{\lambda}{4n}$ layer is defined to be an anti-reflective layer and $\frac{\lambda}{2n}$ is named to be the absentee (spacer) layer [27].

The most basic version of these filters is the bandstop filter, which consists of multiple high (H) and low (L) refractive index layers with a thickness of $\frac{\lambda}{4n}$ [27]. As all layers are proportional to the quarter of the wavelengths, one portion of the spectrum has reduced transmission. By increasing the amount of stacks, it is also possible to reduce the transmission further.

When a spacer layer is added in between two bandstop filters, it is possible to transmit the wavelength of interest, while the surroundings are blocked. These types of special filters are called the Fabry-Perot filters [28]. The transmission spectrum of the Fabry-Perot filter and the bandstop filter is presented in figure 2.3 [27].

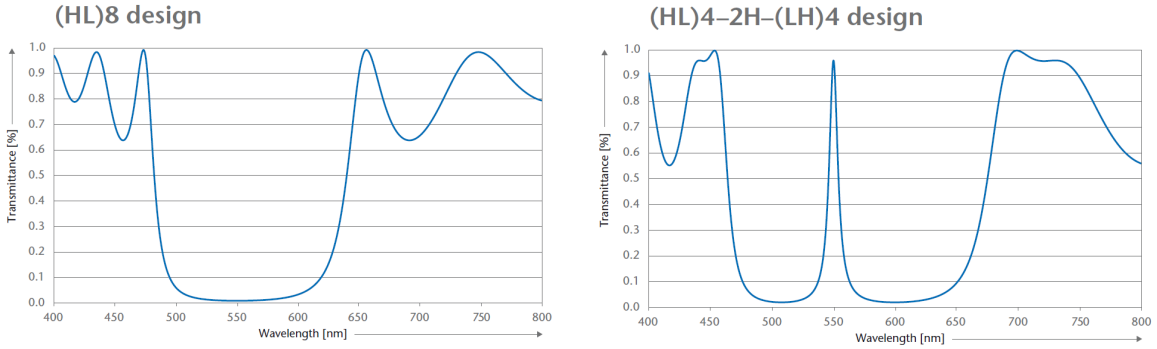

(a) Bandstop filter

(b) Fabry-Perot filter

Figure 2.3: Example for transmission spectrum of filters [27]

As shown in the figure, the bandpass region of the Fabry-Perot filter is very narrow and specific to a single wavelength. It is possible to increase the bandpass region width by introducing more spacer layers to the filter design, which will allow for a wider range of wavelengths to pass through while preventing others [27].

In addition, the filter is dependent on the angle of incidence. This is because, when the light comes with an angle, its total path in the filter layer is longer, due to the reduction of refractive index based on the angle (Snell's Law).

$$n_{angled} = n_{original} sin\theta \tag{2.7}$$

where n_{angled} is the reduced refractive index and θ is the angle of incidence. As a consequence, since the thickness of the layer is the same, the transmission spectrum shifts to lower wavelengths with decreasing refractive index as $\lambda \propto n$ at constant thickness [27].

An example of the Fabry-Perot filter is designed by Pimenta et.al. with a transmission peak at 570nm for neuron physiology assessment [28]. The filter consists of TiO_2 (H-layer) and SiO_2 (L-layer) layers and has one spacer layer that is made with SiO_2. In addition, it has 5 interchanging anti-reflective layers on both sides of the spacer layer, which corresponds to a total of 11 layers. The response of the filter has an $\sim 81.8\%$ transmission peak at 561nm, with a bandpass region of 28nm that is able to transmit more than 50% of the light. The response of the filter compared to a simulation in TFCalc3.5, together with its structure is presented in figure 2.4 [28].

The response shows that the experimental transmittance is similar to the simulation. Overall, the possibility to specify the transmission peak based on material thickness while blocking other wavelengths makes the Fabry-Perot filter design suitable for the transmission of emission of NADH.

Absorption layers

Absorption layers can be used to eliminate some of the wavelengths, as they have high absorption to a range of wavelengths while transmitting others depending on their material properties [29]. In addition

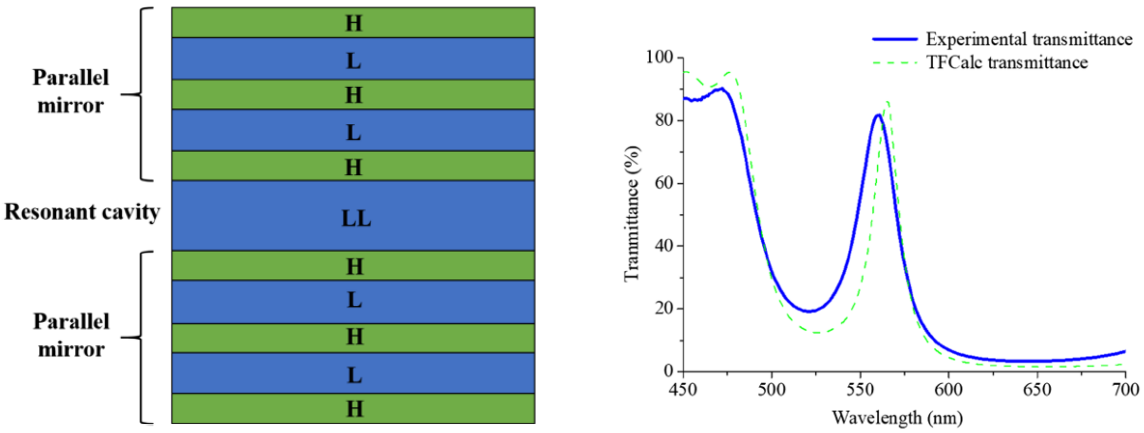

(a) Structure of the Fabry-Perot filter, designed by Pimenta et.al.

(b) Simulation results of TFCalc 3.5 vs. experimental transmission

Figure 2.4: Fabry-Perot interference filter example from Pimenta et. al. [28]

to this, the wavelengths can be shifted to different values by using the photo-sensitive properties of nanoparticles [30]. For this application, a particle with high absorption to undesired wavelengths can be chosen; which will shift this wavelength to a higher value during emission, due to a decrease in light energy. It is then important to choose a particle in which the emission does not interfere with the wavelength of interest.

To sum up, it is possible to reduce the transmission of undesired wavelengths and to limit the range of detection to the emission spectrum of NADH using these filtering techniques.

2.2.2. Detection principle

Detection of fluorescence is done through the use of photodiodes, in which the current flowing through the diode is directly proportional to the incoming light intensity. Silicon-based photodiodes are the most abundant type, which is used in many applications for the detection of broad ranges of wavelengths [31].

The detection principle is based on the absorption of silicon, where there is high absorption at shorter wavelengths that decreases for longer wavelengths [32]. At the infrared range, silicon becomes transparent. Based on this, the photocurrent generated due to a single wavelength can be defined as;

$$I_{PC} = -\frac{\phi_0 q S \lambda}{hc}(1 - e^{-\alpha W}) \tag{2.8}$$

where ϕ_0 is the incoming light intensity, q is the elementary charge ($1.6 \cdot 10^{-19} C$), S is the surface area of the diode, λ is the wavelength of the incoming light, h is the Planck's constant ($6.62 \cdot 10^{-34} Js$), c is the speed of light in vacuum ($3 \cdot 10^8 \frac{m}{s}$), α is the absorption coefficient of silicon and W is the depletion depth in which the current is generated [31].

For the measurement of current at a specific depth W, Choi et.al. introduce a gated photodiode structure. Compared to other types of photodiodes, this allows for the differentiation of wavelengths from each other, which allows for the isolation of the wavelengths of interest. The structure is built on an n-type substrate with p-well, which is presented in figure 2.5 [31]. Here, by controlling the gate voltage (V_{PG}), the depletion depth is adjusted where the photogate current can be determined for the adjusted region (I_{PG}). When a voltage V_1 is applied to the gate, the depletion depth can be defined to be W_1 and the photocurrent that flows to the output is I_{PG1} [33]. A similar case occurs for I_{PG2} when V_2 is applied. As a result, different relationships for the currents will be obtained at W_1 and W_2 since the absorption coefficients are different for each wavelength [33]. Additionally, when multiple wavelengths are applied to the same depth, this will result in a complex relationship where the wavelength with the closest absorption depth to the depletion depth will dominate the current.

By applying this wavelength detection principle to the emission spectrum of NADH, it is then possible

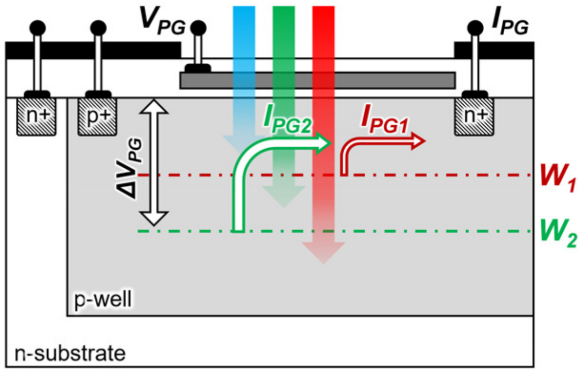

Figure 2.5: Gated photodiode structure by Choi et.al. [31]

to determine the fluorescence light intensity from the current as the photocurrent scales linearly with light intensity (ϕ_0) to determine oxygen concentration. Therefore, this detection principle is chosen to be combined with a Fabry-Perot interference filter and an absorption layer to be able to isolate the emission spectrum of NADH from the excitation source and the fluorescence of other wavelengths for accurate oxygen monitoring.

To be able to place this sensor in the body, the material properties of the design have to be considered. These properties include the ability to have contact with a living organism without harmful effects (biocompatibility), the ability to be decomposed by living organisms with biodegradation of 90% within 6 months (biodegradability), and the ability to degrade inside the human body without any abnormalities (bioresorbability) [34]. Among these three; biocompatibility is the key requirement to have any interaction with humans, where the applicability of the other two depends on the goal and the application area of the product. The choice of materials for this current application is described in the following section.

2.3. Material selection

One of the key properties of this design is determined to be the bioresorbability of the materials. This is because the sensor is designed to be placed inside the body, either for the post-surgical healing monitoring or for the tissue vitality of transplanted organs, during and after its placement in the body. When the system is not composed of bioresorbable materials, an additional surgery to remove the device is required which complicates the healing process of the patient. On the other hand, the use of bioresorbable materials allows for spontaneous absorption, removal, digestion, and disintegration when placed in the body, which eliminates the need for a secondary surgery [35].

Even though some of the current applications involve bioresorbable materials in their sensor design, the measurement of oxygen is restricted to an interstitial tissue-level analysis with short operation times [9] [17]. This raises the need for a bioresorbable oxygen measurement system that can do cellular-level detection with higher operation times.

2.4. Objective of the research

The goal of this project is to introduce the design and experimentation of a bioresorbable optical filter and detector system for NADH fluorescence sensing to measure oxygen concentration within the tissue. To achieve this goal, a bioresorbable system design that can provide more than 90% transmission of NADH fluorescence emission, while rejecting the excitation wavelength at least by two orders of magnitude will be investigated. The system consists of an absorption layer, a Fabry-Perot interference filter, and a photodetector. Each has different research questions to be answered for their design, which are listed below.

- Photodetector: How do the variable gate voltage, device dimensions, and substrate thickness influence a back-illuminated gated photodiode for the measurement of fluorescence emission of NADH?

- Fabry-Perot filter: How can a bioresorbable Fabry-Perot filter be configured to achieve a minimum transmission of 90% of the fluorescence emission (470nm) and a maximum transmission of 10% of the excitation (350nm) with minimum influence of angle of incidence?
- Absorption layer: How much reduction of the excitation wavelength (350nm) can be achieved by depositing ZnO on top of the filter and the detector as an absorption layer?

Based on these research questions, the master project consists of the determination of the optimal design considerations and materials for the absorption layer, Fabry-Perot filter, and photodetector based on simulations and experiments. Chapter 3 will explain the method of design and material choice of each component, together with the simulation results, process steps for fabrication, and the test setup for measurements. Then, chapter 4 will present the experimental results of each component, and calculations for biodegradation time followed by the discussion of the results and suggestions for future experiments in chapter 5 and conclusion in chapter 6.

3

Methods

The biodegradable optical filter and photodetector design consists of three components: The absorption layer, the Fabry-Perot filter, and the photodetector for light detection through light absorption depth in silicon [31]. In this design, the first layer encountered by the light is the absorption layer. After it absorbs some of the light or shifts some wavelengths to higher values, light passes through the Fabry-Perot filter where most of the undesired wavelengths are expected to be canceled while 470nm passes through. Lastly, the light enters the photodetector in which current is generated.

In this chapter; the principles of the design considerations, together with modelling, simulation, and processing steps will be discussed separately for each component. Then, the testing setup for each component will be introduced, which will be used for the experiments.

3.1. Absorption Layer

An absorption layer is added at the top of the device to shift the excitation source wavelength (350nm) to a higher wavelength that is not within the NADH emission spectrum. This prevents some of the excitation source light from entering the device.

3.1.1. Choice of Material

For this application; zinc oxide (ZnO) nanoparticles are chosen as ZnO is bioresorbable with a degradation rate of $4nm/hour$ in PBS [36] at 37° and has a high absorption to the ultraviolet-A (UV-A) spectrum, which contains 350nm [30]. Its absorption increases with increasing nanoparticle diameter up to 40nm after which the particles start to become opaque to UV and are completely opaque for particles greater than 70nm [30]. After 70nm, the absorbance starts to decrease due to a decrease in particle density with an increase in size [30]. Therefore, particles with 25-35nm diameter are chosen to be the optimal type. Moreover, the emission peak of ZnO is at 546nm when excited with 358nm, which is at the edge of the emission spectrum of NADH [37]. The spectral response of ZnO nanoparticles is presented in figure 3.1.

3.1.2. Process steps

The fabrication of the ZnO absorption layer is done on a 1-inch glass wafer for optical characterization, using 22 wt.% water-dispersed ZnO nanoparticle (25-35nm diameter) solution from Nanografi [38].

Before the fabrication, the glass wafers are submerged in acetone (5 minutes), isopropyl alcohol (IPA) (5 minutes), and deionized water (5 minutes) baths for cleaning. Then, they are treated with oxygen plasma for one minute to ensure better adhesion of the particles. After this, the solution is spin-coated at 1000rpm, 1500rpm, and 2000rpm for 80s, 65s, and 40s respectively. Lastly, the particles are annealed on a $200^{\circ}C$ hotplate for 1-10 minutes, where the annealing temperature and time are chosen as the intermediate values of two different ZnO protocols [39] [40].

The reason for increasing the spinning time with lower speeds is to ensure the drying of the solution

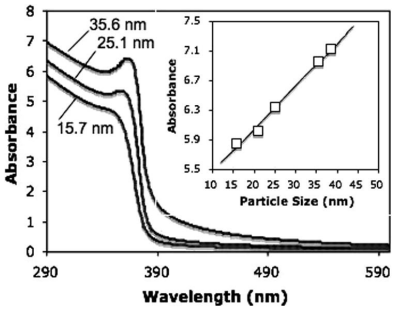

(a) Absorption of different ZnO nanoparticle diameters [30]

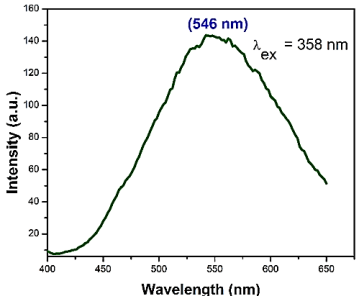

(b) ZnO emission spectrum [37]

Figure 3.1: ZnO spectral response

before annealing. Additionally, different spin rates are chosen to investigate the effect of spinning on the layer properties and thickness.

During the fabrication of the complete device, the nanoparticle solution will be drop-casted on the rest of the components as the final layer and will be left to dry under a fumehood for one hour.

3.2. Fabry-Perot Filter

Fabry-Perot filter is designed for the high transmission of the emission peak of NADH (470nm) while blocking the excitation source and the emission of ZnO nanoparticles. Several criteria are defined for the design of the filter:

- Biodegradable/bioresorbable
- High transmission for NADH spectrum
- Low transmission for excitation source (350nm) and ZnO emission ($\sim$ 546nm)
- Maximum thickness of $\sim 1\mu m$
- High tolerance to different angles of light

3.2.1. Choice of Material

To make the filter bioresorbable, silicon oxide (SiO_2) and silicon nitride (SiN_x) are chosen to be the filter layers for low and high refractive index material. They have degradation rates of $0.1nm/day$ and $0.794nm/day$ in PBS solution at $37°C$ respectively [36]. To ensure bioresorbability within patients' lifetime, the total thickness of the filter is restricted to $1\mu m$, which corresponds to 27.5 years degradation time for $1\mu m$ SiO_2 and 3.5 years for SiN_x. The actual filter is expected to have a degradation time in between these values as the layers are added interchangeably.

3.2.2. Modelling

The thickness of each filter layer is based on the refractive index of the material. The refractive indexes of SiO_2 and SiN_x are $\sim$ 1.46 and $\sim$ 2 respectively [41]. Based on this, the thicknesses of the anti-reflective layers to cancel 350nm can be calculated as;

$$t_{SiO_2} = \frac{\lambda}{4n_{SiO_2}} = \frac{350nm}{4 \cdot 1.46} = 59.93nm \sim 60nm \tag{3.1}$$

$$t_{Si_3N_4} = \frac{\lambda}{4n_{Si_3N_4}} = \frac{350nm}{4 \cdot 2} = 43.75nm \sim 45nm \tag{3.2}$$

and for the spacer layers to transmit 470nm can be calculated as;

$$t_{SiO_2} = \frac{\lambda}{2n_{SiO_2}} = \frac{470nm}{2 \cdot 1.46} = 160.96nm \sim 161nm \tag{3.3}$$

$$t_{Si_3N_4} = \frac{\lambda}{2n_{Si_3N_4}} = \frac{470nm}{2 \cdot 2} = 117.5nm \sim 120nm \tag{3.4}$$

Using these values, simulations are done to determine the optimal filter configuration.

3.2.3. Simulations

Filmetrics spectral thin film reflectance calculator is used to determine the optimal configurations for the filter design [42]. For the simulation, the medium is set to be the air, and the substrate is set to be glass. Then, a unit configuration of L-H-L-2H-L-H-L is determined to be the simplest version of the Fabry-Perot filter, where L represents the low index material (SiO_2) and H represents the high index material (SiN_x). Here, SiN_x is chosen to be the spacer layer as it degrades faster compared to SiO_2 and behaves better compared to the simulations where SiO_2 is the spacer layer.

The thicknesses of the layers are based on pre-determined thicknesses but are also changed to optimize the design. Additionally, the number of unit configurations is increased to have better prevention of 350nm and to have a larger transmission band within the NADH spectrum. The behavior of the filter with different angles of incidence is also simulated to check the tolerance of each configuration, where for all cases a shift towards lower wavelengths is observed.

Overall, four configurations with 15 layers and 3 spacer layers are determined to be built. Their layouts are presented in table 3.1.

Layer number	Material	Filter 1	Filter 2	Filter 3	Filter 4
1	SiO_2	45nm	45nm	60nm	55nm
2	SiN_x	45nm	45nm	45nm	40nm
3	SiO_2	45nm	45nm	60nm	55nm
4	SiN_x	130nm	130nm	125nm	125nm
5	SiO_2	45nm	60nm	60nm	55nm
6	SiN_x	45nm	60nm	45nm	40nm
7	SiO_2	45nm	60nm	60nm	55nm
8	SiN_x	130nm	130nm	125nm	125nm
9	SiO_2	60nm	50nm	60nm	55nm
10	SiN_x	60nm	50nm	45nm	40nm
11	SiO_2	60nm	50nm	60nm	55nm
12	SiN_x	130nm	130nm	125nm	125nm
13	SiO_2	50nm	45nm	60nm	55nm
14	SiN_x	50nm	45nm	45nm	40nm
15	SiO_2	50nm	45nm	60nm	55nm
Total thickness		990nm	990 nm	1035nm	975nm

Table 3.1: Filter configurations from simulations

Filter 1 and 2 are designed so that each L-H-L pair has the same thickness. The thicknesses are varied accordingly, to be able to have low transmission for 350nm and high transmission for 470nm. Filter 3 has the same thickness as the pre-calculated values, except for the spacer layer which is 5nm more than the calculation; and Filter 4 has anti-reflective layers with thicknesses that are 10% less than Filter 3.

The expected transmittance of these filters at 350nm and 470nm is presented in table 3.2 and their expected transmission spectrum is shown in figure 3.2.

The transmittance of the filters shows that filters 3 and 4 have wider pass-band regions compared to filters 1 and 2, and that filter 4 shifts to lower wavelengths due to 10% reduction in anti-reflection layer thickness.

Based on the simulations, these four filters were fabricated for experimentation.

Filter	Transmission at 350nm (%)	Transmission at 470nm (%)	$\frac{Transmission_{470nm}}{Transmission_{350nm}}$
1	7.05	97.7	13.85
2	7.94	95.0	11.96
3	4.18	95.4	22.82
4	4.54	84.8	18.68

Table 3.2: Transmission of filters at 350nm and 470nm

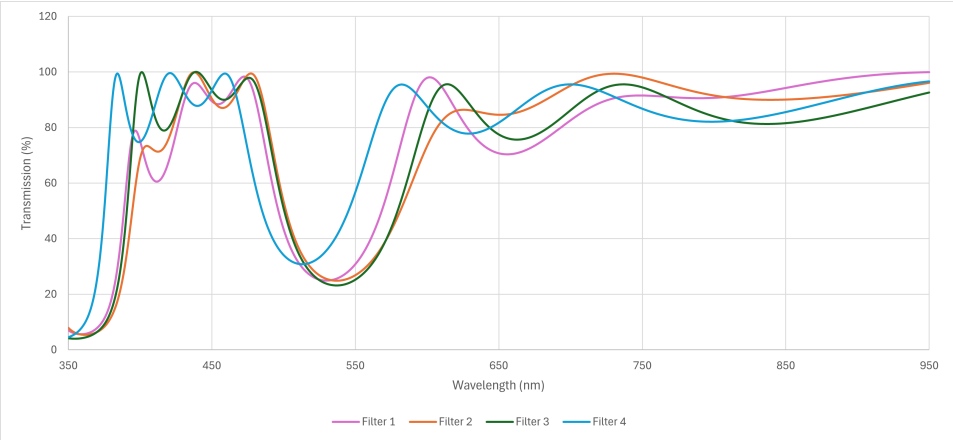

Figure 3.2: Transmittance of the simulated filters

3.2.4. Process steps

The fabrication of the filters is done on 1-inch glass wafers for optical characterization, where Oxford Instruments PlasmaPro 100 - in Kavli Nanolab/ TU Delft - is used for inductively coupled plasma-enhanced chemical vapor deposition (ICPECVD) of the filter layers. The deposition temperature is chosen to be $150°$ to ensure lower stress, based on the specifications from Oxford Instruments [43]. The gases for the deposition are SiH_4 and O_2 for SiO_2 and SiH_4 and N_2 for SiN_x. The recipe names are "Kavli SiO2 150C 59nm/min low stress +50MPa, unifor.5% (2)" and "Kavli SiN HR 150c 47.2 nm/min stress=-283MPa uniformity=1.6% n=2.1" for SiO_2 and SiN_x respectively.

Before the actual deposition, silicon dummy wafers are used to determine the deposition rate of SiO_2 and SiN_x. First, to determine the SiO_2 deposition rate, the chamber of the ICPECVD is conditioned with SiN_x without a dummy wafer to mimic the continuous deposition of the filter. Then, SiO_2 is deposited on the dummy wafer at $150°C$ for two minutes. After this, the thickness of the layer is measured with JA. Woollam Co. M200F spectroscopic ellipsometer and the deposition rate is calculated. The same process is repeated for SiN_x at $150°C$ by conditioning the deposition chamber with SiO_2.

After determining the deposition rates for both materials, the required times per layer are calculated and the filters are deposited. The deposition rate is determined on the same day as the filter deposition to ensure accurate layer deposition.

During the fabrication of the actual device, the filter will also be deposited with ICPECVD on the back side of the photodetector.

3.3. Photodetector

The purpose of the photodetector is to determine the current from one wavelength while eliminating or reducing the effect from the others [31]. For this application, the fundamental wavelength to be detected is 470nm, which is the peak emission from NADH molecules. The design, which is presented in figure 3.3, is an adaptation from Choi et.al.

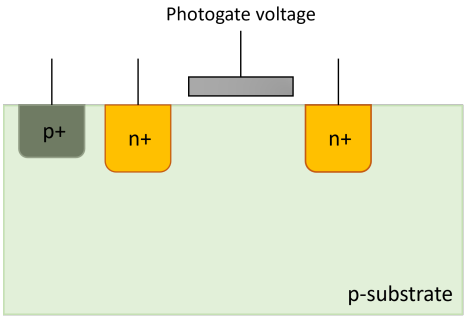

Figure 3.3: Adapted design of the photodetector

In contrast to the gated photodiode design of Choi et.al., this design lacks the deep p-well well in an n-type substrate and consists of two shallow n^+ wells within the p-substrate for current detection instead of one. Therefore, the structure has a similar layout to a transistor.

3.3.1. Modelling

Matlab was used for the characterization of the detector properties; where the intrinsic properties of the detector with no applied voltage and the required bias voltage of the shallow n^+ wells are determined based on the doping concentrations of the substrate and the wells, and based on the fundamental wavelength of 470nm. The Matlab code for this characterization can be found in Appendix A.

A few assumptions were made for these calculations. As the current detection is based on the current generated within a depletion depth, it is assumed that the incoming light illuminates the depletion region while the other parts of the device are insulated. Additionally, it is assumed that the currents generated by higher wavelengths with lower absorptivities in silicon have negligible influence on the measured current at the n^+ wells.

When light hits the depletion region, it generates electron/hole pairs. As the depletion region is void of any mobile charge and there is an electric field between the fixed electrons at the p-side and fixed holes at the n-side of the depletion region, the pair is forced towards the opposite ends of the depletion region. This results in a drift current which is dependent on the generation rate of electron/hole pairs [44]:

$$G = \frac{\alpha \lambda i_v(x)}{hc} \tag{3.5}$$

where $i_v(x)$ is the change in light intensity according to distance.

$$i_v(x) = i_{v0} e^{-\alpha x} \tag{3.6}$$

in which i_{v0} is the initial light intensity before it hits the surface of the photodetector and x is the distance [44].

The total drift current due to light (I_{lum}) can then be calculated based on the total generation in the depletion region, the elementary charge (q), and the surface area of the detector that is in contact with light (S) [44]:

$$I_{lum} = qS \int_0^W G dx = qS \int_0^W \frac{\alpha \lambda i_v(x)}{hc} dx \tag{3.7}$$

The solution of the integral then gives the total illumination current (photocurrent), which has been defined in equation 2.8. During measurement at n^+ well, the influence of this current is considerably higher than the current generated outside of the depletion region, as the currents outside the depletion region are diffusion currents that are regulated by the electron/hole concentration, mobilities, and time [44]. Hence, the current outside depletion region is considered to be negligible.

To determine the intrinsic properties and the biasing conditions, one of the n^+ wells is taken into consideration.

The intrinsic bias voltage (V_{bi}) of the material is based on temperature ($T = 300K$), the intrinsic carrier concentration of the substrate material ($n_i = 1.5 \cdot 10^{10} cm^{-3}$), and the doping concentrations of the substrate ($N_A = 1 \cdot 10^{16}\ atoms/cm^3$) and the n^+ well ($N_D = 3 \cdot 10^{20}\ atoms/cm^3$) [44].

$$V_{bi} = \frac{kT}{q} ln(\frac{N_A N_D}{n_i^2}) = 0.96V \tag{3.8}$$

Here, the intrinsic carrier concentration is chosen for silicon and the doping of the substrate is determined based on the common doping concentrations for standard p-type silicon wafers. The n^+ doping is selected based on the available doping dose and energies for ion implantation to achieve shallow implantation.

The depletion width for the case with no applied voltage (W_{pn}) can be calculated using the intrinsic bias voltage.

$$W_{pn} = \sqrt{\frac{2\epsilon_r \epsilon_0 V_{bi}}{q} \frac{N_A + N_D}{N_A N_D}} = 356nm \tag{3.9}$$

where ϵ_r is the relative permittivity of silicon (11.7) and ϵ_0 is the permittivity of free space ($8.85 \cdot 10^{-12} F/m$) [44].

To be able to detect 470nm; the depletion width has to be adjusted so that it is equal to the absorption depth of 470nm, which can be calculated from its absorption coefficient ($\alpha_{470nm} = 1.72 \cdot 10^4/cm$) in silicon [32].

$$W_{pn,new} = \frac{1}{\alpha_{470nm}} = \sqrt{\frac{2\epsilon_r \epsilon_0 (V_{bi} + V_r)}{q} \frac{N_A + N_D}{N_A N_D}} = 581nm \tag{3.10}$$

where V_r is the required reverse bias voltage to achieve this depletion width, and is equal to $1.64V$ when the substrate is grounded.

Based on the parameters defined before, the schematics to represent the modelling of one of the n^+ wells are presented in figure 3.4.

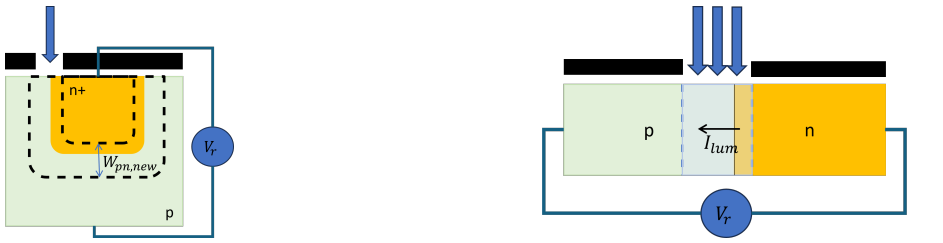

(a) One well model with reverse bias and depletion width

(b) One well model indicating the photocurrent I_{lum}

Figure 3.4: One-well models with arrows indicating the incoming light

After determining these parameters, the current response can be calculated for different wavelengths with the same intensity ($0.05W/m^2$). The current response at different depths within the substrate is presented in figure 3.5.

The response shows that, with the defined parameters, the peak of each location is within the boundaries of the spectral response of NADH (420-550nm [25]) where the peak of 470nm is observed for a depth of $0.3\mu m$. This may indicate that the current measured at the n^+ well, which is the total current with contributions from different wavelengths, is dominated by the spectral response of NADH. However, it should be noted that this model is limited to the depletion region surrounding one of the n^+ wells and does not include the effect of the gate on the current and the overall change in current over time. That's why, the detector response is investigated in more detail through Spectra simulations.

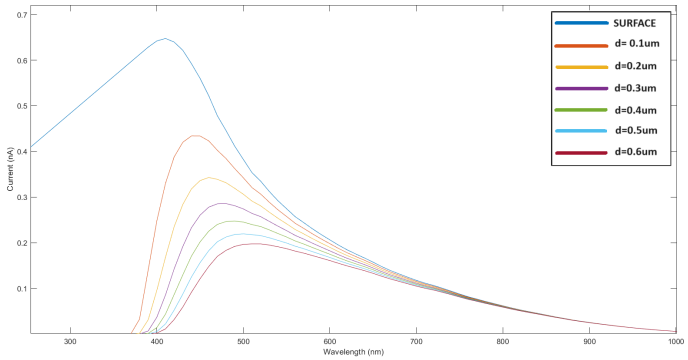

Figure 3.5: Current response at different depths within the substrate over the spectrum

3.3.2. Simulation

Spectra simulations have been conducted to determine the current for 470nm and the response of other wavelengths in more detail; where the effect of the gate voltage, the response based on changes in channel width, and n^+ well size has been investigated.

Five wavelengths are chosen for the simulation; which are 350nm, 400nm, 470nm, 570nm, and 650nm. The choice is based on the spectrum of NADH and the presence of undesired wavelengths: 350nm is the excitation wavelength that is desired to be filtered, 400nm is at the lower edge of the NADH spectrum, 470nm is the peak emission wavelength for free-NADH molecules, 570nm is at the upper edge of the NADH spectrum and also close to the emission wavelength of ZnO nanoparticles (546nm [37]) that is desired to be eliminated from the measurement, and 650nm is a red wavelength with low absorptivity in silicon.

During the simulation of the total current response, the illumination intensities of the wavelengths are adjusted so that the effect of the absorption layer and the Fabry-Perot filter are taken into consideration. This means that the intensity in comparison to 470nm is two orders of magnitude less for 350nm, as it is assumed to be filtered by the Fabry-Perot and absorbed by ZnO nanoparticles, and an order of magnitude less for 570nm as it is assumed to be filtered by the Fabry-Perot. For 400nm and 650nm, the intensities are the same as 470nm. Additionally, the intensities are kept the same as 470nm for single wavelength measurements.

The detector is chosen to be back-illuminated to prevent any reflection of light due to the presence of the gate and metal connections, and the reverse bias voltage is set to be the same as the calculation (1.64V). Then, three tests are conducted to determine the most optimal design, where the length of the device is not taken into consideration as it only contributes to the magnitude of the current but not the current related to changes in wavelength or light intensity:

- Determination of the gate voltage
- Determination of the channel width and n^+ well size
- Determination of substrate thickness

Determination of the gate voltage

During the application of gate voltage, the voltage value influences the formation of the channel. To be able to change and control the channel depth without reaching saturation, the detector has to be operated at the subthreshold conditions ($V_{GS} < V_{th}$).

Since both n^+ wells are supplied with the same reverse bias voltage ($V_r = 1.64V$), V_{GS} can be calculated from both and is equal to $V_G - V_r = V_G - 1.64V$, and the threshold voltage is calculated from the intrinsic properties to be 0.38V in which there is a 20nm SiO_2 layer in between the gate and the substrate as the dielectric material. This means that for the subthreshold condition, the gate voltage has to be between $0 - 2.02V$ to form an n-type channel. Therefore, five values of gate voltages have been simulated with different intensities ($1\mu W/m^2$ - $20\mu W/m^2$) of 470nm: 0V, 0.5V, 1.3V, 1.85V, and

1.95V. For this, the simulation conditions are $5\mu m$ n^+-well width, $100\mu m$ channel width, and $580nm$ substrate thickness, which is the same as the absorption depth of 470nm.

Based on these simulations, 1.3V is determined to be the optimal gate voltage. That's because, with higher values of voltage (1.85V and 1.95V), the saturation is reached faster which prevents the detection of higher intensities but also fails to detect minor changes in the current with lower intensities; and with lower voltages (0V and 0.5V) since the channel depth is shallower and almost non-existent, the magnitude of currents are much lower for 470nm, which prevents the distinction from other wavelengths.

In addition to this simulation, a secondary simulation is done to calculate the percentage of other wavelengths compared to 470nm and to the total current with the same simulation conditions but with a light intensity of $20\mu W/m^2$ for 470nm. For this application, three gate voltages are applied: 0V, 1.3V, and 1.65V. The percentages are presented in tables 3.3 and 3.4.

Wavelength (nm)	0V w.r.t 470nm (%)	1.3V w.r.t 470nm (%)	1.65V w.r.t 470nm (%)
350	66.96	25.29	26.81
400	96.41	110.4	116.9
570	65.61	68.68	64.58
650	45.11	50.11	46.45

Table 3.3: Percentage of currents of test wavelengths w.r.t 470nm at different gate voltages

Wavelength (nm)	0V w.r.t total current (%)	1.3V w.r.t total current (%)	1.65V w.r.t total current (%)
350	47.64	8.88	8.63
400	34.46	38.63	37.62
470	35.82	35.03	32.22
570	23.46	24.04	20.77
650	16.11	17.55	14.94

Table 3.4: Percentage of currents of test wavelengths w.r.t total current at different gate voltages

From these three, the optimal gate voltage is also determined to be 1.3V based on the low percentage of 350nm compared to other wavelengths and the higher percentage of 470nm, except for 400nm. The percentage of 400nm is adjusted later by the optimization of the substrate thickness, which will be explained in more detail in "Determination of substrate thickness".

Determination of the channel width and well width

Channel width and n^+-well width are important as they affect the current detection. A wider channel width allows for a larger detection area which increases current as more electron/hole pairs can be generated within a larger area. In addition, a wider n^+-well decreases the detection time of the current as more current can be collected with a larger well. This then causes a faster recognition of the current. For this simulation, several channel widths and n^+-well widths are tested to determine the most optimal configuration for the detector to be sensitive to 470nm with minimal influence from other wavelengths. The conditions for all the tests include a gate voltage of 1.3V, a bias voltage of 1.64, a light intensity of $20\mu W/m^2$ for 470nm, and a substrate thickness of 580nm.

The channel widths of $60\mu m$, $100\mu m$, and $150\mu m$ with n^+-well widths of $5\mu m$, $15\mu m$ and $25\mu m$ are simulated and the percentage of current of each wavelength with respect to 470nm and the total current is presented in tables 3.5, 3.6 and 3.7.

Wavelength (nm)	$60\mu m$ (%) (470nm)	$100\mu m$ (%) (470nm)	$150\mu m$ (%) (470nm)	$60\mu m$ (%) (total)	$100\mu m$ (%) (total)	$150\mu m$ (%) (total)
350	113.4	25.29	8.06	81.56	8.88	2.27
400	156.2	110.4	118.4	99.48	38.63	33.42
470	100	100	100	90.23	35.03	28.27
570	123.4	68.68	61.09	90.29	24.04	17.25
650	135.1	50.11	33.02	94.85	17.55	9.32

Table 3.5: Percentage of currents of test wavelengths with different channel widths for $5\mu m$

Wavelength (nm)	$60\mu m$ (%) (470nm)	$100\mu m$ (%) (470nm)	$150\mu m$ (%) (470nm)	$60\mu m$ (%) (total)	$100\mu m$ (%) (total)	$150\mu m$ (%) (total)
350	17.45	8.23	49.42	4.44	2.34	10.27
400	123.2	115.2	119.1	31.21	32.54	24.82
470	100	100	100	25.74	28.45	20.96
570	56.97	56.66	30.73	14.47	16.01	6.41
650	25.15	30.35	8.83	6.38	8.57	1.83

Table 3.6: Percentage of currents of test wavelengths with different channel widths for $15\mu m$

Wavelength (nm)	$60\mu m$ (%) (470nm)	$100\mu m$ (%) (470nm)	$150\mu m$ (%) (470nm)	$60\mu m$ (%) (total)	$100\mu m$ (%) (total)	$150\mu m$ (%) (total)
350	75.22	28.59	41.09	45.52	9.78	15.83
400	102.7	111.2	111.0	62.10	37.89	42.56
470	100	100	100	60.55	34.43	38.50
570	90.26	66.74	73.55	54.60	22.85	28.21
650	84.26	47.58	59.51	50.96	16.17	22.91

Table 3.7: Percentage of currents of test wavelengths with different channel widths for $25\mu m$

Based on these percentages, four configurations are chosen to be the most optimal: $5\mu m$ wells with $100\mu m$ and $150\mu m$ channel widths, and $15\mu m$ wells with $60\mu m$ and $100\mu m$ channel widths. The reason behind choosing these configurations is fundamentally based on the percentage of 350nm compared to 470nm, which is desired to be as low as possible. Still, the percentage of 400nm is higher than 470nm, which has to be reduced to be able to have 470nm as the fundamental wavelength.

Determination of substrate thickness

Throughout the determination of optimal gate voltage, channel width, and n^+-well width; the substrate thickness is kept the same as the absorption depth of 470nm (580nm). However, with this thickness, it is observed that 400nm dominates the current. As the current detection is dependent on the depletion width and the absorption depth in silicon, a different substrate thickness has been tested for the detector to be able to cancel out the influence of 400nm.

The absorption coefficient of 400nm ($\alpha_{400nm} = 9.52 \cdot 10^4 cm^{-1}$) corresponds to an absorption depth of $\frac{1}{\alpha_{400nm}} = 105nm$ [32]. As the detector is back-illuminated, increasing the substrate thickness at least by 105nm, is expected to reduce the effect of 400nm. Therefore, the substrate thickness with 700nm is tested to simulate this effect. The percentages after this change for the four optimal configurations are presented in table 3.8.

The simulation shows that by increasing the thickness of the substrate, the effect of 400nm can be reduced. It should be noted that it is not completely removed, which might be due to diffusion currents that are close enough to reach the depletion region during the simulation period ($10\mu s$), which will contribute to the current. Moreover, inconsistency is observed for $15\mu m$ wells with $60\mu m$ channel configuration when the substrate thickness is increased. This may be because of having a smaller detection area due to a shorter channel, which may result in smaller magnitudes of current with higher

Configuration	580nm substrate (%)	700nm substrate (%)
$5\mu m$ wells with $100\mu m$ channel	110.4	87.69
$5\mu m$ wells with $150\mu m$ channel	118.4	91.87
$15\mu m$ wells with $60\mu m$ channel	122.8	40.07*
$15\mu m$ wells with $100\mu m$ channel	115.2	92.32

Table 3.8: Ratio of 400nm and 470nm with different substrate thicknesses. *Inconsistent and unstable currents

deviations. Still, as a reduction of 400nm is observed with 700nm substrate, it is chosen to be the optimal substrate thickness.

In addition to these tests, the effect of change in the intensity of light and pulsed light is investigated. For this, the configurations are tested for the minimum detection intensity of 470nm, which is determined to be $1\mu W/m^2$. Below this intensity, the hole diffusion currents start to dominate the response. The same observation was observed for the pulsed light. The plots for minimum light intensity determination for the optimal configurations are presented in Appendix B.

Overall, four configurations with different channel thicknesses and n^+-well widths are chosen to be manufactured, where 1.3V is the optimal gate voltage and 700nm is the optimal substrate thickness for measurement.

3.3.3. Choice of material

One of the main goals of the detector is its bioresorbability. Therefore, it should be composed of materials that are compatible with the human body and with spontaneous disintegration. The bulk material of the detector is silicon, due to its optical properties that allow for separate wavelength detection. However, it has a biodegradation rate of $4.1nm/day$ ($37°C$ in PBS), which corresponds to a degradation rate of approximately 200 years for a $300\mu m$ thick silicon wafer [36]. Therefore, to shorten the degradation time, the wafer has to be thinned. In addition to this, as mentioned previously, back-illumination is needed to be able to prevent any reflections. This means that the thinning of the wafer to a predetermined value of 700nm is essential both to achieve bioresorbability conditions and to be able to do accurate optical measurements based on the absorption depth of 470nm. By thinning the wafer, it is possible to achieve a degradation time of 171 days in PBS at $37°$, which is approximately 6 months. Moreover, for the rest of the detector, molybdenum (Mo) is chosen for the metal contact, SiO_2 is chosen as the dielectric material and protection layer, and SiN_x is chosen as the hard mask for thinning the wafer. Mo has a degradation rate of $0.2 - 0.6nm/hour$ in Hank's solution at $37°C$; and for SiO_2 and SiN_x, since the thicknesses that are used are low, the slow degradation rate ($0.1nm/day$ and $0.794nm/day$) is not expected to prevent the bioresorbability of the device [36]. It should be noted that the degradation rates of these materials are restricted to certain experimental conditions of solution, temperature, and pH; which gives a limited indication of what will happen in the body. In the end, the degradation time will depend on the location of the body and its conditions.

The dopings of the n^+ wells and the p^+-well are done with phosphorus (P) and boron (B). To make sure their presence does not influence health, the amount of dopants in the body has to be determined and compared with the daily consumption dose. For boron, the daily upper limit of consumption is 20mg, and for phosphorus, it is approximately 700mg [45]. Assuming a maximum doping concentration of $1 \cdot 10^{21} atoms/cm^3$ and a maximum well volume of $1cm^3$, which is significantly larger than the μm-sized structures of the detector, the mass of the dopants can be calculated as 17mg for boron and 206mg for phosphorus. This shows that the amount of dopants inside the device is lower than the daily upper limit. Since silicon degradation is expected to be within $\sim$ 6 months, the resulting dose is much lower than the daily dose.

All in all, the thinning of silicon and the choice of materials allow for a bioresorbable detector design that can be used for wavelength-specific detection.

3.3.4. Mask Design

A mask has been designed for the lithography processes of $6mm \cdot 6mm$ dies based on the pre-determined configurations in which half of the mask is used for the fabrication of the photodetector, while the other

half is used for another project.

There are two versions of the same detector configuration: 2 n^+-wells separated by a channel and 3 n^+-wells, where each pair is separated by a channel. They are presented in figure 3.6.

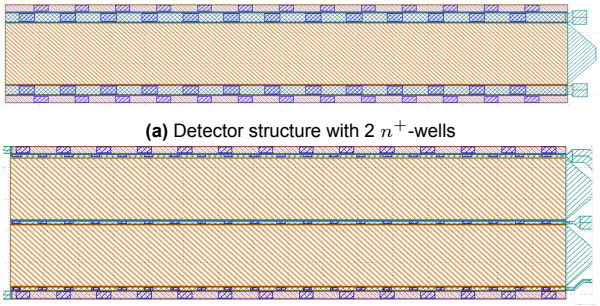

(a) Detector structure with 2 n^+-wells

(b) Detector structure with 3 n^+-wells

Figure 3.6: Structures in the mask design. (Blue) N-wells for the reverse biasing, (Purple) P-wells for the substrate biasing, (Orange) Gate, (Navy blue) Location for the via opening on the wells. All the structures are covered with (Brown/Green) molybdenum interconnect for the biasing.

Here, figure 3.6a consists of two n-wells (blue) for the reverse bias and two p-wells (purple) for the biasing of the substrate, which are separated by the sensitive area that is controlled by the gate (orange). Unlike the 2-well structure, figure 3.6b consists of three n-wells for the reverse bias and two p-wells at the boundaries of the device for substrate biasing. In this version, two channels are present between the n-wells. The reason for having this version is to have a larger sensitive area (orange) while keeping the device dimensions smaller compared to the situation where the 2-well structure is duplicated.

Within the mask, there are thinned regions for optical testing and non-thinned regions for the electrical behavior characterization tests of the transistors. The transistors in the non-thinned regions are replicas of the ones in the thinned regions to make sure the behavior of the transistor is not affected by thinning. Therefore, the choice of design is based on the structures in the thinned regions, where the channel widths and n^+-well widths are chosen based on the simulation results and the channel length varies according to the space available within the thinned region of the mask (a total area of $800\mu m \cdot 1800\mu m$). The configurations present in each part are presented in table 3.9.

Test type	Channel length (μm)	Channel width (μm)	n^+-well size (μm)	n^+-well number
Optical	796	150	5	2
Optical	796	150	5	3
Optical	796	100	5	2
Optical	796	100	5	3
Optical	796	60	15	2
Optical	796	60	15	3
Optical	796	100	15	2
Optical	796	100	15	3
Optical	254	150	5	3
Optical	254	100	5	3
Optical	254	96.5*	15	3
Electrical	796	150	5	2
Electrical	796	100	5	2
Electrical	796	60	15	2
Electrical	796	100	15	2
Electrical	254	150	5	3
Electrical	254	100	5	3
Electrical	254	96.5*	15	3

Table 3.9: Devices in the mask. *The channel width is reduced from $100\mu m$ due to availability of space.

The mask consists of nine images, which are presented in figure 3.7.

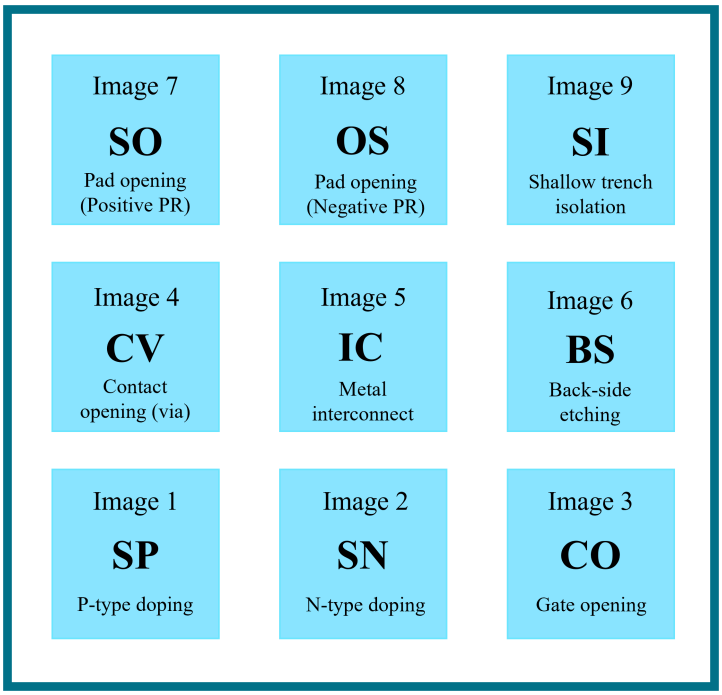

Figure 3.7: Images of the mask. SP: Shallow P-type doping, SN: Shallow N-type doping, CO: Contact opening for the gate, CV: Contact opening for via, IC: Metal interconnect, BS: Back side opening, SO: Pad surface opening (positive photoresist), OS: Pad surface opening (negative photoresist) and SI: Shallow trench isolation.

During the design, the minimum dimension between structures of an image is chosen to be $1.5\mu m$ as mask fabrication has a resolution of $1\mu m$ and the minimum distance within structures of different images is set to be $0.5\mu m$ to compensate for any misalignment during lithography. Additionally, to check the alignment of the images, Vernier scales are added. An example of Vernier scales is presented in figure 3.8.

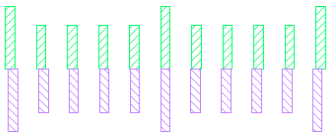

Figure 3.8: Vernier scales. (Green) Vernier scales from image 9 (shallow trench isolation) and (Purple) image 1 (p-type doping). Image 9 is used as the base alignment mark.

Here, green and purple scales are from different images, where the center marks are aligned with each other. The first small marks to the left and right have a misalignment of $0.1\mu m$ and the ones next to those have a misalignment of $0.2\mu m$. The misalignment increases up to $0.5\mu m$ until the larger marks at both ends of the scale. When there is perfect alignment, this is how the scale should look; whereas when there is misalignment, the alignment of the originally misaligned marks will be observed at the location equal to the misalignment amount.

In addition to Vernier scales, other test structures are added for resistivity (Van der Pauw), etching, and contact resistance (Transfer length method). The examples for test structures are presented in figure 3.9.

Van der Pauw structures

Van der Pauw structures are used to determine the resistivity of the substrate, p^+-doped region, n^+-doped region, and the metal; which is then used to determine the doping concentration of the substrate and the doped regions [44]. For the metal, it is present to determine its resistance.

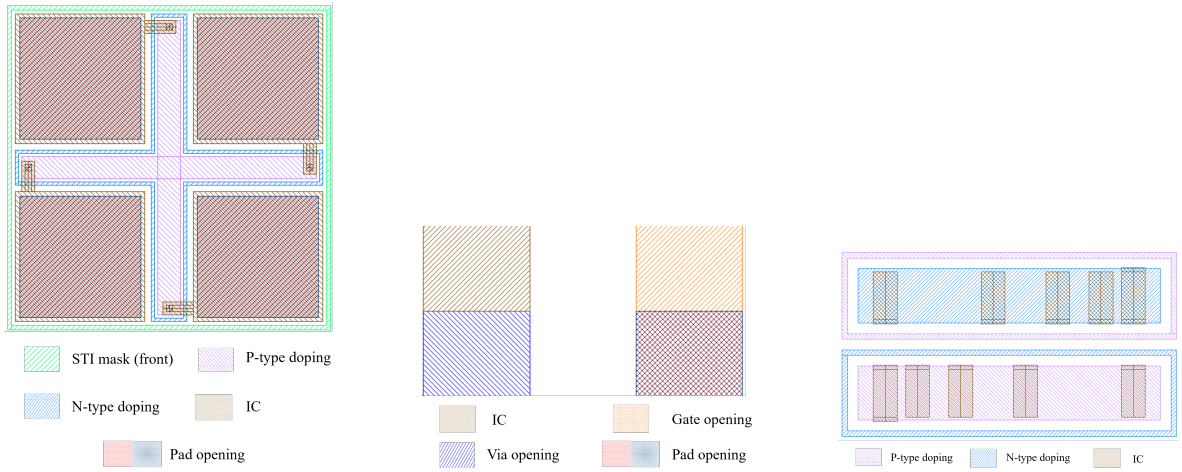

(a) Van der Pauw test structure **(b)** Etching test structure **(c)** TLM test structure

Figure 3.9: Test structure

The principle of Van der Pauw structures is based on a 4-point probe measurement, where an example of the structure is presented in figure 3.9a. The four brown regions in the figure are the contact locations for the measurement. The resistivity is determined by the sheet resistance, based on current and voltage measurements at the adjacent contact locations.

$$R_s = \frac{\pi}{ln2} \frac{R_{34,12} - R_{12,34}}{2} \tag{3.11}$$

where $R_{34,12}$ is the resistance calculated from the voltage between the two adjacent contacts V_{34} and the current between the remaining contacts I_{12}, and vice versa for $R_{12,34}$ [46]. From the sheet resistance, the resistivity is then calculated.

$$\rho = R_s t \tag{3.12}$$

where t is the thickness of the doping region or the metal.

Etching test

The etching test is used to determine the etching and deposition rates, and the accuracy of etching and deposition of these layers. This is done by using a profilometer, where the thickness is determined and then divided by the time of etching/deposition to determine the rates. The test structure for this mask is presented in figure 3.9b. Here, blue represents the etching of the vias for contact, brown represents the metal deposition, orange represents the gate opening and red/navy represents the pad opening.

Transfer length method (TLM)

TLM is used to determine the contact resistance between the metal and the doped regions (both n^+ and p^+) to ensure good contact. A low contact resistance indicates better contact between the metal and the doped regions. The structure of TLM is presented in figure 3.9c.

The structure is organized on either an n^+ type (blue) or a p^+ type (purple) region, where metal contacts (brown) are located at a distance that doubles with each placement of metal. Then; the resistance is measured between the first metal and the rest, where a linear plot is generated with respect to distance (L). The y-intercept of this plot gives double the contact resistance ($2 \cdot R_C$), the magnitude of the x-intercept gives double the transfer length (L_T) and the slope gives $\frac{R_S}{w}$ which can be used to calculate contact resistance (R_C) [47].

$$R_C = \frac{R_s L_T}{w} \tag{3.13}$$

where w is the width of the tested area.

Using these test structures allows for close monitoring of the detector fabrication process steps to prevent any issues at each fabrication stage. The upcoming section will detail the process steps for

detection production while introducing each mask image and its specific purpose. The complete mask design for the detector can be found in Appendix C.

3.3.5. Process steps

The construction of the photodetector is done on a $< 100 >$ 4-inch $300\mu m$ thick, double-side polished (DSP), p-type (Boron) silicon wafer with low resistivity (0.17-0.23 Ohm-cm), which is purchased from Siegert Wafer. The process steps will be explained for the thinned region and a 2 n^+-well detector in the non-thinned region.

1) Shallow Trench Isolation (STI)

After the etching of the alignment marks for the wafer stepper to both sides of the wafer, the shallow trench isolation image is exposed to the wafer (Image 9). STIs are needed for the thickness control of the wafer during back-side etching. For this purpose, the STI is etched with plasma etching to a depth that is equal to the desired substrate thickness for the detector (700nm). They are located around the thinned region so that when the thickness of 700nm is reached from the back side, the regions with STI will become transparent. In addition to this, they are added to isolate the transistors at the non-thinned regions to make sure the biasing of one does not affect the other.

After the etching of the STI, a 20nm thermal oxide layer is grown (dry oxidation) for protection. Figure 3.10 shows the STI structure and process steps.

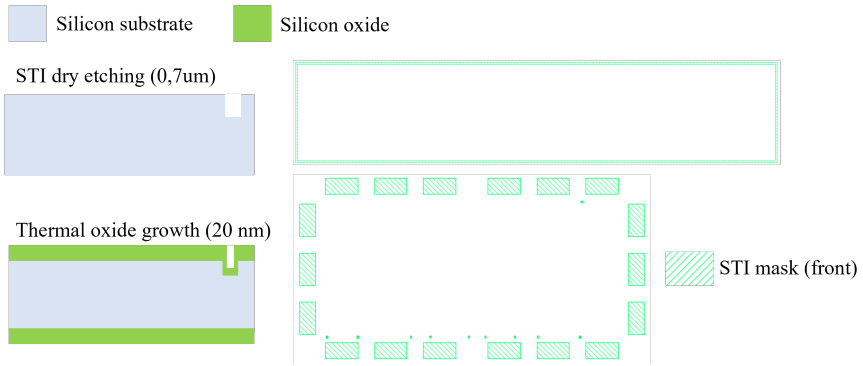

Figure 3.10: STI etching and thermal oxidation

2) P-type doping

Image 1 (SP) is exposed for p-type doping. The doping with boron is done at an external company (Ion Beam Services (IBS)), with an implantation dose of $3 \cdot 10^{15}\ ions/cm^2$ at 15keV. The resulting structure is shown in figure 3.11.

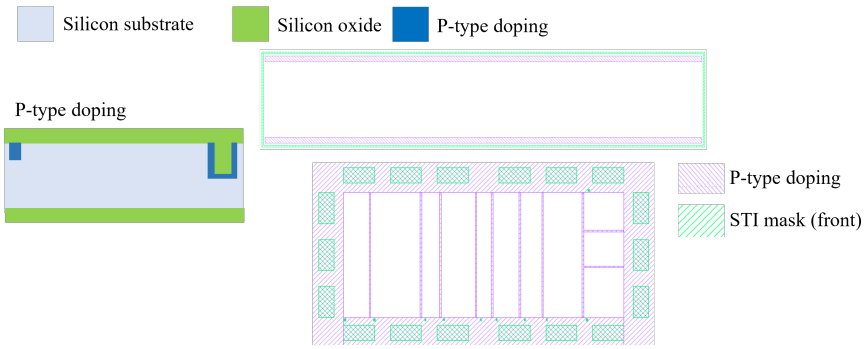

Figure 3.11: P-type doping

3) N-type doping

Image 2 (SN) is exposed for n-type doping. The doping with phosphorus is done at an external company (Ion Beam Services (IBS)), with an implantation dose of $6 \cdot 10^{15}\ ions/cm^2$ at 20keV. The resulting

structure is shown in figure 3.12.

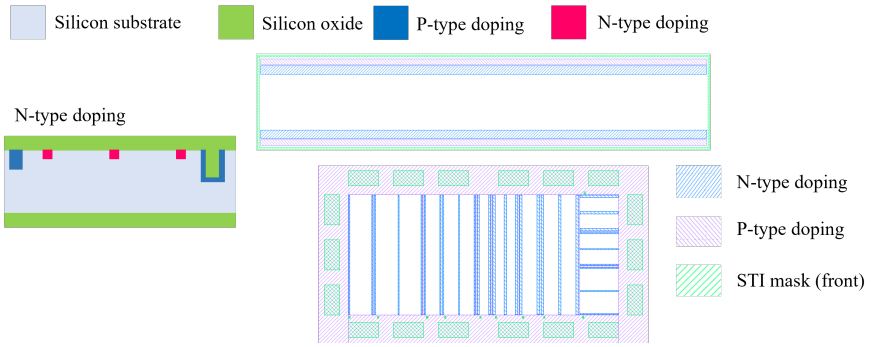

Figure 3.12: N-type doping

After the doping, the wafer is annealed at $1000°C$ by wet oxidation to also form 80nm oxide.

4) Gate opening
Image 3 (CO) is exposed to open the gate. Then, the 100nm oxide (20nm from protection and 80nm during annealing)on top of the gate is etched with wet etching, using 1:7 buffered HF (BHF) at room temperature. After this, 20nm oxide is thermally grown at $1000°C$ (wet oxidation) to be the gate oxide. This process also contributes to the annealing of the dopants. The result is shown in figure 3.13.

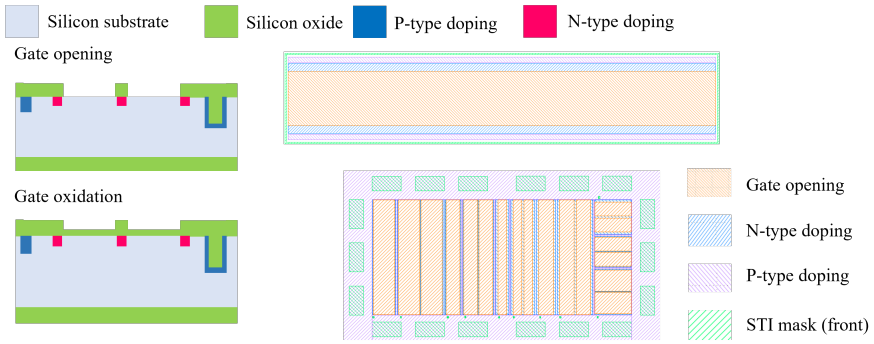

Figure 3.13: Gate opening and oxidation

5) Contact opening
Image 4 (CV) is used to etch the contact openings for the n^+ and p^+ wells. The etching of the 120nm oxide (20nm from dry oxidation and 100nm from wet oxidation) is done with 1:7 BHF. The mask image and the structure are shown in figure 3.14.

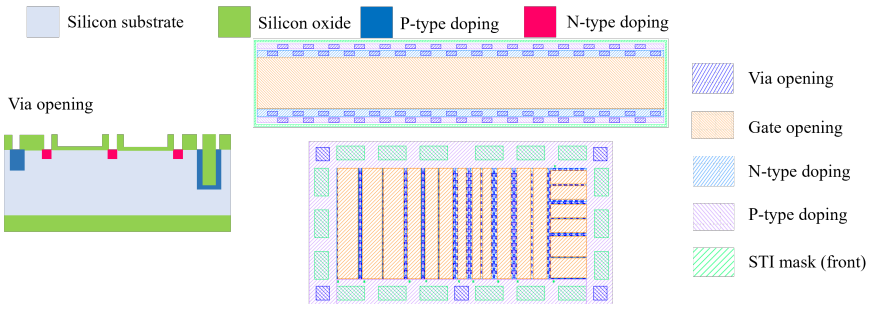

Figure 3.14: Contact opening

6) Metal deposition and interconnect
After contact opening, 500nm molybdenum is deposited at $350°C$. Then, image 5 (IC) is exposed to the wafer. To form the interconnect layer, wet etching of Mo is done with hydrogen peroxide (H_2O_2). Since wet etching is isotropic, the dimensions of the interconnect mask are chosen so that there is a tolerance for the 500nm under etch. After the etching and alloying of Mo, $2\mu m$ PECVD oxide to the frontside and $300nm$ PECVD nitride to the frontside and the backside are deposited as the protection during back-side etching. The resulting structure is presented in figure 3.15.

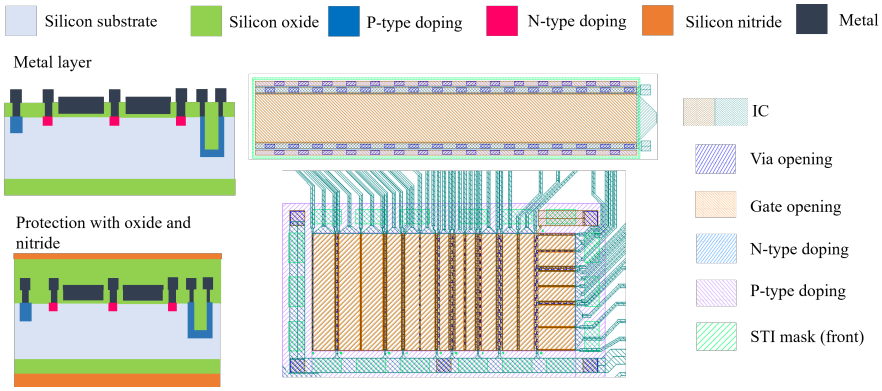

Figure 3.15: Metal deposition and interconnect

7) Back-side etching
Image 6 is exposed for the back side etching and the hard mask (PECVD nitride and thermal oxide) is removed.

Most of the back side etching is done with 25wt. % tetramethylammonium hydroxide (TMAH) with 10% IPA at $85°C$, where it selectively etches $< 100 >$ silicon compared to $< 111 >$ plane . As a result, an angle of $54.74°$ is present between the mask and the silicon substrate [48]. The formed shape is presented in figure 3.16.

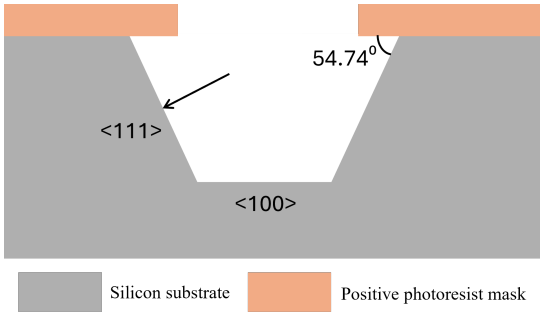

Figure 3.16: TMAH etching profile

Additionally, the back etching increases the fragility of the wafers, as the wafers become thinner at certain locations. The size of the back etching region is chosen to be $3mm \cdot 3mm$ so that the wafer stays stable and the back etching of the whole device area is possible. This means that half the area of the die will be thinned.

The wet etching is done until $50\mu m$ is left, where the rest of the etching is done with plasma etching. The process steps for the back etching are presented in figure 3.17.

8) Pad opening
Two possibilities are considered for opening the pads for wire bonding: Positive and negative photoresist (SU8), where two separate images are designed (Image 7 and 8). After the image's exposure

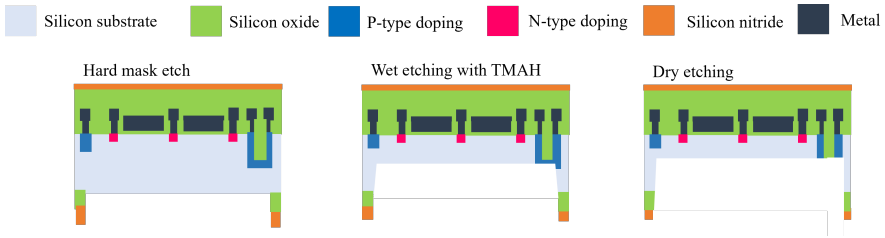

Figure 3.17: Back side etching

based on the photoresist type, the pads are etched by plasma etching of the $300nm$ nitride and $2\mu m$ oxide at the front side. Then, $2\mu m$ PECVD oxide is deposited at the back for protection.

A possibility to use SU8 is considered to increase the stability of the wafer during the testing period, as the SU8 will stay at the parts except for the pad openings which will create a support layer after back etching. It will not be present in the device, as it is not biodegradable.

After the process steps are completed for each component, two different test environments are required to investigate the optical properties of the Fabry-Perot filter and the ZnO absorption layer and to analyze the current response of the detector. The setup requirements and the testing method are explained in the following section.

3.4. Test setup

The testing of the Fabry-Perot filter and the ZnO absorption layer is done separately from the testing of the photodetector. This is to ensure that the optical properties of the filter and the absorption layer fulfill the requirements. Therefore, two setups are required: Optical testing setup and current measurement setup. In addition to these setups, the thickness of the ZnO layers is measured with Bruker Dektak XT profilometer.

3.4.1. Optical Test Setup

The testing setup consists of an Ocean Optics DH2000 Deuterium Tungsten Halogen lamp, a 1-inch sample holder, a rotating stand, two convex lenses on both sides of the sample holder, an Ocean Optics Flame-S-VIS-NIR-ES spectrometer, and two Thorlabs optical fibers (M151L01). The picture of the setup is presented in figure 3.18.

The light from the lamp passes through the optical fiber and is then adjusted by the lens so that the rays are parallel to each other. After passing through the sample, it is focused by the lens to pass through another optical fiber, where it is collected by the spectrometer. The measurement with the spectrometer is done using OceanView 2.0.16 spectroscopy software by Ocean Insight. For the measurement, the integration time of the software is set to be 10ms, and 5 scans are done for an average result.

The measurements of the sample are done at different angles of $-60°$ to $60°$ with respect to the perpendicular orientation to the light ($0°$), with $15°$ increments to determine the effect of different angles of incidence. Three orientations of the sample within the sample holder are then tested to get an average result for the overall sample.

3.4.2. Photodetector Current Measurement Setup Concept

The testing setup of the photodetector should consist of a monochromator and a printed circuit board (PCB) to determine the current at the n^+ well. For this setup, the currents from one well of the detector are expected to be low (orders of nano ampers based on the simulation). Therefore, the PCB design should consist of an amplifier to amplify the current magnitude and a small resistor at the output ($\sim 1\Omega$) to measure the current across.

After putting the detector in a sample holder with a rotating stand, the desired wavelength has to be sent with the monochromator and the current response has to be measured at the output of the PCB. In addition, it is also possible to measure the current response to the whole spectrum by using the Ocean Optics DH200 Deuterium Tungsten Halogen lamp. Here, to understand the actual response to 470nm,

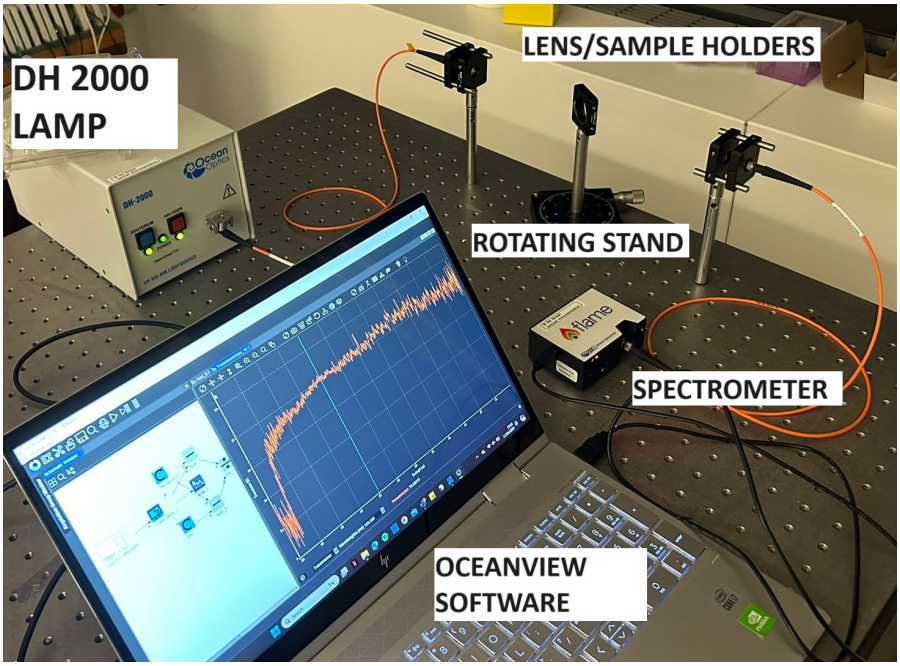

Figure 3.18: Optical test setup

it is essential to determine its response with respect to other wavelengths.

For the final combination of the device, it is expected to use the same measurement setup as for the photodetector; whereas for the filter and absorption layer combination, the optical test setup has to be used. The results obtained for these components are presented in chapter 4.

4

Experiments and results

This chapter is dedicated to the experimental progress of the project, where the experimental results of the ZnO layer and the Fabry-Perot filter, and the pre-fabrication test results of the photodetector will be presented.

At the end of the project, it was possible to optically test multiple samples of the ZnO absorption layer with different spinning rates and annealing times, and the four configurations of the Fabry-Perot filter, together with the surface characterization of the ZnO absorption layer. Then, the best protocol for ZnO is chosen based on the cancellation of 350nm and the tolerance to different angles of incidence to be combined with the Fabry-Perot filter. The combination of the two is then optically tested to determine the response of the filter-absorption layer configuration.

For the detector, tests on Mo etching rate in H_2O_2 and back-side etching were done to ensure these methods are feasible. However, it was not possible to complete the fabrication of the whole detector, as the process has stopped due to the time constraints of the project.

4.1. Absorption Layer

Two batches were prepared for the test of ZnO absorption layers, where three different annealing times were set: 1 minute, 2 minutes, and 10 minutes. The first batch consists of three different protocols for spinning and 10-minute annealing, where one sample is prepared for each protocol. The spin coating protocols are 1000rpm for 80s, 1500rpm for 65s, and 2000rpm for 40s. The transmission spectrum of each sample was measured by the optical test setup at three different orientations of the sample. For the response analysis, the transmission of 470nm over 350nm is calculated for each measurement and the ratios are averaged for the same angle magnitude for different sample orientations. The results are presented in figure 4.1, together with the standard deviations between the different orientations of one sample and a reference measurement without any ZnO layer.

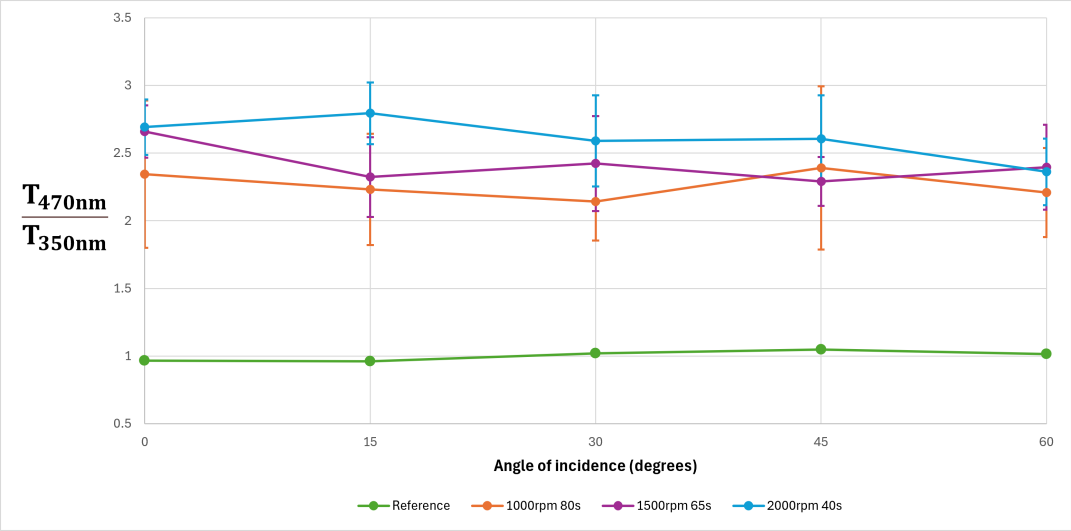

Figure 4.1: Transmission of 470nm over 350nm at different angles of incidence for 3 different samples with 10-minute anneal and different spin-coating protocols. The bars at each data point indicate the standard deviation within three different orientations of each sample.

The results show a transmission ratio within the range of 2 and 3, where the overall response with different angles is relatively the same. The highest ratio is observed for 2000rpm (2.61), followed by 1500rpm (2.42) and 1000rpm (2.26). Among these three, the lowest standard deviation is calculated for 2000rpm, where the deviation is 10% of the average result. For 1500rpm and 1000rpm, these deviations are approximately 11% and 19% respectively. This results in an overlap of the measurement points between each speed, which means that the factors obtained at different speeds are relatively the same.

After this initial test, a second batch of ZnO samples is tested with shorter annealing times (1 and 2 minutes) to investigate the effect of annealing time on the layer properties. For this batch, protocols with 1500rpm and 2000rpm are chosen to be the spinning speeds, as they have lower standard deviations and higher average transmission ratios. The measurements are then compared with the 10-minute annealing time and are presented in figures 4.2 and 4.3 for 1500rpm and 2000rpm respectively with the reference measurement.

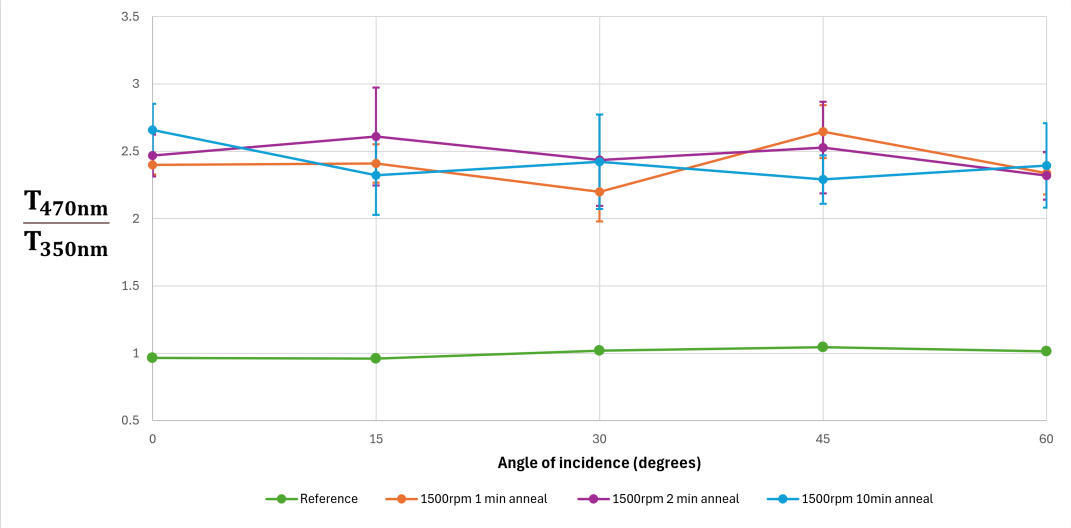

Figure 4.2: Transmission of 470nm over 350nm at different angles of incidence for three samples spun at 1500rpm with different annealing times. The bars at each data point indicate the standard deviation within three different orientations of each sample.

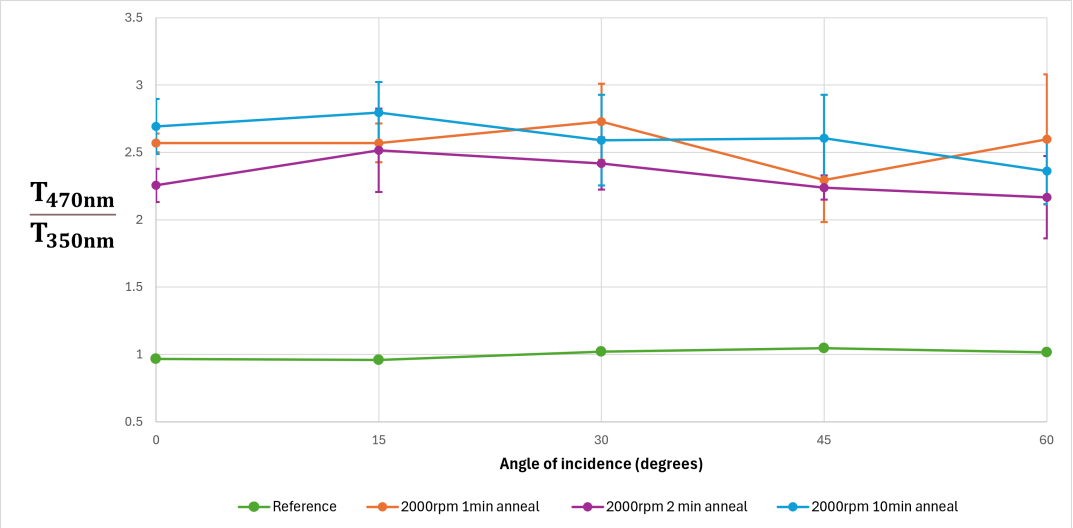

Figure 4.3: Transmission of 470nm over 350nm at different angles of incidence for three samples spun at 2000rpm with different annealing times. The bars at each data point indicate the standard deviation within three different orientations of each sample.

The results show that the transmission ratio is approximately the same for different annealing times. For both of the speeds, the ratio is within a range of 2 to 3, similar to the observation for the samples with 10-minute annealing times. The standard deviations are less than 10% for all the cases, however, there is a large overlap within the samples. All in all, the annealing time does not have a significant impact on the transmission of the ZnO nanoparticles.

The spectral response of each sample is presented in Appendix E. The response shows that for all of the samples, the transmission of all of the wavelengths is reduced with increasing angle of incidence even though the transmission ratio is kept the same.

In addition to the transmission measurements, the thicknesses of each sample are measured with the profilometer. The results are presented in table 4.1.

Sample	Average thickness (nm)
1000rpm/80s, 10-minute annealing	2250
1500rpm/65s, 1-minute annealing	898
1500rpm/65s, 2-minute annealing	427
1500rpm/65s, 10-minute annealing	1310
2000rpm/40s, 1-minute annealing	678
2000rpm/40s, 2-minute annealing	161
2000rpm/40s, 10-minute annealing	1007

Table 4.1: Thicknesses of ZnO absorption layers

These results show that, within the same annealing time, the thickness of the layer decreases with increasing speed. However, when compared with the other annealing times, 2-minute annealing has the lowest thickness compared to the rest. Overall, there is a high deviation of thickness for the same spinning speed.

4.2. Fabry-Perot Filter

The measured transmission spectra compared to the simulation at 0° angle of incidence are presented in figure 4.4 for each filter.

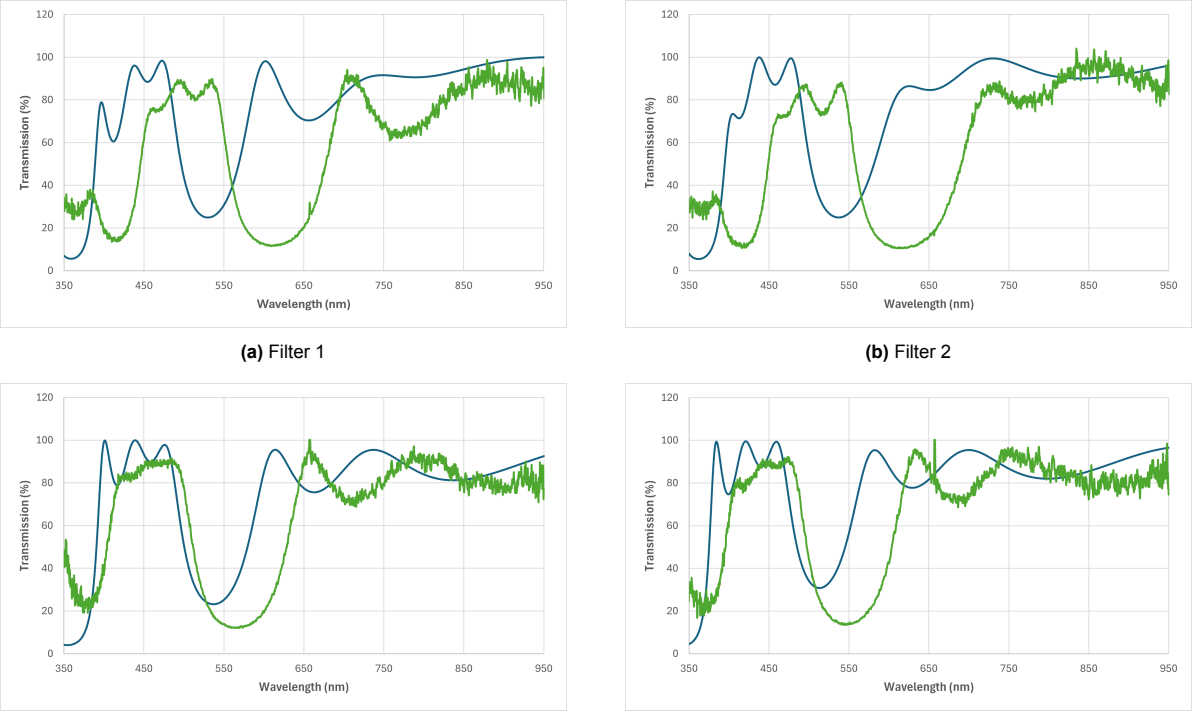

(a) Filter 1

(b) Filter 2

(c) Filter 3

(d) Filter 4

Figure 4.4: Transmission spectra of the Fabry-Perot filters. (Navy blue) The simulated transmission response and (Green) the experimental response.

The results show that for filter 1 (figure 4.4a) and filter 2 (figure 4.4b), there is a 70nm shift for the minimum transmission wavelength, which was designed to be 350nm according to the simulation. The transmission band for the range of 400-500nm is also shifted towards a higher wavelength, in which there is approximately a 30nm shift for the transmission peak within these bands. Additionally, compared to the simulations, there is a reduction in the transmission of 470nm, which has reduced approximately 20% for both of these filters.

For filters 3 (figure 4.4c) and 4 (figure 4.4d), the shift in the response towards higher wavelengths is observed less, which is 30nm and 20nm respectively. In contrast to filters 1 and 2, there is only a shift of approximately 5nm for the peak transmission within the band of 400-500nm. The transmission of 470nm is also reduced by approximately 10%.

For all the filters, the effect of different angles is also explored. To determine the cancellation performance of 350nm, that is the excitation source, the ratio between 350nm and 470nm is calculated for different angles of incidence and the results are presented in figure 4.5.

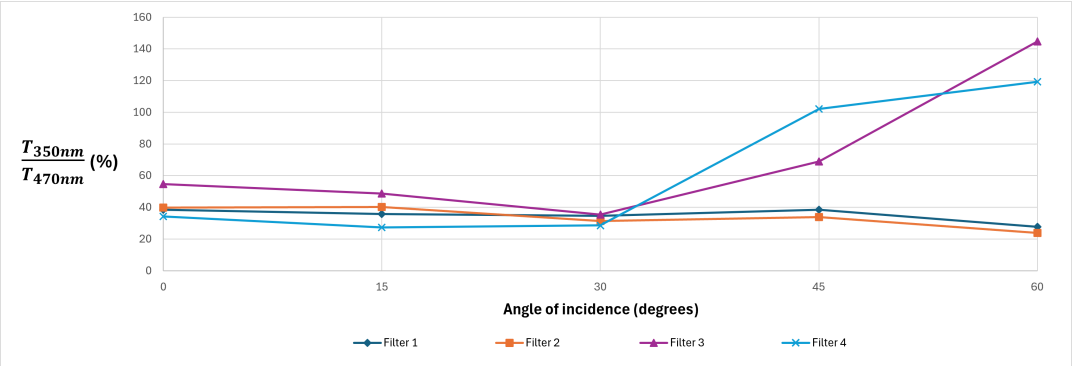

Figure 4.5: Transmission ratio of 350nm and 470nm at different angles of incidence

Here, a lower percentage indicates a better cancellation of 350nm compared to 470nm and a higher percentage shows the filter behavior is similar for 350nm and 470nm. When the percentage is higher than 100%, this means that the filter is preventing the transmission of 470nm more compared to 350nm. The transmission spectra of the filters at different angles are presented in Appendix D.

The results show that, among the four combinations, filter 4 has the lowest percentage of 350nm (34.3%) when the light perpendicularly hits the filter ($0°$ angle of incidence). The percentage then decreases to approximately 28% for $15°$ and $30°$. However, when the angle is increased more, the transmission of 350nm increases significantly and is more than 470nm (more than 100% ratio). A similar response is observed for filter 3, where the 350nm transmission increases significantly after $30°$. In this filter, a maximum 350nm percentage (54.7%) is observed for perpendicular illumination compared to other filters. Overall, both of these filters have low angle tolerance, as their response to 350nm transmission decreases significantly when the angle of incidence is more than $30°$.

In contrast to filters 3 and 4, filters 1 and 2 have a more stable response. For an angle of incidence range of $0-45°$, the ratio of 350nm with respect to 470nm is approximately 36% for both of the filters. At $60°$, this reduces further to 27.8% and 23.8% for filters 1 and 2 respectively. This means that the filters are suitable to use for cases where there are high angles of incidence and when there are variable angles of incidence.

The reciprocal of this ratio indicates the factors of 470nm related to 350nm, which is shown in figure 4.6. This can then be used to determine the cancellation response of the filter.

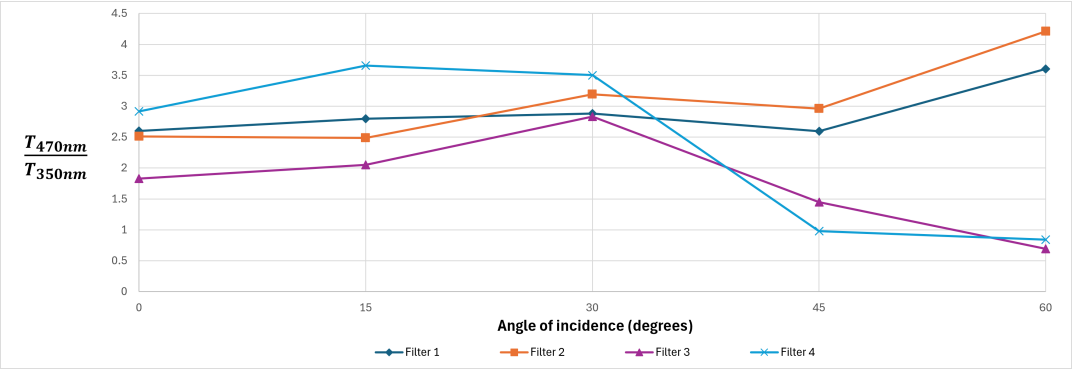

Figure 4.6: Factor of 470nm with respect to 350nm at different angles of incidence

This figure shows that 470nm is transmitted 2-3 times more compared to 350nm at 0 degrees and that changes for different angles. As shown before, filters 1 and 2 have a more stable relationship between 470nm and 350nm, and filters 3 and 4 have lower factors between 470nm and 350nm at higher angles.

4.3. Photodetector

Pre-fabrication tests were done on the etching of molybdenum and back-side etching to optimize the etching rate and the etching conditions. Due to safety concerns, 33% wt. potassium hydroxide (KOH) at approximately $80°$ is used instead of TMAH for the back-side etching. Since KOH and TMAH have similar etching profiles, this is not an issue in terms of structural tests. However, when KOH is used for back etching for an active device like the photodetector, there is a chance of charging the surface which influences the properties of the device.

For the molybdenum etching test, a 500nm Mo is deposited on a silicon wafer and a mask with square openings is exposed. For the test, H_2O_2 is poured on the wafer and then stayed for 15 minutes (figure 4.7a). Then, the wafer is dumped in a water bath and dried. The results showed that the positive photoresist, which is used for lithography, is completely etched by H_2O_2 that also etched the molybdenum layer on the wafer. Therefore, a $2\mu m$ PECVD oxide is deposited as the hard mask before the lithography process to protect the Mo under the mask. With this optimization, it was possible to protect the molybdenum. However, the etching process was non-uniform throughout the wafer, in which the sides of the wafer were etched less compared to the center. This non-uniformity is observed during

the etching, where flakes of metal are observed at the sides. This is then removed by more etching but this results in an over-etch in the middle of the wafer, which might cause issues with metal interconnect formation.

A $33\%wt.$ KOH solution is prepared with 2kg KOH salt from Sigma Aldrich and 4 liters of distilled water for the back side etching of the DSP silicon wafer, where PECVD SiO_2 ($2\mu m$) and SiN_x (300nm) are used as the hard mask on both sides of the wafer. After removing the hard mask for the back-etch region, the wafer is etched for 2 hours. The results show a $133\mu m$ etching of silicon, where the etching rate can be calculated to be $\sim 1.1\mu m/min$. Overall, the etching is observed to be uniform throughout the wafer. The experimental setup for both the Mo etching and back-side etching are shown in figure 4.7.

(a) Molybdenum wet etching test setup

(b) Back-side etching test setup

Figure 4.7: Pre-fabrication tests for photodetector

Additionally, the first step of the detector fabrication has been completed by STI etching, using Trikon Omega 201 to etch the silicon with reactive ion etching (RIE). To determine the etching rate, a test wafer is used, and the resulting etching thickness is determined using Dektak 8 profilometer. From this, the etching rate is determined to be approximately $240nm/min$. The etching time for the desired substrate thickness (700nm) is then determined to be 2 minutes 55 seconds.

The STI etching results and their deviation with respect to 700nm for four DSP wafers are shown in table 4.2.

Wafer number	STI depth (nm)	Error (%)
1	764.05	9.15
2	752.93	7.56
3	752.16	7.45
4	749.1	7.01

Table 4.2: STI etching results

After this process, the fabrication of the photodetector has been stopped in the context of this master project and will be continued later.

4.4. Combination of the different parts of the system

Based on the results from the Fabry-Perot filter and the ZnO absorption layer, the expected cancellation factor is in the range of 2-3 for both of the components. The total cancellation factor after combining these components is then the multiplication of the cancellation factors, which corresponds to a range of 4-6.

To test this performance, the pre-fabricated Fabry-Perot filters are spin-coated with ZnO nanoparticles at 2000rpm/40s, and annealed for 2 minutes at $200 \pm 3°$. During annealing, Filter 1 delaminated from the glass wafer, which is shown in figure 4.8 with its initial look. This did not occur for the rest of the samples.

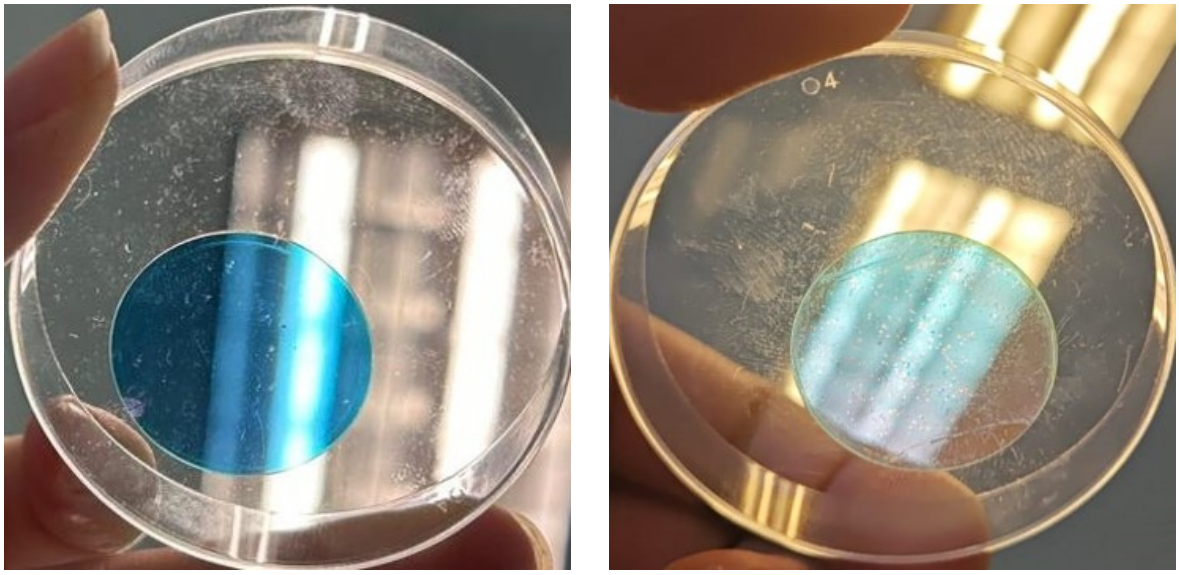

(a) Original filter 1 **(b)** Delaminated filter 1

Figure 4.8: Delamination of filter 1 after annealing

After the fabrication, the transmittance of each sample is measured for different angles at three different orientations. The average results with standard deviations are presented in figure 4.9.

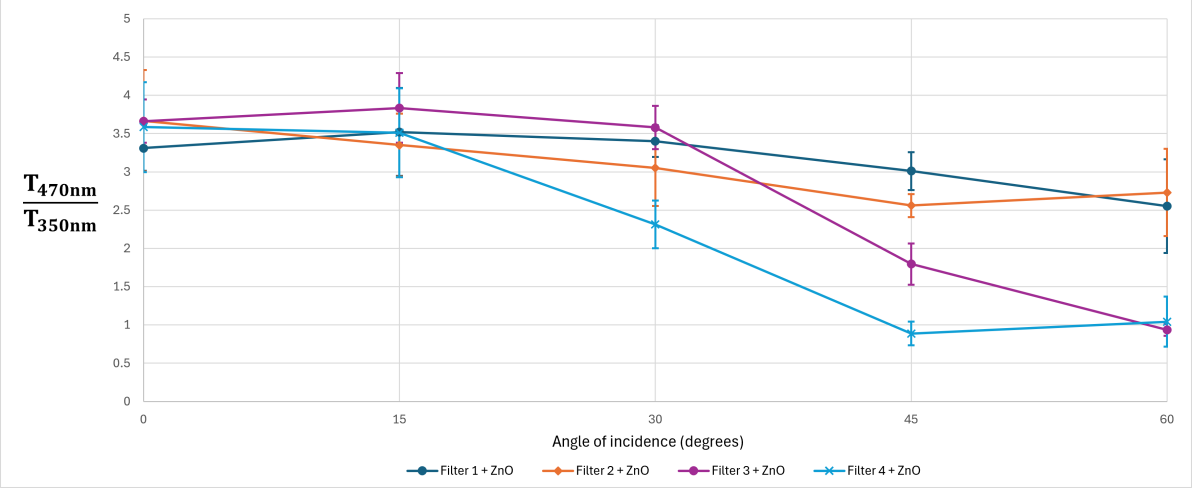

Figure 4.9: Transmission of 470nm over 350nm at different angles of incidence for the combination of the filters with the ZnO absorption layer. The bars at each data point indicate the standard deviation within three different orientations of each sample.

The results show that for $0°$ and $15°$, all of the combinations have a transmission factor in the range of 3-4, and afterward, this factor starts to decrease for all of the combinations. The most significant

decrease is observed for filter 4 with ZnO, followed by filter 3 and ZnO. They both reduce to a factor of 1 at $60°$, which means that the transmission of 470nm is the same as 350nm. For filters 1 and 2 with ZnO, the reduction in transmission ratio is less, and the minimum transmission is equal to 2.55 at $60°$ and 2.56 at $45°$ respectively. Additionally, the standard deviations overlap with each other for $0°$ and $15°$, which means that the responses of the combinations are approximately the same.

To compare the response of these combinations with the filters, the transmission ratios of the filters are plotted with these results. The plot is presented in figure 4.10 and the percent change compared to the old transmission ratio is shown in table 4.3.

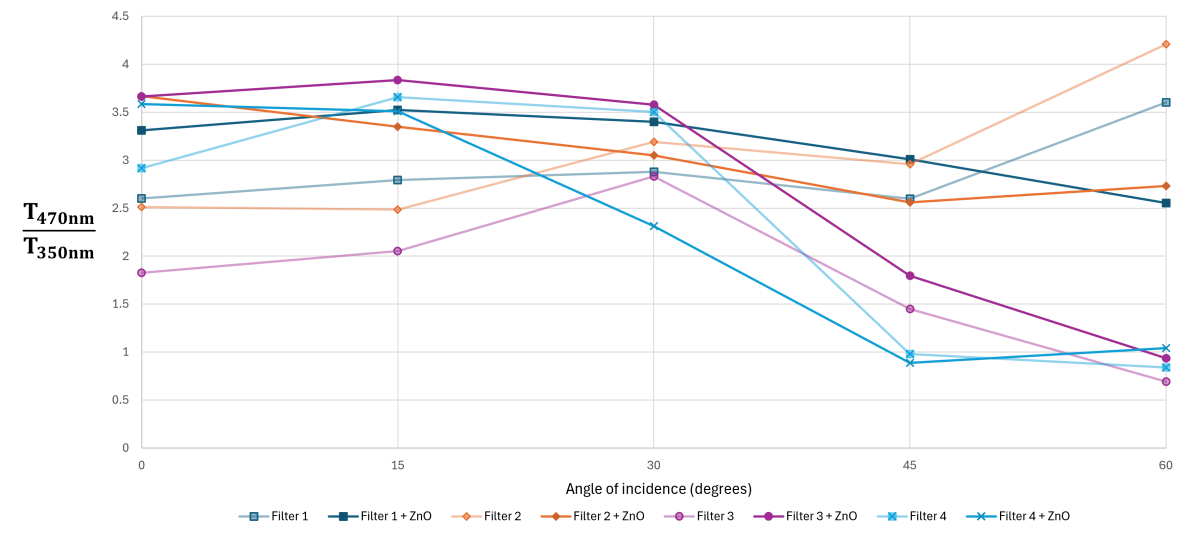

Figure 4.10: Transmission of 470nm over 350nm at different angles of incidence for the Fabry-Perot filters and the combination of the filters with the ZnO absorption layer. The Fabry-Perot filters are plotted partially transparent.

Angle (degrees)	Filter 1 percent change (%)	Filter 2 percent change (%)	Filter 3 percent change (%)	Filter 4 percent change (%)
0	27.3	45.9	100.4	22.9
15	26.0	34.7	86.9	-4.0
30	18.1	-4.4	26.5	33.9
45	15.9	13.5	23.9	-9.4
60	-29.1	-35.1	35.2	24.2

Table 4.3: Percent change of the combination of ZnO absorption layer and Fabry-Perot filter compared to Fabry-Perot filters. The negative influence of the combination is indicated in red.

The results show that all of the combinations have an improvement at $0°$, where the most improvement is observed for filter 3. For all angles, it exhibits an improvement, at least more than 23.9%. A similar improvement is observed for filter 1 but with deterioration at $60°$ (-29.1%). Another decline in performance is present for filter 2 at $60°$ (-35.1%). Lastly, filter 4 shows improvements for some angles while there is a slight decrease in performance at $15°$ and $45°$. The complete transmission spectra of each sample can be found in Appendix F.

4.5. Biodegradation time

The expected biodegradation rates of each component are calculated based on the degradation values given in the literature. These values are calculated separately for the photodetector, the 4 different configurations of the filter, and the maximum thickness that has been measured for the ZnO absorption layer. The degradation medium conditions are PBS at $37°$ (pH 7.8) for ZnO ($4nm/hour$), SiO_2 ($0.1nm/day$), SiN_x (0.794 or $1.3nm/day$) and silicon ($4.1nm/day$), and Hank's solution at $37°$ for Mo ($0.2-0.6nm/hour$) [36] [49]. For the Fabry-Perot and ZnO, as they are built on glass wafers, the degradation calculation is done by assuming that only one side of the component is exposed to the solution;

whereas for the detector it is assumed to be both sides as all its materials are biodegradable.

The calculated degradation times for each component are presented in table 4.4.

Component	Degradation time
Photodetector	$\sim$ 57 years
Filter 1	12-13 years
Filter 2	12-13 years
Filter 3	14-15 years
Filter 4	13-14 years
ZnO layer (2250nm)	23.5 days

Table 4.4: Total expected biodegradation times of each component

In addition, the degradation rate is also calculated for the case when it is combined altogether. This means that when placed in the body, the degradation will start from both sides of the device, which means the bottom of the detector and the ZnO at the uppermost layer will be exposed to the body. For the setup, it is assumed that the $2\mu m$ support at the backside is replaced by the filter and the ZnO layer. Based on this, the maximum degradation time is calculated to be $\sim$ 38 years.

5 Discussion

5.1. Test setup

The optical measurement setup for the Fabry-Perot filter and the ZnO absorption layer needs some improvements regarding its measurement range and the spectrum of the input light source. The Ocean Optics Flame spectrometer is calibrated for measurements within the range of 350nm-1000nm. This is at the edge of the spectrum for the measurement of 350nm. As a result, high fluctuations are observed at this wavelength, which might have influenced the accurate measurement of the response for 350nm.

Additionally, the DH2000 Deuterium Tungsten Halogen Lamp spectrum has low intensity of 350nm, compared to the other wavelengths. Its spectrum is shown in figure 5.1. As a result, when the transmission is normalized to 100% for all of the wavelengths, a slight change in the intensity of 350nm affects the transmission response more compared to wavelengths that are with high intensity. Eventually, this might have caused large fluctuations in the measurement.

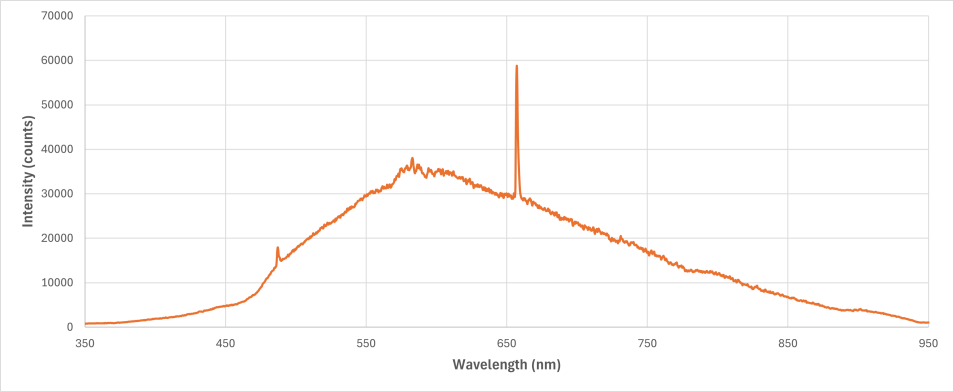

Figure 5.1: Spectrum of DH2000 Deuterium Tungsten Halogen Lamp

One way to eliminate these effects is to increase the averaging of the data per sample. It was set to 5 scans to average for these measurements, but it is recommended to increase it further to reduce the fluctuations further.

5.1.1. Future Outlook

For future experiments, it is recommended to use a spectrometer with a larger measurement range and to choose a lamp with a larger intensity of 350nm so that the measurement of 350nm can be done more accurately. An increase in scans to average can also improve the measurement as mentioned, but the improvement in the measurement setup will allow for a better result.

For this experiment, it was not possible to build the test setup for the photodetector, but for future experiments, it is suggested to use the PCB concept with a lamp with a higher intensity of 350nm.

Overall, the measurement setup was sufficient to have data that is comparable with each other but requires improvements to have more accurate results.

5.2. Absorption Layer

At the end of this project, it was possible to fabricate and test ZnO absorption layer samples with different annealing times and spinning protocols. The results show that ZnO nanoparticles can indeed be used for the cancellation of 350nm, compared to the other wavelengths. The results from the tests of different fabrication protocols and annealing times show that the spectral behavior of ZnO is not affected by different protocols. The reduction of transmission, that is observed for every sample, can be explained by an increase in the reflectivity of ZnO nanoparticles with an increase in the angle of incidence [41]. This decrease does not influence the transmission ratio of 350nm and 470nm, as the decrease in transmission is observed for all the wavelengths.

However, the measurements have high standard deviations, which results in an overlap between the responses of each protocol. This means that the measurements of each sample have essentially the same behavior and therefore a decision on the best protocol cannot be made. Even though some experimental choices are made based on the standard deviation and the magnitude of the cancellation factor, these choices are limited to the measurements from a single sample.

In addition, there is high variability within the thicknesses of the ZnO layers, even at the same spinning speeds (table 4.1). It was expected that for a higher spinning speed, the thickness would be lower; whereas for a slower speed, it would be higher. It was possible to observe this relationship for samples with the same annealing times and different speeds, but the samples with the same spinning speeds and different annealing times do not have similar thicknesses as expected. The results also indicate that this variability in thickness does not influence the optical behavior of the layer, as the transmission measurements for the same spinning speeds show similar behavior (figures 4.2 and 4.3).

Overall, the measurements of the ZnO absorption layer show that the optical performance is not dependent on the thickness and the fabrication protocol. This could be because the layer consists of nanoparticles, where the optical performance of the particle itself is of interest, but not the overall performance of the layer. As long as there are particles covering the surface, the 350nm will be absorbed and its absorption will not be thickness-dependent. Since the sizes of these particles are chosen so that they have high absorption to 350nm, the absorption at the surface of the ZnO absorption layer allows for sufficient absorption.

5.2.1. Future Outlook

For future experiments, it should still be noted that the measurement results and observations are based on the measurements from single samples. To ensure that the results are consistent and reproducible, the fabrication protocols have to be replicated for multiple samples and tested accordingly. Additionally, the surface properties of the layers have to be checked with the atomic force microscope (AFM) and scanning electron microscope (SEM) to see the distribution of the nanoparticles and the structure of the layers.

5.3. Fabry-Perot Filter

By the end of the project, it was possible to test four different configurations of the Fabry-Perot filter. The results show a higher transmission of 350nm and a lower transmission of 470nm, compared to the simulations in Filmetrics. This then results in a significant reduction in the transmission ratio of 470nm and 350nm (table 3.2 vs. figure 4.5). The reductions are 81.2%, 79.0%, 92.0%, and 84.4% for filters 1-4 respectively.

One of the reasons for this decrease in the transmission ratio is the reduction of 470nm transmission in all of the filters. The reduction in 470nm or any other wavelengths is expected compared to the simulation, as the simulation conditions assume a pure setup without any non-idealities. The spectroscopy measurements are done in the open air, where there is the presence of dust particles that could interfere

with the measurement. This means that any particle, that is present within the measurement path or on the surface of the filter, could cause reflections of light which will eventually reduce the transmission of the light. A solution to eliminate this effect could be a measurement in a dust-free environment.

Another reason for the reduction of ratio is the shift in the transmission spectrum of the filters towards higher wavelengths. Even though this is less for filters 3 and 4, it still increases the transmission of 350nm, as the local minimum that is designed to be on 350nm is shifted. This shift could be because of the fabrication limits of the ICPECVD.

The PlasmaPro 100 ICPECVD machine is designed to deposit a minimum thickness of 20nm [50]. Since the thickness of the anti-reflective filter layers is only a factor of 2 or 3 larger than the minimum resolution of the machine, the optical properties of the filter can be affected greatly due to the possibility of large fluctuations that can go up to 20nm during deposition. In addition to this, the deposition of the filter layers is done consecutively in the same chamber. During each deposition, the chamber walls also come in contact with the deposition gases that result in the accumulation of the material. When the deposition is shifted from one material to the other, the residues of the previous material that are collected in the chamber can land and interfere with the deposition of the current layer. This then results in a gradient between the interfaces of the layers, which might influence the optical behavior. Consequently, both due to the minimum deposition thickness specification of the ICPECVD and due to residues of the chamber, the shift in the spectrum might have occurred, which might have also influenced the transmission of other wavelengths.

Besides the resolution of ICPECVD, the fabrication accuracy was also limited by the measurement of the thicknesses of each filter layer. As multiple layers of SiO_2 and SiN_x are being deposited at the same time and since each layer is transparent, the measurement of the film thicknesses was not possible to measure with the ellipsometer. Therefore, the exact thickness of the filter layers is unknown even though the deposition rate is calculated beforehand. This prevents the complete characterization of the device dimensions, which can only be estimated through the behavior observed by the optical measurement as a shift in the spectrum. A solution to fix this issue could be the deposition of each layer one by one, which will increase the fabrication time greatly, or by the inspection of the cross-section of the filter with SEM after the fabrication is completed.

5.3.1. Design considerations

During fabrication, filters 1 and 2 are fabricated and tested before filters 3 and 4. Therefore, optimizing the design of 3 and 4 is done based on the results of filters 1 and 2. As a shift of 30nm at the transmission peak was observed for filters 1 and 2, the spacer layer of the other filters is decreased by 5nm. Additionally, to compensate for the shift of 70nm at the minimum transmission wavelength towards higher wavelengths, the anti-reflective layers of filter 4 are reduced by 10% ($\sim 4 - 6nm$). In the end, for filters 3 and 4, the shift in peak transmission was reduced to 5nm, and the shift in minimum transmission was reduced by 10nm in filter 4, compared to filter 3. This means that it is possible to optimize the design of the filter based on the shifts in the transmission spectrum.

5.3.2. Future Outlook

This experiment consists of a total of 4 samples with no replica of the same sample. Therefore, the measurements are limited to the behavior of a single filter. For future experiments, it is recommended to fabricate more filters with the same configuration so that the variability within the chamber and the samples can be understood. Additionally, it is recommended to fabricate the same filter at different times to understand the reproducibility of the result. To be able to match the desired simulation behavior completely, the thickness of the anti-reflective and the spacer layer should also be varied further, where different variations can be tested to settle on the best thickness. Lastly, an experimental setup can be created to model the medium inside the body to analyze the optical behavior of the filter. This will allow for the understanding of the optical restrictions to consider when the body is involved so that the filter design can be adjusted accordingly.

5.4. Photodetector

The pre-fabrication tests of the photodetector show that back-etching stability is preserved when the wafer is etched approximately halfway through. It should be noted that during the etching, the KOH

concentration increases with water evaporation as the solution is heated. To minimize this effect and ensure that the evaporated water returns to the solution, the top of the KOH bath is closed.

Additionally, the STI etching results have less than 10% deviation compared to the desired depth. This deviation is within the acceptable range and the expected result from this is a further reduction in 400nm current, as was observed with the simulation with an increase in substrate thickness. There is also a possibility of a minor reduction of 470nm, but since the absorption of 470nm is still within the depletion region, it is not expected to influence the measurement results.

The choice of low-resistive wafers is essential to have a doping of approximately $10^{16} atoms/cm^3$, as when the substrate doping concentration is decreased, the intrinsic depletion width increases significantly more than the desired depletion width of 580nm. This then prevents the controlling of the depletion width.

5.4.1. Future Outlook

For future work, as the wet-etching of molybdenum resulted in nonuniform etching, it is suggested to proceed with dry etching. This will allow for a more uniform etching of the metal without undercuts due to anisotropic etching of the metal. It should be noted that the mask was created so that it has tolerance to these undercuts, but switching to dry etching will improve the interconnect layer quality.

Moreover, it is recommended to conduct the back-etching tests with TMAH, to be able to quantify the etching properties before the fabrication of the actual photodetector. The etching tests should also be conducted until the desired substrate thickness, where the stability of the wafer under vacuum or in other machines has to be checked.

The photodetector fabrication must be completed on double-side polished low-resistivity wafers to achieve optimal electrical performance in line with calculations and simulations. Additionally, post-ion implantation doping concentrations should be verified using TLM test structures to confirm they align with simulated conditions.

As the fabrication process has not been completed due to time constraints, it is not possible to assess the device's performance at the current stage of the project.

5.5. Combination of the different parts of the system

5.5.1. Fabry Perot filter and ZnO absorption layer

During the spin coating of ZnO on filter 1, the layers of the filter delaminated from the surface of the glass wafer. This might be due to the organic residues or particles on the glass wafer before the deposition of the filter. The wafer was only cleaned with a nitrogen gun to get rid of any dust particles, but any remaining residues on the wafer could have stayed there during deposition. Then, when the wafer is heated during annealing, these residues might have expanded or created stress on the surface that could result in delamination from the wafer. This effect was not observed for other combinations and when compared with the behavior of other combinations, the results seem to be not significantly affected.

The results from the absorption layer and filter combination show that there is an improvement in the filter behaviors, especially for the angle range of $0 - 30°$. The expected improvement is less than the expected range of 4-6. This could be due to the variability that was observed for the ZnO layer.

In addition, for some of the combinations, a degradation of performance is observed with an increase in angle, when compared to the initial filter behavior. This could be attributed to the increase in reflectivity of ZnO with an increase in the angle of incidence, which might have resulted in worse behavior in terms of intensity.

From these measurements, filter 3 with ZnO shows the most amount of improvement compared to the rest. It has the best performance for the angle range of $0 - 30°$, where the factor of transmission then starts to decrease. This behavior makes this filter suitable for a design where the excitation source has a low angle of incidence on the filter. This could be done by choosing the distance between the excitation source and the filter, and the distance between the filter and the tissue so that the angle of incidence is less than $30°$ within the illumination of any location on the filter. For designs, where the

angle of incidence can go up to $60°$, filter 1 is more favored compared to the rest, as it has a stable angular performance with a higher transmission factor.

Overall, the choice of which combination is suitable is based on the positioning of the excitation source and the tissue distance.

5.5.2. All

The combination of all components has to be done after the fabrication of the photodetector, where the filter has to be deposited with ICPECVD and ZnO has to be drop-casted. The test for this combination can only be done with current measurements as the back side of the photodetector is opaque.

Based on the simulation results of the photodetector and the measurements of the filter-ZnO combinations, the expected transmission factor can be calculated. The minimum transmission factor of the detector is simulated to be 3.95 and the maximum is 12.5. As the combination of the filter and the ZnO layer has a transmission factor range of 2.5-4 at $0°$, the total cancellation factor can be expected to be in the range of 10.0-50.0, where it is assumed that the photodetector works the same as the simulation. The actual experimental result might be lower than this range.

5.5.3. Future Outlook

For the rest of the experiments, it is recommended to clean the surface of the glass wafer with 5-minute acetone, 5-minute IPA, and 5-minute distilled water baths before filter deposition, similar to the cleaning for the absorption layer. The fabrication of filter 1 and ZnO layer combination is recommended to be repeated to ensure the results are not affected by the delamination.

Additionally, as these measurements are conducted based on a single sample for each combination, it is recommended to fabricate and test more samples for repeatability and consistency of the measurements.

5.6. Biodegradation time

The materials of the design were chosen so that the filter and the optical detector are possible to degrade in the body and that they are bioresorbable. Even though this is theoretically the case for each material choice, the total biodegradation time results in the device being classified as long-term/permanent based on International Standard ISO10993-1 [51]. Among the materials that are chosen, SiO_2 has the slowest degradation rate, which increases the degradation time of the device. It is possible to accelerate the degradation rate of SiO_2 by increasing the pH of the medium around the device [49]. For example, by increasing the pH of PBS to 10, the degradation rate of silicon, SiO_2 and SiN_x can be increased to $624nm/day$, $0.6nm/day$, and $7nm/day$ respectively [49] [52]. This then reduces the total degradation time to $\sim$ 6.5 years. It is also possible to reduce this further by replacing the support of the photodetector at the metallization side with SiN_x, which reduces the degradation time to $\sim$ 2 years.

It should also be noted that this calculation assumes a degradation only from the top and the bottom and that each material exists as a full layer, instead of a structure. In the real case, it is expected to degrade faster since the degradation will also be from the sides and around each structure.

5.6.1. Future Outlook

For future experiments, it is recommended to test the possibility of a support layer that is different from SiO_2 and the effect of the pH. The possibilities to change the pH and the ways to prevent any harm to the body have to be investigated in more detail, as the placement of a sensor with a higher pH can cause complications near some of the organs, such as the heart, and the open wounds. One solution could be a casing around the device that has a similar degradation time as the degradation of the device at a higher pH. This might prevent the high pH medium from interfering with its surroundings.

Another possibility is to investigate the addition of holes or dents in the material to accelerate the degradation, as it will allow the penetration of the surrounding medium to interfere with the device and initiate the biodegradation process.

Additionally, it is recommended to create a test setup with accelerated biodegradation tests in PBS at $37°$ to know the exact degradation rates of the materials used for this design, as the material properties

may vary within the machines that are used for fabrication. This setup could be created by the formation of a thin layer of any pre-selected material on a glass wafer, and then the measurement of its thickness loss within a pre-determined time.

In summary, the experiments for the filters, ZnO absorption layer, and the combination of the two have to be replicated to be able to have a consensus on the optimal filter and ZnO fabrication protocol choice. The choice is also affected by the positioning of the device with respect to the excitation source and the tissue. The repetition of the experiment will also show the reproducibility and consistency of the design.

Furthermore, the choice of materials for the fabrication of the photodetector support layers has to be reconsidered with the possibilities of acceleration of the degradation to be able to shorten the degradation time. Overall, the fabrication of the photodetector is needed to know its performance compared to the simulation and its biodegradation time.

6

Conclusions

The goal of this project was to design a bioresorbable optical filter and photodetector to determine tissue oxygen levels for the assessment of tissue vitality through NADH fluorescence measurements. The design of the system was done so that the transmission of the emission peak of NADH (470nm) is the highest compared to the rest of the wavelengths and lowest to the excitation wavelength (350nm). The design consisted of a ZnO absorption layer, a Fabry-Perot filter, and a wavelength-specific gate-controlled photodetector, where the optimization of the properties was done through calculations and simulations.

At the end of the project, it was possible to build and test different Fabry-Perot filters and ZnO absorption layers separately and combined. The results show variability within samples and are based on single samples. Therefore, repetition of the experiment is required to have a conclusion on the optimal choice of design. In addition, the results regarding the photodetector are based on pre-fabrication tests and simulations, as it was not fabricated during the project. However, it is possible to estimate the overall device performance based on the simulation results and the measurements of the Fabry-Perot filter and ZnO absorption layer combinations. These results show that the optical filter and the photodetector design can achieve a cancellation of more than an order of magnitude, which is a minimum cancellation by a factor of 10 for 350nm.

Additionally, the biodegradation calculation of the design is higher than the requirements, but by investigating acceleration methods and the replacement of some parts of the device, it is possible to shorten this period.

In conclusion, with this design for the optical filter and photodetector, it is possible to isolate the peak emission wavelength of NADH and cancel its excitation wavelength by an order of magnitude to be able to quantify oxygen concentration through fluorescence measurements for tissue vitality analysis.

References

[1] P.J. French, J. Jeekel, and J. Lange. *WO2007008057A1 - Tissue vitality monitoring system and method and surgical technique - Google Patents*. 2007. URL: https://patents.google.com/patent/WO2007008057A1/en.

[2] S. Guo and L.A. DiPietro. "Factors Affecting Wound Healing". In: *Journal of Dental Research* 89.3 (Mar. 2010), pp. 219–229. ISSN: 0022-0345. DOI: 10.1177/0022034509359125. URL: https://pubmed.ncbi.nlm.nih.gov/20139336/.

[3] Avraham Mayevsky et al. "Tissue spectroscope: a novel in vivo approach to real time monitoring of tissue vitality". In: *Journal of biomedical optics* 9.5 (2004), p. 1028. ISSN: 1083-3668. DOI: 10.1117/1.1780543. URL: https://pubmed.ncbi.nlm.nih.gov/15447025/.

[4] Roland N. Pittman. "Regulation of Tissue Oxygenation". In: San Rafael (CA): Morgan & Claypool Life Sciences, 2011. Chap. 4. URL: https://www.ncbi.nlm.nih.gov/books/NBK54104/.

[5] Harald Pötzschke and Kai-Uwe Zirk. "Monitoring of Surgical Wounds with Purely Textile, Measuring Wound Pads – I. The Concept, and Technical Wound Models for Wound Pad Testing with Performance". In: *The Open Biomedical Engineering Journal* 16.1 (Apr. 2022). ISSN: 1874-1207. DOI: 10.2174/18741207-V16-E2202170.

[6] Miguel F. Montero-Baker et al. "The First-in-Man "si Se Puede" Study for the use of micro-oxygen sensors (MOXYs) to determine dynamic relative oxygen indices in the feet of patients with limb-threatening ischemia during endovascular therapy". In: *Journal of Vascular Surgery* 61.6 (June 2015), pp. 1501–1510. ISSN: 10976809. DOI: 10.1016/J.JVS.2014.12.060.

[7] Yasser Khan et al. "A flexible organic reflectance oximeter array". In: *Proceedings of the National Academy of Sciences of the United States of America* 115.47 (Nov. 2018), E11015–E11024. ISSN: 10916490. DOI: 10.1073/pnas.1813053115. URL: https://www.pnas.org/doi/abs/10.1073/pnas.1813053115.

[8] Ching Chou Wu et al. "Fabrication of miniature Clark oxygen sensor integrated with microstructure". In: *Sensors and Actuators B: Chemical* 110.2 (Oct. 2005), pp. 342–349. ISSN: 0925-4005. DOI: 10.1016/J.SNB.2005.02.014.

[9] Didi She and Mark G. Allen. "A Self-Powered, Biodegradable Dissolved Oxygen Microsensor". In: *Journal of Microelectromechanical Systems* 29.5 (Oct. 2020), pp. 1074–1078. ISSN: 19410158. DOI: 10.1109/JMEMS.2020.3013208.

[10] Soner Sonmezoglu et al. "Monitoring deep-tissue oxygenation with a millimeter-scale ultrasonic implant." In: *Nature Biotechnology* 39.7 (Mar. 2021), pp. 855–864. ISSN: 1087-0156. DOI: 10.1038/S41587-021-00866-Y. URL: https://europepmc.org/article/med/33782610.

[11] Avraham Mayevsky et al. "Mitochondrial function and tissue vitality: bench-to-bedside real-time optical monitoring system". In: *Journal of biomedical optics* 16.6 (2011), p. 067004. ISSN: 1560-2281. DOI: 10.1117/1.3585674. URL: https://pubmed.ncbi.nlm.nih.gov/21721825/.

[12] T. Y. Abay and P. A. Kyriacou. "Photoplethysmography for blood volumes and oxygenation changes during intermittent vascular occlusions". In: *Journal of Clinical Monitoring and Computing* 32.3 (June 2018), pp. 447–455. ISSN: 15732614. DOI: 10.1007/S10877-017-0030-2/FIGURES/5. URL: https://link.springer.com/article/10.1007/s10877-017-0030-2.

[13] Yihan Liu et al. "Skin-Interfaced Deep-Tissue Sensing Patch via Microneedle Waveguides". In: *Advanced Materials Technologies* 7.9 (Sept. 2022), p. 2200468. ISSN: 2365-709X. DOI: 10.1002/ADMT.202200468. URL: https://onlinelibrary.wiley.com/doi/full/10.1002/admt.202200468.

[14] Hexia Guo et al. “Wireless implantable optical probe for continuous monitoring of oxygen saturation in flaps and organ grafts”. In: *Nature Communications 2022 13:1* 13.1 (May 2022), pp. 1–12. ISSN: 2041-1723. DOI: 10.1038/s41467-022-30594-z. URL: https://www.nature.com/articles/s41467-022-30594-z.

[15] Mark E. Gray et al. “In vivo validation of a miniaturized electrochemical oxygen sensor for measuring intestinal oxygen tension”. In: *American journal of physiology. Gastrointestinal and liver physiology* 317.2 (Aug. 2019), G242–G252. ISSN: 1522-1547. DOI: 10.1152/AJPGI.00050.2019. URL: https://pubmed.ncbi.nlm.nih.gov/31188641/.

[16] Junfei Xia and Sameer Sonkusale. “Flexible thread-based electrochemical sensors for oxygen monitoring”. In: *Analyst* 146.9 (May 2021), pp. 2983–2990. ISSN: 13645528. DOI: 10.1039/D0AN02400G. URL: https://www.researchgate.net/publication/349920623_Flexible_thread-based_electrochemical_sensor_for_oxygen_monitoring.

[17] Jiameng Li et al. “Fully printed and self-compensated bioresorbable electrochemical devices based on galvanic coupling for continuous glucose monitoring”. In: *Science Advances* 9.29 (July 2023). ISSN: 23752548. DOI: 10.1126/SCIADV.ADI3839/SUPPL{_}FILE/SCIADV.ADI3839{_}SM.PDF. URL: https://www.science.org/doi/10.1126/sciadv.adi3839.

[18] *Fluorescence, Phosphorescence and Photoluminescence Differences*. URL: https://www.edinst.com/blog/photoluminescence-differences/.

[19] Chao Zhou et al. “Highly Stable and Luminescent Oxygen Nanosensor Based on Ruthenium-Containing Metallopolymer for Real-Time Imaging of Intracellular Oxygenation”. In: *ACS Sensors* 4.4 (Apr. 2019), pp. 984–991. ISSN: 23793694. DOI: 10.1021/ACSSENSORS.9B00131. URL: https://www.researchgate.net/publication/331693622_Highly_Stable_and_Luminescent_Oxygen_Nanosensor_Based_on_Ruthenium-Containing_Metallopolymer_for_Real-Time_Imaging_of_Intracellular_Oxygenation.

[20] Chang Jin Lim and Jin Woo Park. “Wearable transcutaneous oxygen sensor for health monitoring”. In: *Sensors and Actuators A: Physical* 298 (Oct. 2019), p. 111607. ISSN: 0924-4247. DOI: 10.1016/J.SNA.2019.111607.

[21] Natalie A. Wisniewski et al. “Tissue-Integrating Oxygen Sensors: Continuous Tracking of Tissue Hypoxia”. In: *Advances in Experimental Medicine and Biology* 977 (2017), pp. 377–383. ISSN: 2214-8019. DOI: 10.1007/978-3-319-55231-6{_}49. URL: https://link.springer.com/chapter/10.1007/978-3-319-55231-6_49.

[22] Jennifer S. Chien et al. “Injectable Phosphorescence-based Oxygen Biosensors Identify Post Ischemic Reactive Hyperoxia”. In: *Scientific reports* 7.1 (Dec. 2017). ISSN: 2045-2322. DOI: 10.1038/S41598-017-08490-0. URL: https://pubmed.ncbi.nlm.nih.gov/28811566/.

[23] Daniel B Cybyk et al. “Biodegradable oxygen biosensors via electrospinning”. In: *Medical Devices & Sensors* 4.1 (Feb. 2021), e10149. ISSN: 2573-802X. DOI: 10.1002/MDS3.10149. URL: https://onlinelibrary.wiley.com/doi/full/10.1002/mds3.10149.

[24] Taylor M. Cannon et al. “Characterization of NADH fluorescence properties under one-photon excitation with respect to temperature, pH, and binding to lactate dehydrogenase”. In: *OSA Continuum* 4.5 (May 2021), p. 1610. ISSN: 25787519. DOI: 10.1364/OSAC.423082.

[25] Patrick M. Schaefer et al. “NADH Autofluorescence—A Marker on its Way to Boost Bioenergetic Research”. In: *Cytometry Part A* 95.1 (Jan. 2019), pp. 34–46. ISSN: 15524930. DOI: 10.1002/CYTO.A.23597.

[26] Robert H.H. Van Den Heuvel, Marco W. Fraaije, and Willem J.H. Van Berkel. “Redox Properties of Vanillyl-Alcohol Oxidase”. In: *Methods in Enzymology* 353 (Jan. 2002), pp. 177–186. ISSN: 0076-6879. DOI: 10.1016/S0076-6879(02)53047-0.

[27] *Interference Filters & Special Filters - SCHOTT GLAS - PDF Catalogs | Technical Documentation | Brochure*. URL: https://pdf.directindustry.com/pdf/schott-glas/interference-filters-special-filters/22716-368532.html.

[28] Pimenta S et al. “High-selectivity neural probe based on a Fabry-Perot optical filter and a CMOS silicon photodiodes array at visible wavelengths”. In: *Journal of biomedical optics* 23.10 (Oct. 2018), p. 1. ISSN: 1560-2281. DOI: 10.1117/1.JBO.23.10.105004. URL: https://pubmed.ncbi.nlm.nih.gov/30350488/.

[29] V. Kalyani and Varsha Sharma. “Different types of Optical Filters and their Realistic Application”. In: (2016).

[30] E G Goh, X Xu, and P G Mccormick. “Effect of particle size on the UV absorbance of zinc oxide nanoparticles”. In: (2014). DOI: 10.1016/j.scriptamat.2014.01.033. URL: https://www.sciencedirect.com/science/article/pii/S1359646214000372.

[31] Yong Joon Choi et al. “Demonstrating a Filter-Free Wavelength Sensor with Double-Well Structure and Its Application”. In: *Biosensors 2022, Vol. 12, Page 1033* 12.11 (Nov. 2022), p. 1033. ISSN: 2079-6374. DOI: 10.3390/BIOS12111033. URL: https://www.mdpi.com/2079-6374/12/11/1033/htm.

[32] Martin A. Green. “Self-consistent optical parameters of intrinsic silicon at 300 K including temperature coefficients”. In: *Solar Energy Materials and Solar Cells* 92.11 (Nov. 2008), pp. 1305–1310. ISSN: 0927-0248. DOI: 10.1016/j.solmat.2008.06.009.

[33] Yong Joon Choi et al. “Multi-wavelength fluorescence detection of submicromolar concentrations using a filter-free fluorescence sensor”. In: *Sensors and Actuators, B: Chemical* 256 (Mar. 2018), pp. 38–47. ISSN: 09254005. DOI: 10.1016/J.SNB.2017.09.077. URL: https://www.researchgate.net/publication/320405657_Multi-wavelength_fluorescence_detection_of_submicromolar_concentrations_using_a_filter-free_fluorescence_sensor.

[34] Gi Doo Cha et al. “Bioresorbable Electronic Implants: History, Materials, Fabrication, Devices, and Clinical Applications”. In: *Advanced healthcare materials* 8.11 (June 2019). ISSN: 2192-2659. DOI: 10.1002/ADHM.201801660. URL: https://pubmed.ncbi.nlm.nih.gov/30957984/.

[35] Walid Al-Zyoud et al. “Biocompatibility Testing for Implants: A Novel Tool for Selection and Characterization”. In: *Materials* 16.21 (Nov. 2023). ISSN: 19961944. DOI: 10.3390/MA16216881. URL: https://www.ncbi.nlm.nih.gov/pmc/articles/PMC10647244/.

[36] Chen Hu et al. “Recent Development of Implantable Chemical Sensors Utilizing Flexible and Biodegradable Materials for Biomedical Applications”. In: *ACS Nano* 18.5 (Feb. 2024), pp. 3969–3995. ISSN: 1936086X. DOI: 10.1021/ACSNANO.3C11832. URL: https://www.researchgate.net/publication/377699769_Recent_Development_of_Implantable_Chemical_Sensors_Utilizing_Flexible_and_Biodegradable_Materials_for_Biomedical_Applications.

[37] L. A. Avinash Chunduri et al. “Streptavidin conjugated ZnO nanoparticles for early detection of HIV infection”. In: *Advanced Materials Letters* 8.4 (Apr. 2017), pp. 472–480. DOI: 10.5185/AMLETT.2017.6579.

[38] *Zinc Oxide (ZnO) Nanopowder/Nanoparticles Water Dispersion*. URL: https://nanografi.com/nanoparticles/single-metal-oxide-nanoparticles/zinc-oxide-nanoparticles/zinc-oxide-zno-nanopowder-nanoparticles-water-dispersion-size-25-35-nm-22-wt/.

[39] Burak Kadem, Hikmat Adnan Banimuslem, and Aseel Hassan. “Modification of morphological and optical properties of ZnO thin film”. In: *Karbala International Journal of Modern Science* 3.2 (June 2017), pp. 103–110. ISSN: 24056103. DOI: 10.1016/J.KIJOMS.2017.04.003. URL: https://www.researchgate.net/publication/317064006_Modification_of_morphological_and_optical_properties_of_ZnO_thin_film.

[40] Mursal et al. “Structural and Optical Properties of Zinc Oxide (ZnO) based Thin Films Deposited by Sol-Gel Spin Coating Method”. In: *Journal of Physics: Conference Series* 1116.3 (Dec. 2018), p. 032020. ISSN: 1742-6596. DOI: 10.1088/1742-6596/1116/3/032020. URL: https://iopscience.iop.org/article/10.1088/1742-6596/1116/3/032020.

[41] Mikhail N. Polyanskiy. “Refractiveindex.info database of optical constants”. In: *Scientific Data* 11.1 (Dec. 2024). ISSN: 20524463. DOI: 10.1038/S41597-023-02898-2.

[42] *Spectral Thin Film Reflectance Calculator for Thin-Film Stacks*. URL: https://www.filmetrics.com/reflectance-calculator?wmin=300&wmax=1100&wstep=1&angle=0&pol=mixed&units=nm&mat[]=Air&d[]=0&mat[]=Si3N4&d[]=87.5&mat[]=SiO2&d[]=0&sptype=t.

[43] *PlasmaPro 100 PECVD - Oxford Instruments*. URL: https://plasma.oxinst.com/products/pecvd/plasmapro-100-pecvd.

[44] Donald A. Neamen. *Semiconductor Physics and Devices*. 4th ed. New York: McGraw-Hill, 2012.

[45] *Dietary Supplement Fact Sheets*. URL: https://ods.od.nih.gov/factsheets/list-all/.

[46] Johanna Zikulnig et al. “Evaluation of the Sheet Resistance of Inkjet-Printed Ag-Layers on Flexible, Uncoated Paper Substrates Using Van-der-Pauw’s Method”. In: *Sensors 2020, Vol. 20, Page 2398* 20.8 (Apr. 2020), p. 2398. ISSN: 1424-8220. DOI: 10.3390/S20082398. URL: https://www.mdpi.com/1424-8220/20/8/2398.

[47] Maciej Serda et al. “Synteza i aktywność biologiczna nowych analogów tiosemikarbazonowych chelatorów żelaza”. In: *Uniwersytet śląski* 7.1 (2013). Ed. by G. Balint et al., pp. 343–354. ISSN: 1868-7075. DOI: 10.2/JQUERY.MIN.JS. URL: https://www.researchgate.net/publication/269107473_What_is_governance/link/548173090cf22525dcb.

[48] S. Santosh Kumar and Ravindra Mukhiya. “CMOS Compatible Wet Bulk Micromachining for MEMS Applications”. In: *Micromachining* (Nov. 2019). DOI: 10.5772/INTECHOPEN.88487.

[49] Seung Kyun Kang et al. “Dissolution Behaviors and Applications of Silicon Oxides and Nitrides in Transient Electronics”. In: *Advanced Functional Materials* 24.28 (July 2014), pp. 4427–4434. ISSN: 1616-3028. DOI: 10.1002/ADFM.201304293. URL: https://onlinelibrary.wiley.com/doi/full/10.1002/adfm.201304293.

[50] *Oxford PlasmaPro 100 PECVD*. URL: https://mnfc.princeton.edu/static/docs/Oxford%20ICP-CVD%20SOP.pdf.

[51] *Use of International Standard ISO 10993-1, ”Biological evaluation of medical devices - Part 1: Evaluation and testing within a risk management process”* | *FDA*. URL: https://www.fda.gov/regulatory-information/search-fda-guidance-documents/use-international-standard-iso-10993-1-biological-evaluation-medical-devices-part-1-evaluation-and.

[52] Seung Kyun Kang et al. “Dissolution chemistry and biocompatibility of silicon- and germanium-based semiconductors for transient electronics”. In: *ACS applied materials & interfaces* 7.17 (May 2015), pp. 9297–9305. ISSN: 1944-8252. DOI: 10.1021/ACSAMI.5B02526. URL: https://pubmed.ncbi.nlm.nih.gov/25867894/.

A

Matlab Code for Detector Characterization

The Matlab code is used to determine the intrinsic bias voltage, reverse bias voltage, and illumination current in relation to the wavelength range of 250-1450nm. The values of the constants and the equations are obtained from Neamen, D. (2012) [44] and the absorption coefficients for the wavelength range of 250-1450nm are obtained from Green et. al[32].

```
%% CHARACTERIZATION OF THE PHOTODETECTOR
%% Constants
q=1.6*10^(-19); %elementary charge (C)
e=2.718281828459045;  %Euler's number
h= 6.62*10^(-34); %Planck's constant (Js)
c= 3*10^(8); %speed of light in free space (m/s)
k= 1.38e-23; %Boltzmann constant (J/K)
n_i= 1.5e10; % silicon intrinsic carrier concentration at 300K (cm-3)
n_i_m= n_i*1e6; % silicon intrinsic carrier concentration at 300K (m-3)
eps_r= 11.7; %relative permittivity of silicon
eps_0= 8.85*10^(-12); %vacuum permittivity (F/m)
eps_oxr= 3.9; %relative permittivity of silicon oxide (SiO2)
phi_m=4.6;  %Molybdenum metal work function (V)
E_g=1.12; %Bandgap energy of silicon (eV)
elect_aff_si=4.01; %Electron affinity of silicon (eV)

%% Design parameters
T=300; %Temperature (K)
t_ox=20e-9;%thickness of the gate oxide (m)
N_a= 1e16;  %p substrate doping (atoms/cm3)
N_a_m= N_a*1e6; %p substrate doping (atoms/m3)
N_d = 3e20; %n-well doping with phosphorus (atoms/cm3)
N_d_m= N_d*1e6;%n-well doping with phosphorus (atoms/m3)
S= 200*200*10^(-12); %sensing area (m2)

%% Intrinsic Bias Voltage Determination
phi_fp=(k*T/q)*log(N_a_m/n_i_m); %Potential difference between E_Fi and E_f in p-type
    semiconductors (V)
x_dt=sqrt((4*eps_0*eps_r*phi_fp)/(q*N_a_m)); %maximum space charge width (m)
Q_SD_MAX= q*N_a_m*x_dt; %maximum space charge density per unit area (C/m2)
phi_ms= phi_m -(elect_aff_si +(E_g/2) + phi_fp); %Metal-semiconductor work function
    difference (V)
V_tn= Q_SD_MAX*(t_ox/eps_oxr) + phi_ms + 2*phi_fp; %Threshold voltage (V)
V_bi= (k*T/q)*log((N_a_m*N_d_m)/(n_i_m)^2); %intrinsic bias voltage (V)

%% Reverse bias voltage determination
x_n= sqrt(((2*eps_r*eps_0.*V_bi)./(q))*(N_a_m/N_d_m)*(1/(N_a_m+N_d_m))); %n-side depletion
    width (m)
W_pn= sqrt(((2*eps_r*eps_0.*V_bi)./(q))*((N_a_m+N_d_m)/(N_a_m*N_d_m))); % total depletion
    width with no applied voltage (m)
x_p= W_pn-x_n; %p-side depletion width (m)
```

```
W_pnr= 0.58e-6; % desired depletion width in the presence of reverse bias (m)
V_r= (W_pnr^2 - W_pn^2)*(q/(2*eps_r*eps_0))* (N_a_m*N_d_m/(N_a_m+N_d_m)); %reverse bias voltage needed for 580nm (V)
W_pn_biased=sqrt(((2*eps_r*eps_0.*(V_bi+V_r))./(q))*((N_a_m+N_d_m)/(N_a_m*N_d_m))); %reversed biased depletion width (m)
x_n_biased= sqrt(((2*eps_r*eps_0.*(V_bi+V_r))./(q))*(N_a_m/N_d_m)*(1/(N_a_m+N_d_m))); %reversed biased depletion width (n-side) (m)
x_p_biased= W_pn_biased-x_n_biased; %reversed biased depletion width (p-side) (m)

%% Illumination current determination
lambda= unnamed1(:,1);  %wavelengths of interest (250-1450nm)
abs= unnamed1(:,2); % absorption coefficients for the wavelength range of 250-1450nm in silicon(/m)
abs_depth = 1./abs; %absorption depths of 250-1450nm (m)
distance=(0:0.1e-6:1e-6); %Depth inside the silicon substrate
intensity_i= 5000e-05; %intensity of incoming light (W/m2)
intensity_final=intensity_i*e.^(-abs.*distance); %intensity of incoming light with distance(W/m2)
lambda_nm=lambda/(1e-9); %wavelength in nm
I= ((q*S.*lambda)./(h*c)).*(1-e.^(-abs.*W_pn_biased)).*intensity_final; %Illumination current (A)
I_nm= I/(1e-9); %Illumination current in nA

%% Plot
figure
plot(lambda_nm, I_nm)
xlabel('Wavelength␣(nm)')
ylabel('Current␣(nA)')
```

B

Minimum light intensity determination

The minimum light intensity that can be measured with the photodetector is simulated by testing out different intensities of 470nm, starting from $20\mu W/m^2$ down to $0.1\mu W/m^2$. The results are also compared with the case with no light. The intensity at which the current starts to become unstable and similar to the no-light condition is chosen to be the detection limit. From these tests, $1\mu W/m^2$ is determined to be the detection limit and the current is plotted for the intensities from $1\mu W/m^2$ up to $20\mu W/m^2$ with increments of $5\mu W/m^2$ to show that the current plots have a distinction from each other for different light intensities. The current response at different intensities for pre-determined configurations is shown in figure B.1.

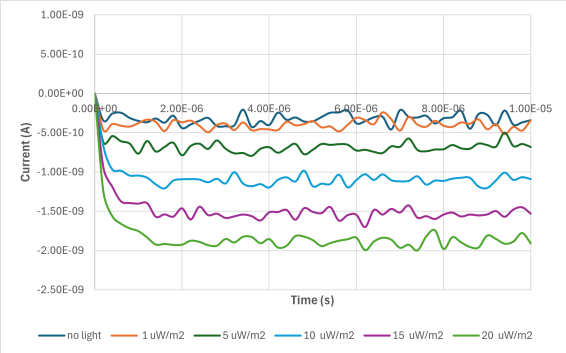

(a) $5\mu m$ n-well and $100\mu m$ channel configuration

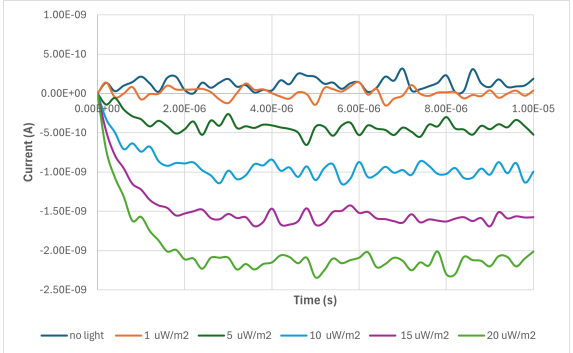

(b) $5\mu m$ n-well and $150\mu m$ channel configuration

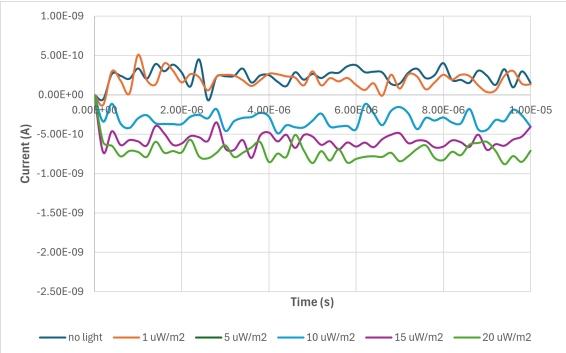

(c) $15\mu m$ n-well and $60\mu m$ channel configuration

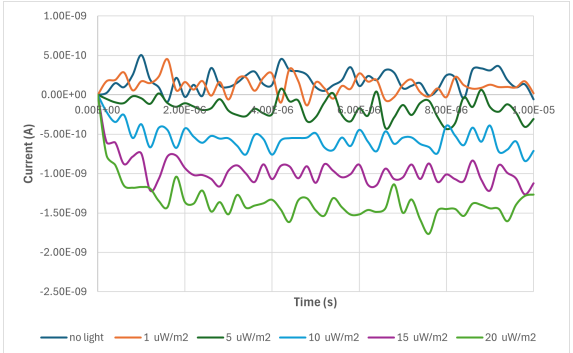

(d) $15\mu m$ n-well and $100\mu m$ channel configuration

Figure B.1: Current response of the device configurations at different light intensities

All of the simulations show an overlap between the no light condition and the light intensity of $1\mu W/m^2$, which indeed shows that it is the limit for detection. For the rest of the intensities, the separation between the intensities indicates the possibility of their detection based on the current magnitude. The expected drift current sign is negative, as the wells are n-type, and therefore, the current is the opposite of the flow inside the n-well. A switch in the current sign is observed for lower intensities, which is attributed to the presence of hole diffusion currents. This is because, with lower intensities, the magnitude of the drift current gets lower compared to the diffusion currents that can reach the depletion region. As a result, the diffusion currents start to dominate the simulation, which will show a positive value based on hole movement.

C

Mask Design

The mask is designed in KLayout 0.28.17 and consists of 9 images. Two of the nine are designed for pad opening, which is suitable for positive and negative (SU8) photoresists. Each layer of the mask and the complete mask design with the labeling of the regions of the mask are presented.

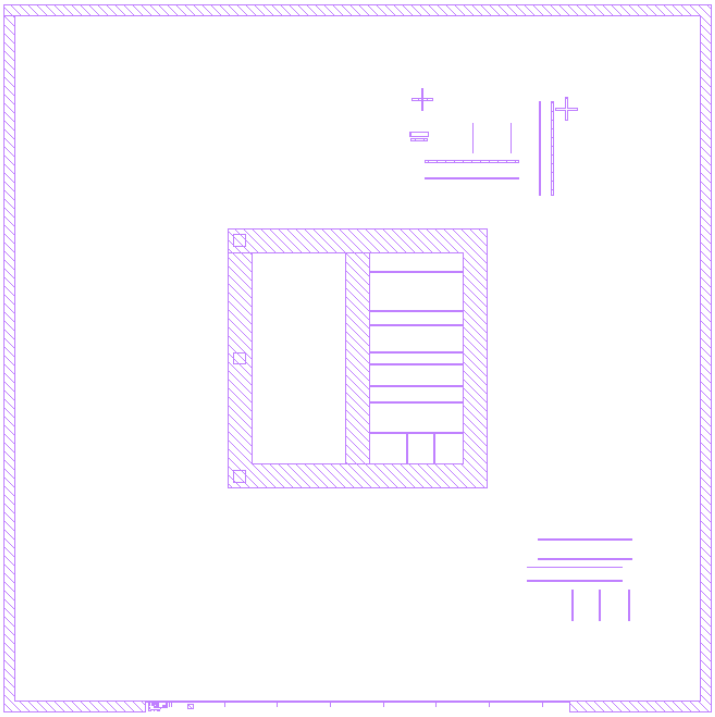

Figure C.1: Image 1: P-type doping

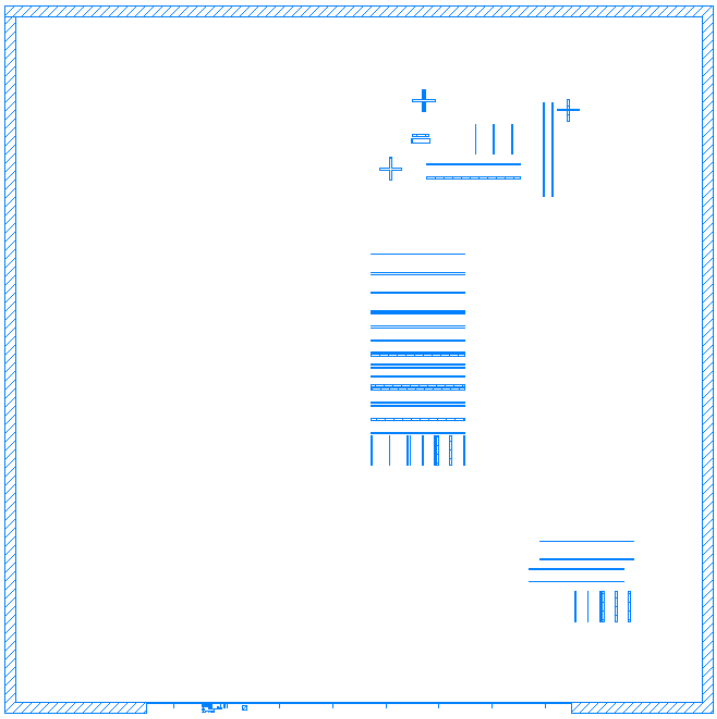

Figure C.2: Image 2: N-type doping

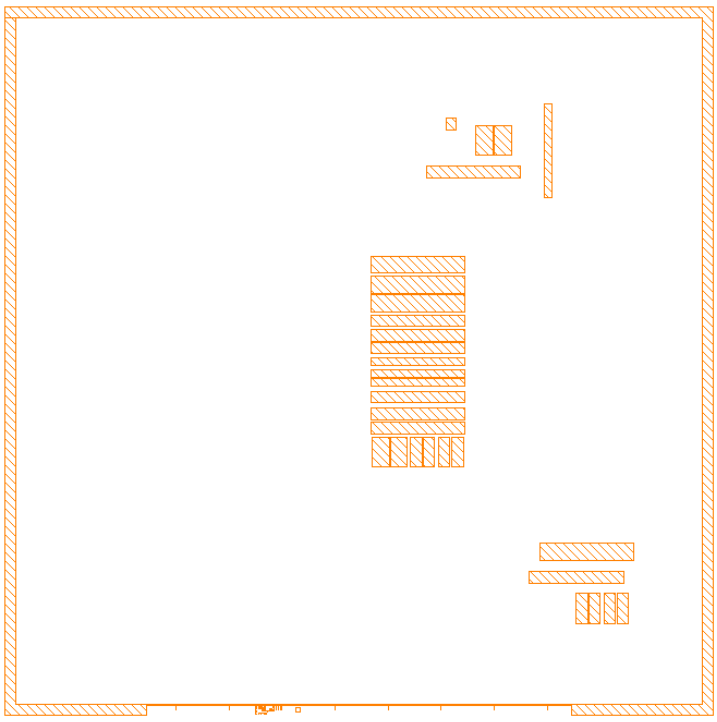

Figure C.3: Image 3: Gate opening

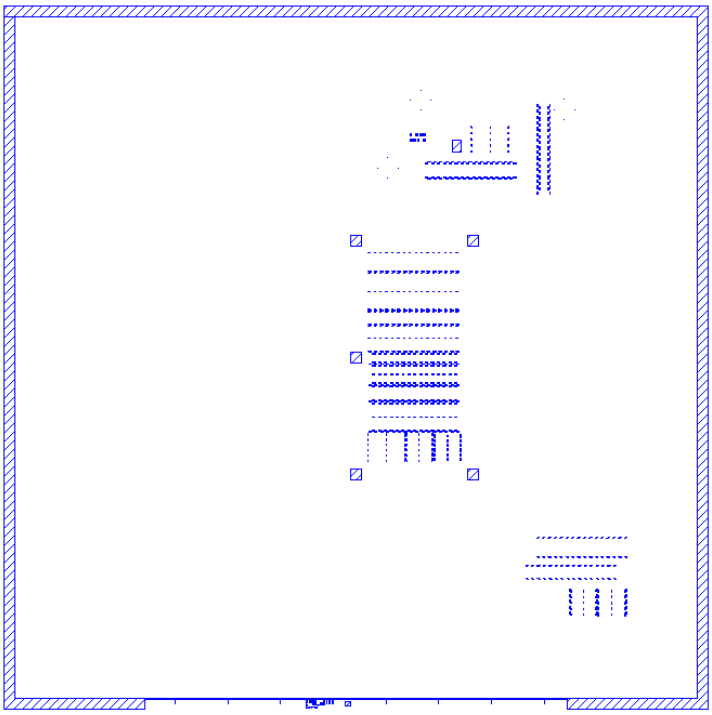

Figure C.4: Image 4: Contact opening

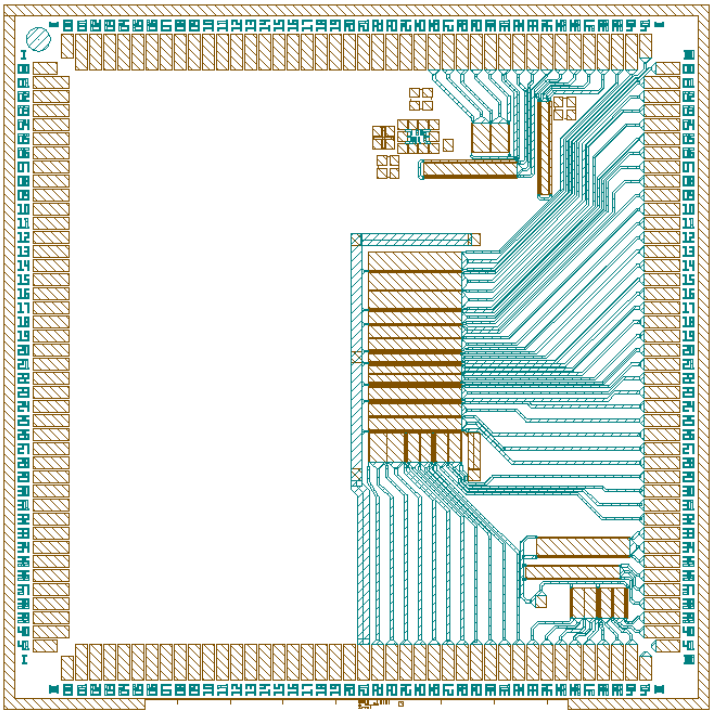

Figure C.5: Image 5: Metal interconnect

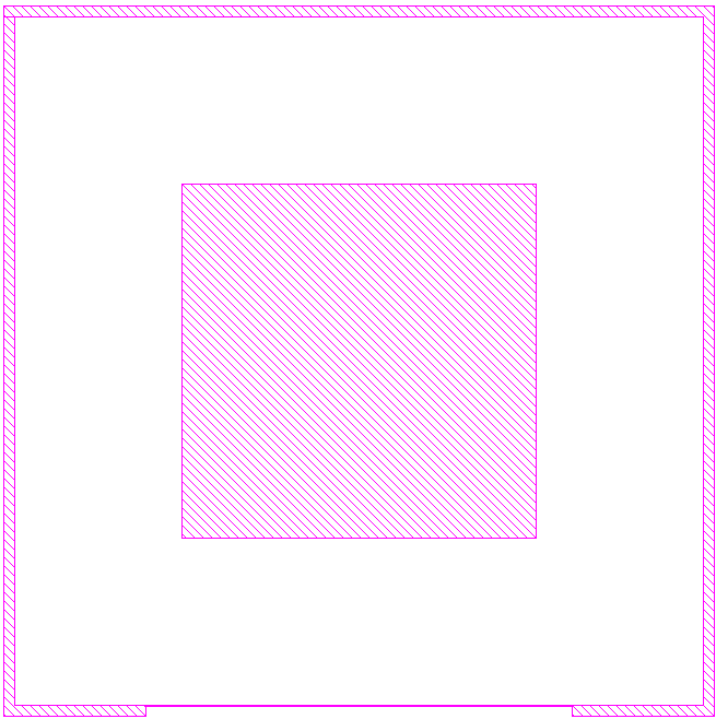

Figure C.6: Image 6: Back-side opening

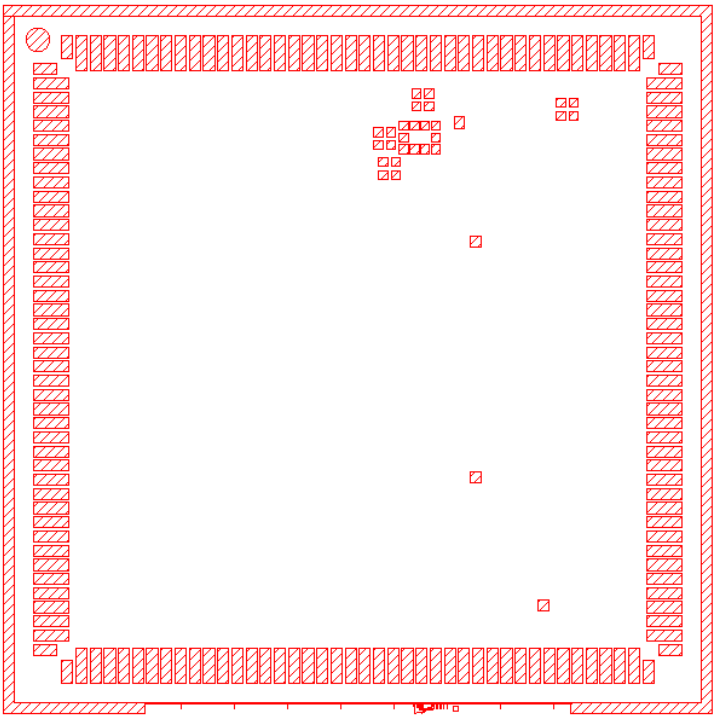

Figure C.7: Image 7: Pad opening (Positive photoresist)

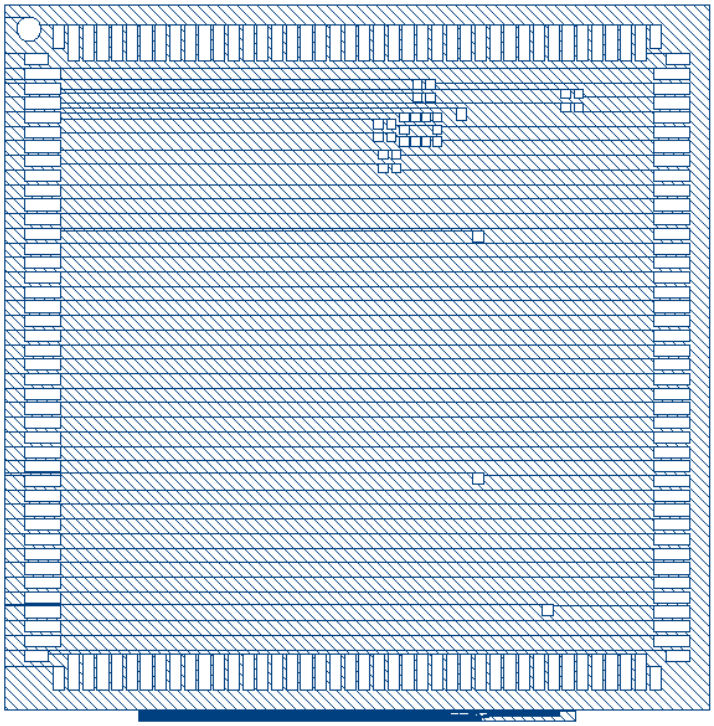

Figure C.8: Image 8: Pad opening (Negative photoresist)

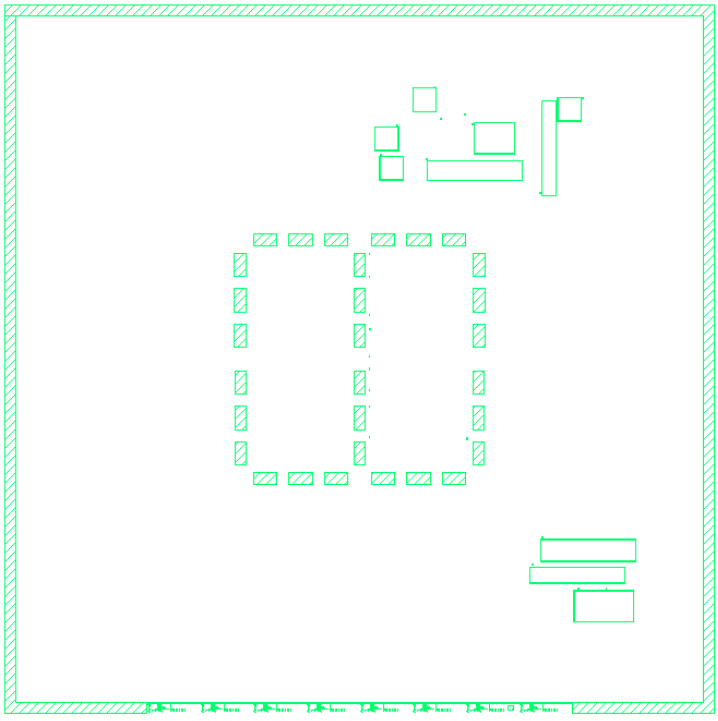

Figure C.9: Image 9: Shallow Trench Isolation

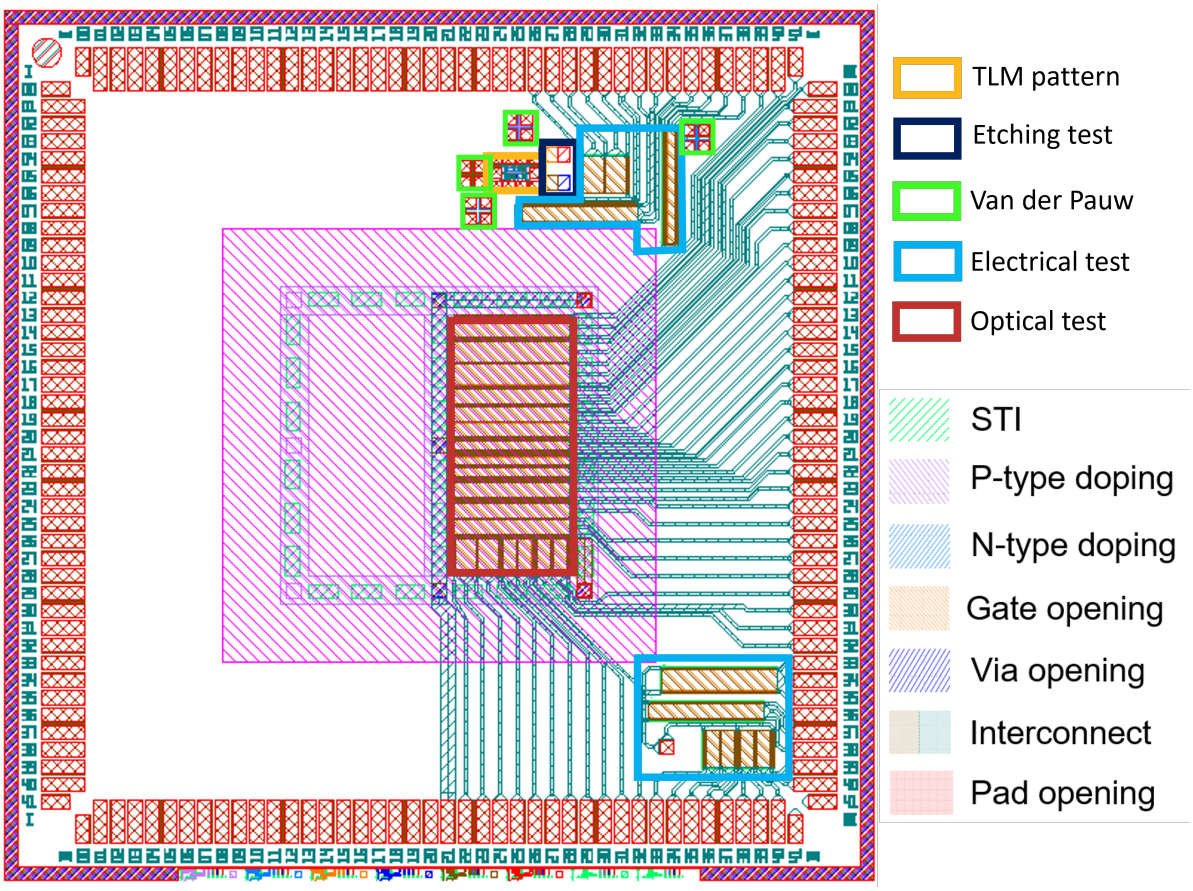

Figure C.10: Complete mask design with labeling of the specific regions of the mask

D

Transmission spectrum of filters at different angles of incidence

For all the filters, the transmission spectrum shifts toward lower wavelengths as expected based on Snell's Law.

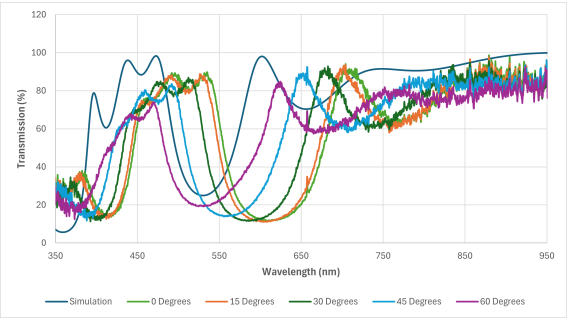

(a) Filter 1

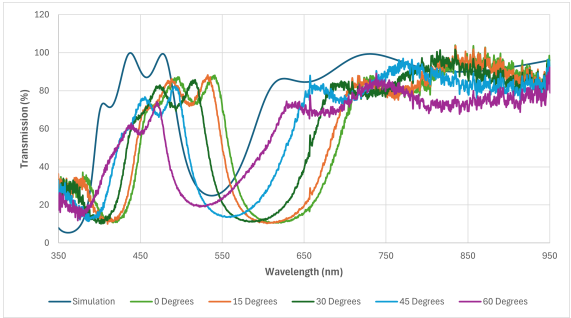

(b) Filter 2

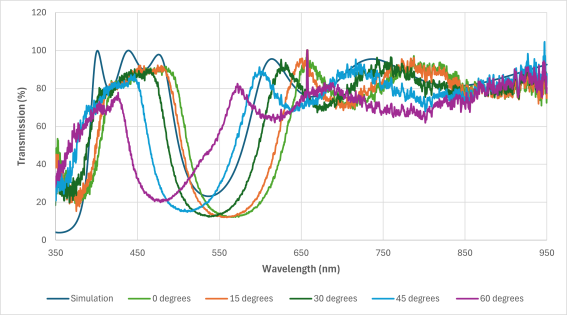

(c) Filter 3

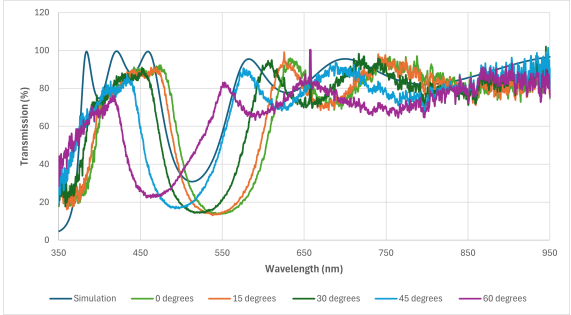

(d) Filter 4

Figure D.1: Transmission spectra of the Fabry-Perot filters at different angles of incidence

E

Transmission spectrum of ZnO absorption layers at different angles of incidence

The transmission spectrum of each ZnO sample is shown for different annealing times and spinning speeds.

All of the transmission spectra show a reduction in the transmission of 350nm compared to other wavelengths. In addition, a reduction in the total transmission is observed for increasing the angle of incidence.

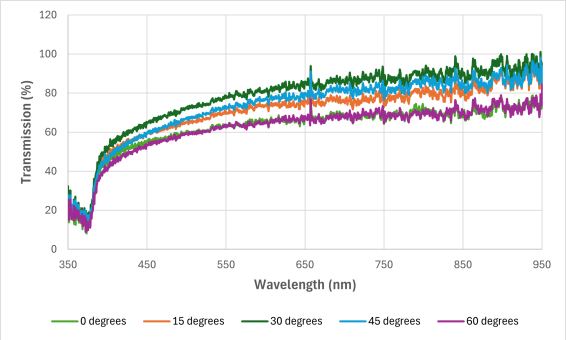

Figure E.1: Transmission spectrum of ZnO sample with 1000rpm/80s spin coating and 10-minute annealing

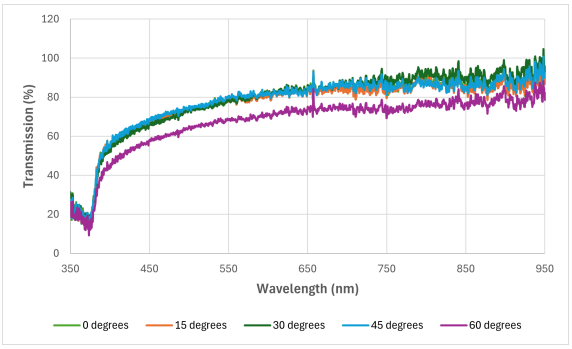

(a) 1-minute annealing

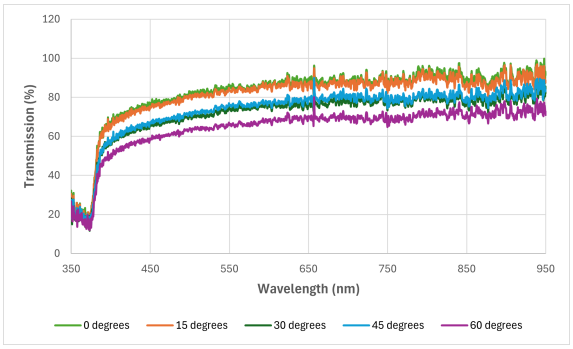

(b) 2-minute annealing

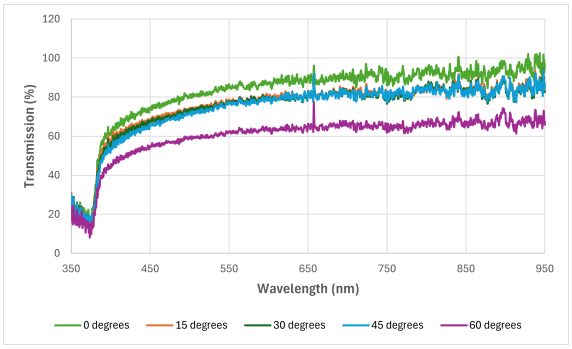

(c) 10-minute annealing

Figure E.2: Transmission spectrum of ZnO samples with 1500rpm/65s spin coating

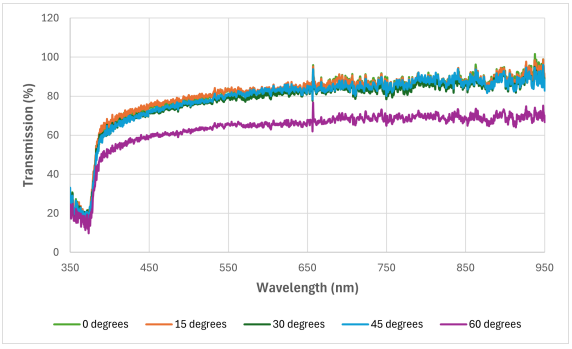

(a) 1-minute annealing

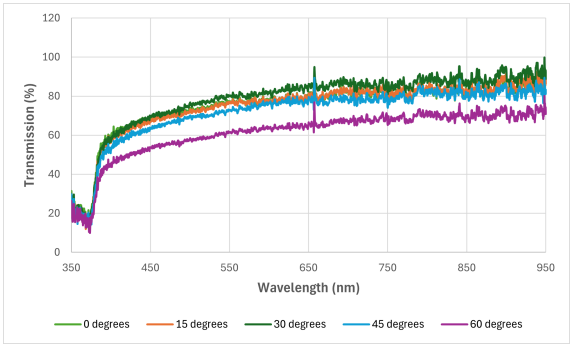

(b) 2-minute annealing

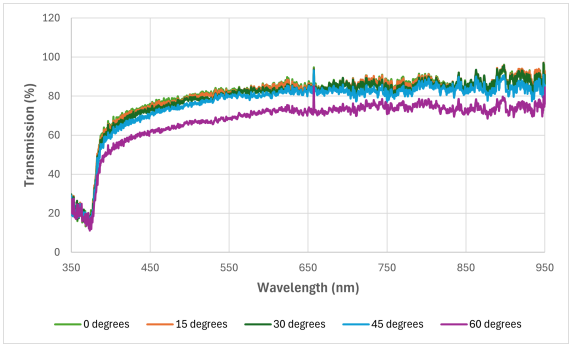

(c) 10-minute annealing

Figure E.3: Transmission spectrum of ZnO samples with 2000rpm/40s spin coating

F

Transmission spectrum of filters with ZnO absorption layers at different angles of incidence

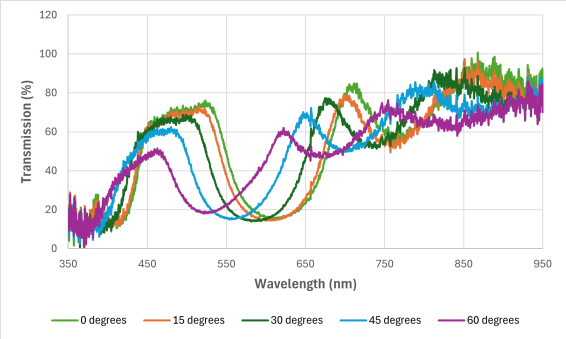

(a) Filter 1 with ZnO absorption layer

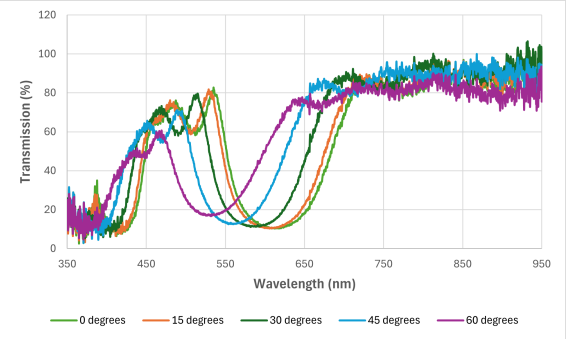

(b) Filter 2 with ZnO absorption layer

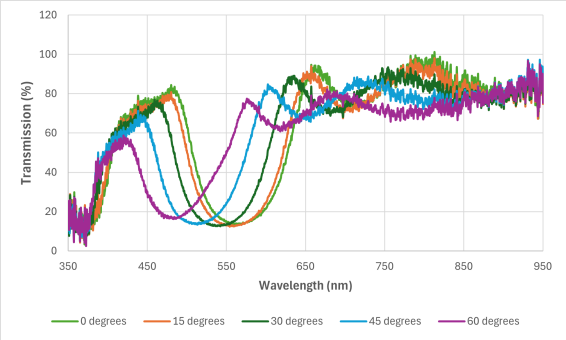

(c) Filter 3 with ZnO absorption layer

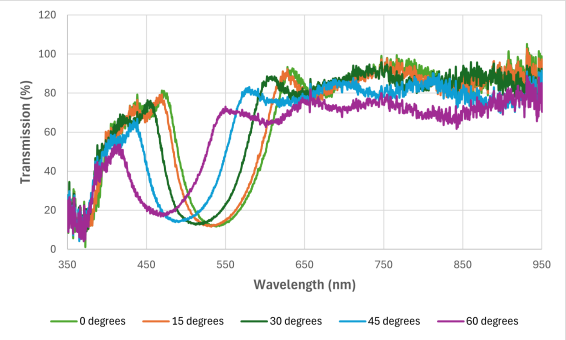

(d) Filter 4 with ZnO absorption layer

Figure F.1: Transmission spectra of the Fabry-Perot filters with ZnO absorption layers at different angles of incidence